SHUNT ACTIVE POWER FILTER WITH EXTENDED-FRYZE ADAPTIVE NOTCH FILTER AND WEIGHTAGE-BASED PARTICLE SWARM OPTIMIZATION PROPORTIONAL INTEGRAL CONTROLLER

By

SYAHRUL HISHAM BIN MOHAMAD @ ABD RAHMAN

Thesis Submitted to the School of Graduate Studies, Universiti Putra Malaysia, in Fulfilment of the Requirement of The Degree of Doctor of Philosophy

March 2024

FK 2024 45

Abstract of thesis presented to the Senate of Universiti Putra Malaysia in fulfilment of the requirement for the Degree of Doctor of Philosophy

SHUNT ACTIVE POWER FILTER WITH EXTENDED-FRYZE ADAPTIVE NOTCH FILTER AND WEIGHTAGE-BASED PARTICLE SWARM OPTIMIZATION PROPORTIONAL INTEGRAL CONTROLLER

By

SYAHRUL HISHAM BIN MOHAMAD @ ABD RAHMAN

March 2024

Chairman : Mohd Amran Mohd Radzi, PhD
Faculty : Engineering

The integration of Shunt Active Power Filters (SAPF) into electrical power systems is pivotal for mitigating current harmonics, which pose numerous quality challenges. A critical aspect of SAPF lies in the implementation of harmonics or fundamental extraction algorithms, necessitating quick and precise current generation of harmonic references to ensure effective compensation. While Adaptive Notch Filter (ANF) offers a method for signal extraction, its application in three-phase systems especially in the utilization of SAPF is limited particularly due to the absence of direct DC-link controller utilization.. Consequently, this research introduces an enhanced version termed as Extended Fryze ANF (EFANF) within the SAPF, specifically designed for fundamental signal extraction across single-phase and three-phase applications, while incorporating a DC-link voltage regulation controller based on the Fryze power-loss equation. This novel extraction algorithm boasts simplified design construction, frequency tracking, and eliminates reliance on phase-locked loop (PLL) synchronization. Balancing energy between the DC link voltage and filter current is paramount in SAPF development, commonly achieved through Proportional-Integral (PI) controllers. Despite their simplicity, PI voltage regulators suffer from time-consuming trial-and-error tuning. In response, an optimization method utilizing Weightage-Based Particle Swarm Optimization (WBPSO) is proposed, enabling the acquisition of optimal Kp and Ki values tailored to the controller's requirements. The integration of EFANF with an optimized PI controller is expected to elevate SAPF's dynamic performance, maintain requisite voltage levels via the DC-link, and minimize total harmonic distortion (THD). The efficacy of both algorithms is validated through comprehensive simulation using MATLAB/Simulink and experimental execution on DSpace RS1104, demonstrating satisfactory harmonic mitigation across diverse multi-load conditions. The results indicate THD reduction below 5%, in adherence to IEEE 519™-2014 standards, affirming algorithmic functionality in steady and transient state conditions. Furthermore, the algorithm effectively tends to maintain the DC link capacitor voltage based on the reference voltage throughout the changes of multi-loads conditions, underscoring its holistic impact on SAPF efficacy within electrical power systems. Hence, it can be concluded that the proposed algorithms have successfully performed their functions by effectively enhancing the operation of the SAPF.

Keywords: Active Power Filter, Notch Filter, Optimization and Power Quality.

SDG: GOAL 7: Affordable and clean energy.

Abstrak tesis yang dikemukakan kepada Senat Universiti Putra Malaysia
sebagai memenuhi keperluan untuk Ijazah Doktor Falsafah

PENAPIS KUASA AKTIF PIRAU DENGAN PENAPIS TAKUK ADAPTIF DIPERKEMBANGKAN-FRYZE DAN PENGOPTIMUMAN KUMPULAN ZARAH BERASASKAN BERAT PENGAWAL BERKADARAN KAMIRAN

Oleh

SYAHRUL HISHAM BIN MOHAMAD @ ABD RAHMAN

Mac 2024

Pengerusi : Mohd Amran Mohd Radzi, PhD
Fakulti : Kejuruteraan

Integrasi Penapis Kuasa Aktif Pirau (SAPF) ke dalam sistem kuasa elektrik adalah penting untuk mengurangkan harmonik arus, yang menimbulkan pelbagai cabaran kualiti. Aspek kritikal SAPF terletak pada pelaksanaan algoritma pengekstrakan harmonik atau asas, yang memerlukan penjanaan arus rujukan harmonik yang cepat dan tepat untuk memastikan pampasan yang berkesan. Walaupun Penapis Takik Adaptif (ANF) menawarkan kaedah untuk pengekstrakan isyarat, penggunaannya dalam sistem tiga fasa, terutama dalam penggunaan SAPF, adalah terhad terutamanya kerana ketiadaan penggunaan pengawal DC-link secara langsung.. Akibatnya, penyelidikan ini memperkenalkan versi yang dipertingkatkan yang dikenali sebagai Penapis Takuk Adaptif Fryze Lanjutan (EFANF), yang direka khusus untuk pengekstrakan isyarat asas dalam aplikasi satu fasa dan tiga fasa, sambil menggabungkan pengawal pengawalan voltan DC-link berdasarkan persamaan kehilangan kuasa Fryze. Algoritma pengekstrakan novel ini mempunyai reka bentuk pembinaan yang dipermudahkan, penjejakan frekuensi, dan menghapuskan pergantungan pada penyegerakan gelung terkunci fasa (PLL). Mengimbangkan tenaga antara voltan DC-link dan arus penapis adalah penting dalam pembangunan SAPF, yang biasanya dicapai melalui pengawal Proportional-Integral (PI). Walaupun kesederhanaannya, pengawal voltan PI mengalami pelarasan cuba-dan-salah yang memakan masa. Sebagai tindak balas, kaedah pengoptimuman yang menggunakan PSO berasaskan wajaran (WBPSO) dicadangkan, yang membolehkan pemerolehan nilai Kp dan Ki yang optimum yang disesuaikan dengan keperluan pengawal. Integrasi EFANF dengan pengawal PI yang dioptimumkan dijangka meningkatkan prestasi dinamik SAPF, mengekalkan tahap voltan yang diperlukan melalui DC-link, dan meminimumkan distorsi harmonik total (THD). Keberkesanan kedua-dua algoritma ini disahkan melalui simulasi komprehensif menggunakan MATLAB/Simulink dan pelaksanaan eksperimen pada DSpace RS1104, menunjukkan pengurangan harmonik yang memuaskan dalam pelbagai keadaan beban. Hasil menunjukkan pengurangan THD di bawah 5%, mematuhi piawaian IEEE 519™-2014, mengesahkan fungsi algoritma dalam keadaan mantap dan transien. Selain itu, algoritma ini berkesan mengekalkan voltan kapasitor DC-link sepanjang perubahan keadaan beban, menekankan impak holistiknya terhadap keberkesanan SAPF dalam sistem kuasa elektrik. Oleh itu, dapat disimpulkan bahawa algoritma yang dicadangkan telah berjaya melaksanakan fungsinya dengan meningkatkan operasi SAPF secara berkesan.

Kata Kunci: Penapis Kuasa Aktif, Penapis Takuk, Pengoptimuman dan Kualiti Kuasa.

SDG: MATLAMAT 7: Tenaga yang berpatutan dan bersih.

ACKNOWLEDGEMENTS

"All praise be to Allah S.W.T, the Almighty God. There is no god but Allah, and Muhammad is His messenger. I am deeply grateful to Allah for bestowing upon me strength, inspiration, and good health. By His will, I have managed to complete my thesis and successfully conclude my Ph.D. journey. Thank you, Allah.

I extend heartfelt thanks to my supervisor, Professor Dr. Mohd Amran Bin Mohd Radzi, for his encouragement, guidance, and unwavering support from the inception to the completion of my studies. My gratitude also goes to my supervisory committee members, Prof. Madya Dr. Nashiren Farzilah Binti Mailah and Prof. Madya Ir. Dr. Noor Izzri Bin Abdul Wahab, for their invaluable support and guidance. With sincere appreciation, I thank my mother, Ramlah binti Mohamad, who has provided blessings and steadfast support throughout this journey—I love you, Mom. My heartfelt love and thanks are also extended to my wife, Siti Shuhada, and my children, Syifa Hanna, Sarah Aleesya, and Anas Mikail. Without your love, support, and understanding, the completion of this significant journey would not have been possible.

I would like to acknowledge my lab members who have offered their support throughout this journey. Without your assistance, reaching this milestone would have been unattainable. Thank you all. Lastly, many thanks go to my sponsor, Universiti Teknikal Malaysia Melaka, for providing me the opportunity to pursue my Ph.D. Your support has opened doors and created possibilities, and for that, I am eternally grateful."

This thesis was submitted to the Senate of Universiti Putra Malaysia and has been accepted as fulfilment of the requirement for the degree of Doctor of Philosophy. The members of the Supervisory Committee were as follows:

Mohd Amran bin Mohd Radzi, PhD
Professor
Faculty of Engineering
Universiti Putra Malaysia
(Chairman)

Nashiren Farzilah binti Mailah, PhD
Associate Professor
Faculty of Engineering
Universiti Putra Malaysia
(Member)

Noor Izzri bin Abdul Wahab, PhD
Associate Professor , Ir.
Faculty of Engineering
Universiti Putra Malaysia
(Member)

ZALILAH BINTI MOHD SHARIFF, PhD
Professor and Dean
School of Graduate Studies
Universiti Putra Malaysia

Date: 08 August 2024

TABLE OF CONTENTS

LIST OF TABLES

LIST OF FIGURES

LIST OF ABBREVIATIONS

ANF	Adaptive Notch Filter
AC	Alternating Current
ADALINE	Adaptive Linear Neural Network
ANN	Adaptive Neural Networks
APF	Active Power Filter
ASD	Adjustable Speed Drives
COG	Centre Of Gravity
CSI	Current Source Inverter
DC	Direct Current
DFT	Discrete Fourier Transform
EFANF	Extended Fryze Adaptive Notch Filter
FCC	Fryze Current Control
FE	Final Error
FET	Field-Effect Transistor
FFT	Fast Fourier Transform
FIR	Finite Impulse Response
GA	Genetic Algorithm
HPF	High Pass Filters
IGBT	Insulated-Gate Bipolar Transistors
IIR	Infinite Impulse Response
LPF	Low Pass Filters
MF	Membership Functions
MOSFET	Metal-Oxide-Semiconductor Field-Effect Transistors
MPC	Model Predictive Control
NLL	Non-Linear Load

PCB	Printed Circuit Boards
PCC	Point Of Common Coupling
PI	Proportional Integral
PID	Proportional Integral Differential
PLL	Phase Lock Loop
PNC	Point Of Normal Coupling
PPF	Passive Power Filter
PQ	Power Quality
PSO	Particle Swarm Optimization
PWM	Pulse-Width-Modulation
R	Resistive
RC	Resistive And Capacitive
RL	Resistive And Inductive
RMS	Root Means Square
SAPF	Shunt Active Power Filter
SMC	Sliding Mode Controller
SMPS	Switched Mode Power Supply
SSE	Sum State Error
TDD	Total Demand Distortion
THD	Total Harmonics Distortion
UPQC	Unified Power Quality Compensator
UPS	Uninterruptible Power Supply
VAC	Voltage of Alternating Current
VDC	Voltage of Direct Current
VSI	Voltage Source Inverter
WBPSO	Weightage Based Particle Swarm Optimization

WT	Wavelet-Packet Transform
ZCD	Zero Crossing Detectors

CHAPTER 1

INTRODUCTION

1.1 Background of Study

In recent years, there has been a strong urge regarding the importance of power quality supplies in the industrial, commercial, and residential sectors. The utilization of various electrical and electronic equipment, such as four-quadrant power electronics converter, diverse switching mode power supply, motor speed adjustable unit, arc furnaces, and other equipment, have risen dramatically over the years. All the above equipment are usually operated based on diodes, triodes, transistors, and thyristors, which promote the nonlinearity characteristics and contribute to the pollution of harmonics in electrical power systems [1]–[3]. The outcomes of the polluted sources by harmonics could be harmful to the other loads within the same bus system. In conjunction with this, inductive and capacitive (LC) filter is normally used to reduce the harmonics and improve the power factor [4], [5]. However, passive LC filters generally are load-dependent, bulky, and unyielding to changes [5]–[7]. Various studies on power correction techniques are ongoing concerning these issues according to the power system pollution sources or circumstances. The active power filter (APF) is one of the most studied areas.

APFs have been through a lot of changes in shape design, research, application, and in terms of commercialization within the past three decades [7]. In advancement, APFs can compensate for current-based distortions such as current harmonics, reactive power, and neutral current [8]. Based on their characteristics, they are also applied for voltage-based distortion such as voltage harmonics, voltage flickers, voltage sags, swells, and voltage imbalances [9]. APF can be divided into two categories, namely as single-phase and three-phase. Three-phase APFs may be with or without a neutral connection and used for high-power nonlinear loads such as adjustable speed drives (ASD) and AC to DC converters. Whereas single-phase APFs are used to compensate for power quality problems caused by single-phase loads such as DC power supplies. APFs can be divided into active series power filters, active shunt power filters, a combination of both known as unified power quality compensator (UPQC) and the unity of APFs, and passive power filters known as hybrid APFs. All of these topologies are based on inductive energy storage for current source inverter (CSI) and capacitive energy storage for voltage source inverter (VSI). When applying APFs, two significant tasks are typically expected within the processing of APF which are the capability to produce the purest reference current and the ability to track the reference current signal.

The performance of the APF usually depends on the extraction algorithms. To generate compensating current, harmonics or fundamental extraction algorithms are required. The extraction algorithms can be divided into time- and frequency-based methods. The frequencies-based algorithms designed for the APF are Fourier series, discrete Fourier transform, fast Fourier transform, Kalman filter, and wavelet transforms. Although these algorithms can produce excellent reference current, their usage involves a transformation in the frequency domain, thus increasing the complexity of the algorithm if applied in the time domain. According to the previous research works, commonly employed algorithms in APF application mostly rely on time domain techniques, such as instantaneous active-reactive power theory (p-q), synchronous reference frame theory (d-q), power balance theory, and capacitor voltage control. These algorithms exhibit superior performance when operated under undistorted balanced voltages. In time-based algorithms, all these algorithms are known as classical techniques.

A current method that has recently emerged involves estimating current references using intelligent techniques. This method can be broken down into several sub-methods, such as supervised neural networks, adaptive neural networks (ANN), training of neurons, and adaptive linear neural network (ADALINE). These algorithms possess the ability to learn and enhance the harmonics condition within the system. Another advantage of intelligent techniques is that they can extend the value of estimation or extraction to other waveforms by updating the learning process. However, the greater the extraction value, the more complex the algorithms are needed. This requirement will increase the computational burden of the algorithms. Additionally, these algorithms require training before being directly applied to APFs, further adding to the computational burden of implementing intelligent techniques.

An alternative to those algorithms is an adaptive notch filter (ANF) method. The ANF is a well-researched technique that removes and recovers sinusoids from an unstated frequency of variable sources and noises. Currently, ANF is widely used in the field of frequency estimation. ANF is based on the finite impulse response (FIR) or infinite impulse response (IIR) model. It has been improved regarding its predecessor in terms of convergence properties, such as unbiased frequency estimation, improved tracking, and enhanced reliability for extremal input frequencies [10]. ANF can also detect, estimate, filter, and track the sinusoidal signal in the wideband noise environment. The ANF was initially designed to operate in the frequency domain, which limited its application in various contexts. Later, the ANF is transposed into a continuous time domain for larger areas of implementation [11]. It was further improved by scaling the forcing signal to obtain a unitary gain, which avoids undesirable crossing through zero of the estimated frequency and enhances stability and convergence [12]. ANF can be adjusted to the requirement of filter parameters adaptively, making the error output can control reach the minimum available value and thus accomplishing the maximum filtering effect. Another characteristic of the ANF compares to other conventional algorithms is the capability of the ANF to extract individual harmonic components, which makes it effective in selective harmonics compensation [13].

1.2 Problem Statement

Adaptive Notch Filtering (ANF) is a method used to extract signals by isolating fundamental and individual harmonic components, typically from noise-corrupted signals [14]. Traditionally, ANF employs a linear filter that allows all frequencies to pass except for a designated notch frequency where the gain is zero. Initially designed based on the Infinite Impulse Response (IIR) filter structure, ANF has evolved into a lattice-based structure, enhancing performance and application flexibility by allowing individual tuning and bandwidth attenuation using planar rotators [15]. This approach offers stable numerical behavior and faster computational rates. ANF has been utilized as a power system frequency estimator, offering a simpler and faster response compared to Phase-Locked Loop (PLL) systems. While effective for frequency estimation, more research is required to explore this stage of ANF's potential for signal extraction and harmonics mitigation [16].

In Active Power Filters (APFs), harmonics should be defined for the entire power system to filter overall harmonics. Despite ANF's capability for harmonic extraction, current algorithms focus solely on current-induced harmonics, neglecting voltage-induced harmonics, which also contribute to overall distortion. Furthermore, while ANF has been adapted for current decomposition to filter active, reactive, and harmonic components, its application remains restricted to current, limiting its effectiveness[12]. In [16], the ANF was used only for decomposing the currents drawn by nonlinear loads into harmonic, active, and reactive currents. However, its application for grid-integration and APF has not been discussed. Although, there is an application of using ANF in the PQ and DQ algorithm as filter to replace low pass filter, this application undermines the capabilities of the ANF as an individual reference generation algorithm as well increase the complexity of the original filtering use by the algorithm.

Another critical component in APF systems is the DC-link capacitor, which acts as the primary voltage source. Control algorithms must handle DC-link voltage variations to prevent capacitor damage due to over-voltage and ensure proper operation during under-voltage conditions. Dynamic operations, such as load changes, directly impact APF performance. Current ANF designs limit functionality to single-phase systems, complicating three-phase system integration with DC-link controllers. Effective integration requires incorporating DC-link control directly within the ANF for multi-phase systems, a process need to be cater when integrating a three phase system which are lack in the current application of ANF[12].

Ensuring optimal APF performance involves selecting appropriate DC-link control strategies to manage sudden load changes and high-frequency ripple caused by power electronic switching [17]. While advanced control strategies like Fuzzy Logic [18], Artificial Neural Networks (ANN), and model predictive control (MPC) [19], offer improved performance, they are often complex and computationally intensive compared to simpler Proportional-Integral (PI) controllers. However, tuning PI controllers is challenging, often relying on trial-and-error methods that may not account for system dynamics and nonlinearities, leading to suboptimal performance [20]. Ziegler-Nichols tuning method is popularly used for tuning and needs wide-ranging experimentation. Hence, there is always the possibility of better tuning of to improve the settling time and overshoot [21].

Therefore, there is a need for more advanced tuning methods that can cater for the dynamic behavior and nonlinearities of the system to ensure that the PI controller is properly configured for the specific application. One of the method that can be used in order to optimize the process of PI tuning is optimization method [21]. However, as the value of THD and DC link error are intercorrelated with each other during the tuning process, special observation needs to be considered on the tuning method. Consequently, the optimization method applied must simultaneously address and balance both components THD and DC link error during SAPF operation.

Therefore, by improving the extraction of harmonics in the ANF algorithm and PI tuning method for DC link capacitor voltage control by proposing new controllers. This controller should be able to yield better signals for both the fundamental and harmonic frequencies and increased capabilities of the APF in controlling the power balance within the capacitor.

1.3 Aim and Objectives

This work aims to develop a three-phase shunt active power filter (SAPF) with improved harmonics extraction and DC-link capacitor control algorithms. The detailed objectives are as follows:

1. To develop a harmonics extraction algorithm based on the adaptive notch filter and Fryze conductance theory named as extended Fryze adaptive notch filter (EFANF).

2. To design weightage-based particle swarm optimization (WBPSO) for optimizing PI controller implemented with EFANF.

3. To assess the performance of EFANF and optimized PI based on WBPSO for three-phase SAPF in reducing the THD due to non-linear loads and DC-Link voltage stability through simulation and experimental works.

1.4 Scope of Work

The scope of the research work emphasizes on the listed items below:

1. The proposed algorithm for a three-phase three-wire SAPF using a three-phase voltage source inverter (VSI) topology with a DC-Link as the voltage source and a filter inductor attached to the inverter. This work contributes explicitly towards the harmonics compression within the electrical power system.

2. The effectiveness of the proposed extraction algorithm to generate reference currents is assessed based on the shape and the phase of three-phase instantaneous supply current.

3. The effectiveness of the proposed current control algorithm to compensate harmonic currents and reactive power is measured based on Total Harmonic Distortion (THD) values, the Institute of Electrical and Electronics Engineers (IEEE) Standard 519-2014 and PFs.

4. During the simulation stage, the proposed APF is simulated under a three-phase supply voltage of 400 V and a frequency of 50 Hz. Then the work covers development of WBPSO for PI optimization. The optimized PI will be simulated synchronously with the EFANF.

5. Experimental work is performed at 110V and 50Hz to ensure safety and equipment capability. The effectiveness of the proposed EFANF will be measured by the capability of the APF to compensate the current harmonics based on the available power quality standard.

The experimental work is done to verify the proposed EFANF as the new harmonic extraction method and the optimized PI based on WBPSO as the DC-Link voltage controller. The proposed algorithms are tested under two load conditions which are the steady state and dynamic state conditions. In a steady state, the algorithms are evaluated under three different values for resistive, inductive and capacitive loads. For the dynamic state, the algorithms are tested under changes of load values and secondly under load type between capacitive inductive and resistive. All proposed algorithms are developed and simulated in MATLAB / Simulink. Additionally, DSPACE 1104 microcontroller board is employed to execute all the proposed algorithms for experimental verification.

1.5 Thesis Organization

The thesis is organized based on the following chapters.

Chapter 2 discusses harmonic distortion, harmonic mitigation tools, and the principal operation of SAPFs. Also, it elaborates on the roles of the control system of SAPFs.

Chapter 3 explains the development of a three-phase three-wire SAPF using a three-phase, three-leg VSI, the proposed control strategy, and the proposed algorithms.

Chapter 4 presents and discusses both simulation and experimental results.

Chapter 5 concludes the findings and contributions of the proposed algorithms. Some recommendations for future work are also provided.

CHAPTER 2

LITERATURE REVIEW

2.1 Introduction

This chapter describes power quality terms within the power system aspects. It methodically assesses the power quality contribution of the negative element, the possible sources of the power quality, the types of power quality, and the commonly used power quality mitigation techniques. The more composite details of power quality in terms of harmonics are also discussed comprehensively within the subchapters.

2.2 Power Quality

Power quality is mainly associated with maintaining the qualities of energy in the process of generation, transmission, distribution, and consumption of the electrical power system. In some terms, power quality is defined as the alteration from a clean sinusoidal voltage waveform to an unclean or distorted sinusoidal voltage waveform. Power quality evaluation involves assessing how the supply system's voltages, currents, and frequency deviate from their intended values. Given the variability in power quality issues, various classifications are employed to categorize and identify the specific problems. Each category of power quality is defined by the specific property to determine the problem, and the conditions are separated as "steady-state" and "non-steady-state" occurrences in some situations. An example of the guideline used to classify related problems is as provided in ANSI C84.1, where the factor of the event duration defines this standard. Another standard is IEE-519 which emphasizes the wave shape, especially in terms of duration, and magnitude, as in the give classification guideline. Furthermore, the IEC standard considers the frequency range to classify the degree of power quality events.

Typically, power quality issues arise due to the pollution of the AC supply system originate from various disturbances of numerous nonlinear loads such as uninterruptible power supply (UPS), furnaces, adjustable speed drive (ASDs), converters, and power electronics equipment coupled at the point of common coupling (PCC) [22]–[24]. These pollutions in the power supply contributed to power quality issues such as voltage/current harmonics, spikes, notches, swell, surges, sag/dip, unbalance, glitches, flickers fluctuations, and outages. In addition, power quality issues may also happen due to natural occurrences such as lighting, flashover, equipment failures, and faults.

Based on various research works conducted, power qualities have impacted total cost losses of roughly RM1.5 billion due to voltage sag and RM82 million due to harmonics [25]. Aside from the direct impact on the economic values in industrials and commercials, the power quality is also the cause of incline losses within the distribution system and electrical machine, failures in capacitor banks, noise, overvoltage, and excessive current caused by resonance vibrations, sequential negative currents in motor and generators, dielectric breakdown, derating of cable, communication system and signal disruption.

As the electrical power system advances, various issues related to power quality have emerged. These issues are diverse and require classification to identify their distinct characteristics. Power quality issues are classified based on the occurrence during non-steady and steady-state events. The primary characteristics of voltage, current, and frequency are measured to determine the severity and nature of these issues in supply and load systems. Precise identification and analysis of these power quality issues are essential for improving the overall efficiency and reliability of the power system.

Most phenomena occurring in transitory nature, such as sag (dip), swell, short-duration voltage differences, power frequency deviations, and voltage fluxes, are included in the non-steady-state or sometimes referred to as transient categories of power quality. Long-duration voltage changes, waveform distortions, unstable voltages, DC offset, flicker, low power factor, unbalanced load currents, load harmonic currents, and extreme neural currents are examples of steady-state power quality issues.

The next level of power quality classification is based on the electrical power system's primary quantities, such as voltage, current, and frequency [26]. When referring to the voltage, the problems include flickers, sag, under-voltage, voltage distortion, swell noise, and overvoltage [27]–[30]. Some of these problems also occurred to the current with additional conditions such as unbalanced currents, harmonics current, reactive power components of current, and neutral current issues.

The following classification is centered on the load or supply system. Generally, the load-induced power qualities are issues due to the nature of the applied load, such as fluctuating loads consisting of reactive current power components, DC offset, harmonics, neutral current, and unbalanced currents. In contrast, the power quality problems due to supply are usually related to voltage and frequency, such as voltage distortion, notches, swell, noises, sag, unbalanced, and flicker [31]. Frequency quality problems are generally associated with frequency variation below or above desired values.

Table 2.1 show examples of poor power quality and descriptions of poor power-quality "events."

Table 2.1: Power quality classification in power system [32]

Power Quality	Description
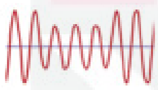	Voltage sag, also known as voltage dip, is the temporary decline in the value of the RMS line voltage within 0.1 to 0.9 of the nominal per unit (p.u) value
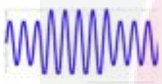	Voltage swell is considered as the inverse of voltage sag, which involves a temporary rise within the value of the RMS line voltage within 1.1 to 1.8 of normal line voltage p.u.
	An impulsive transient is a brief, unidirectional voltage, current, or both fluctuation on a power line.
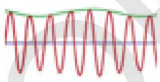	Voltage flickers is fluctuations are RMS line-voltage variations that are comparatively minor (less than 5%).
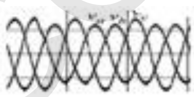	A three-phase voltage "imbalance" is a change in the amplitudes of the voltages with respect to one another.
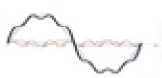	Harmonics are byproducts of nonlinear loads that create periodic sinusoidal distortions in the supply voltage or load current.

2.3 Harmonics

Harmonic can be defined as "a sinusoidal component of a periodic wave or quantity having a frequency that is an integral multiple of the fundamental frequency." Therefore, harmonic is the existence of voltage or current having the frequency of multiplication of fundamental voltage or current in the voltage/current of the system. For example, Figure 2.2 (a) displays a 50 Hz fundamental frequency waveform followed by corresponding frequencies of third (150 Hz), fifth (250 Hz), and seventh (350 Hz) harmonic. The summation of the fundamental component and all the harmonic components will lead to a distorted waveform, as shown in Figure 2.1 (b), where the waveform is not identical to the fundamental elements.

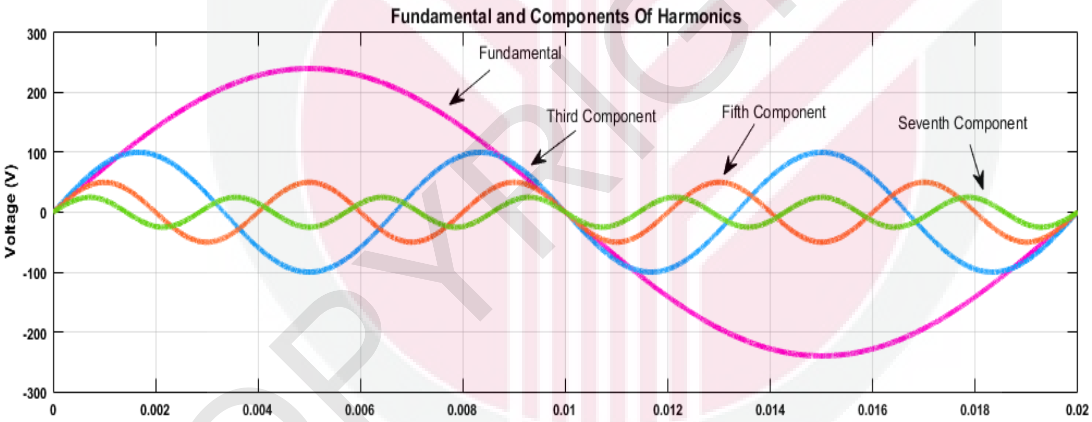

(a)

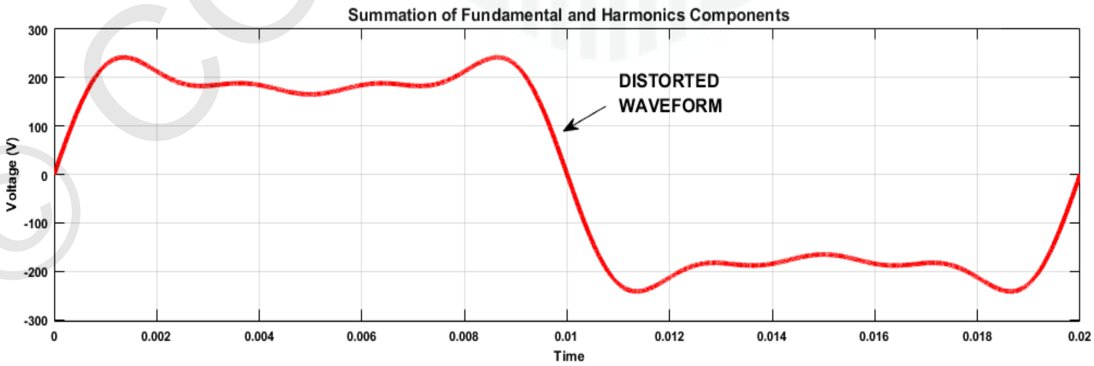

(b)

Figure 2.1: (a) Waveform of 50 Hz, 150 Hz, 250 Hz, and 350 Hz individual frequency and (b) distorted waveform from summation of fundamental and harmonics components

The leading cause of harmonic generation is the non-linear loads. The non-linear load can be explained as a load with changing impedance depending on the applied instantaneous voltage. These non-linear changes will cause a non-sinusoidal current to be drawn out when used with supply the voltage. A non-linear load does not exhibit a constant current and voltage relation along the time frame and thus contributes to the generation of harmonics.

Given that a distorted waveform is the composition of the summation of fundamental and harmonic components, any periodic waveform can be inversely decomposed into harmonic components. By decomposition the waveform will make it possible to individually analyze of each element of the distorted waveform thus allowing familiar circuit analysis techniques to find the combined effect of these parts, represented by the sum of their harmonic derivatives. This method usually shows the harmonics in the form of individual harmonic spectrum. The deconstruction of the fundamental frequency and number of the corresponding sinusoid harmonic frequency can be mathematically expressed in terms of sums of all the sinusoidal signals given as :

$$f(x) = \frac{a_0}{2} + a_1 \cos x + b_1 \sin x + a_2 \cos 2x + b_2 \sin 2x + \cdots + a_n \cos nx$$

$$+ b_n sin\, nx$$

$$= {}^{a_0}/_2 + \sum_{n=1}^{\infty} a_n \cos nx + \sum_{n=1}^{\infty} b_n \cos nx \qquad (2.1)$$

$$a_0 = \frac{1}{\pi}\int_0^{2\pi} f(x)\, dx \quad , \; a_n = \frac{1}{\pi}\int_0^{2\pi} f(x) \cos nx\, dx \quad , b_n = \frac{1}{\pi}\int_0^{2\pi} f(x) \sin nx\, dx$$

$$c_n = \sqrt{a^2{}_n + b^2{}_n}$$

$$\emptyset_n = \tan^{-1}\frac{b_n}{a_n}$$

where f(x) is given as a generic periodic of a waveform, a_0 is given as the DC components, a_n and b_n are the coefficients of the series, n is the component value between 1 and infinity, and given the period t = 2π. The respective magnitude of each series can be defined as c_n, and the phase angle $\emptyset_n$ can be found as stated equation.

An alternative perspective on the harmonic is obtainable by visualizing their levels graphically. The representation can be accomplished by creating a harmonic spectrum that illustrates the magnitude or phase angle associated with each frequency component. By referencing the spectrum display, it is possible to identify and address the source of the harmonics. Typically, the harmonic spectrum indicate the levels of the harmonics as a percentage of each component in relation to the fundamental component for a given base frequency, as depicted in Figure 2.3.

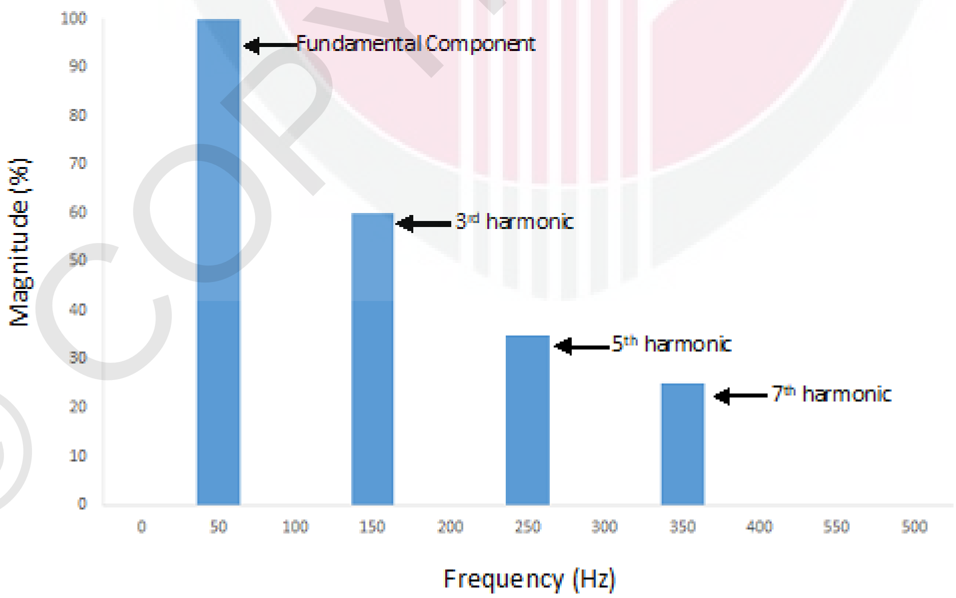

Figure 2.2: Harmonic spectrum of a harmonic-distorted waveform with the fundamental frequency of 50 Hz

Aside from evaluating the waveform using the harmonic spectrum, an index or parameter is also utilized in the metering and comparison of harmonic contents of waveforms. An index used for measuring the effective value of harmonics into a single quantity for easy monitoring is specified as a total harmonic distortion (THD) [33]. The definition given of THD for both voltage and current are stated as follows:

$$Voltage\ harmonics = 100\frac{\sqrt{V^2{}_h}}{V_1} \tag{2.2}$$

$$Current\ harmonics = 100\frac{\sqrt{I^2{}_h}}{I_1} \tag{2.3}$$

where I_h and V_h are the sums of value for current and voltage harmonics, respectively, in terms of root means square (RMS), while V_1 and I_1 are the RMS value of the fundamental voltage and current.

The THD of voltage is determined as the aggregate of voltage harmonics with the fundamental voltage. The THD of current is calculated by summing up the current harmonics in relation to the fundamental current. Voltage is consistently present in situations without fault, providing a reliable reference. However, this does not hold for the current. The main predicament is that the fundamental current may fluctuate during the load value changes. Consequently, if the loads are switched off, the fundamental current drops. Since it is being utilized as a reference, any noise in the system will display high levels of THD when the fundamental reference approaches zero.

Regarding these conditions for THD of current, another indices method, total demand distortion (TDD), is used. TDD is used for measuring current distortions, where the current harmonics are summated and compared to the maximum average current recorded during the test interval. The advantage of this method is that even when the current is low, the TDD value will not give misleading results of the effect of THD on the whole system. Based on this, TDD measurements can be easily compared and analyzed between multiple power quality changes of loads using a fixed reference value.

$$TDD = \sqrt{\frac{sum\ of\ the\ squares\ of\ the\ amplitude\ of\ all\ the\ harmonic\ order}{square\ of\ the\ amplitude\ of\ the\ average\ \max current\ interval}} \times 100\% \qquad (2.4)$$

Thus, the levels of harmonic distortion can be characterized using harmonic spectrum, THD, and TDD approaches. Once the sources of harmonic problems and the degree of harmonic distortion they imposed are identified, action can be taken toward effective mitigation solutions to confine and eliminate them.

2.3.1 Sources of Harmonic Current Distortion

In daily life, contamination of harmonics is common within the power system due to increased application of power electronics equipment and field-effect transistor (FET) based electronic converters. However, the sources of current and voltage harmonics can be distinguished into three main major categories.

The first category is the magnetic core equipment. The major magnetic core equipment used in the power system is the transformer[34][35]. Transformers can be considered as the initial sources of power system harmonics. The fundamental reason behind this lies in the non-linear relationship between the primary voltage and current caused by the shape of the magnetization curve. This non-linear behavior is particularly pronounced when the transformer operates within the saturation region, thus as a result, harmonics are generated and contribute to the overall harmonics content in the power system. Similar to a transformer, an electric motor is also a magnetic core equipment that produces harmonics during its process of producing the magnetic field [36]. However, due to the air gap in its construction, motor magnetizing is more linear than a transformer. Thus, its contribution to harmonics is relatively low. The second category is the harmonics due to the arc furnaces, arc welders, and high-pressure discharge lamps [37]. All these sources involve the high usage of power in the melting process and the arc furnace process specifically contributes harmonics due to abrupt initiation and interruption of current flow, causing considerable disturbance to the high impedance circuit [38]. Nonetheless, switch mode approaches, which operate as a non-linear load or disturbance generator, impair the quality of the power supply which arc welders commonly use.

Power electronics and electronic pieces of equipment produce the third category of sources [39]. The common equipment found in this source is fluorescent lighting, which is widely used in residential and industrial settings. With the advent of electronic ballasts, fluorescent lighting has become more efficient than the previous magnetic ballast technology [40]. Nevertheless, the electronic ballast method that regulates fluorescent lighting generates harmonics in the electrical supply system. The second most common category of components in this source is the switched mode power supply (SMPS)[41], which has seen a significant surge in usage due to the proliferation of electronic devices such as smartphones. SMPS mainly consists of a single-phase rectifier powered by switching components, where SMPS has replaced the transformer application. The charging and discharging of the reservoir capacitor derived from the rectifier produces the output voltage and current. However, this process results in a non-continuous pulse current with a high concentration of harmonics.

Another major piece of equipment that falls under this category is the three-phase rectifier-based device. Usually, the three-phase rectifier is used in equipment that involves static converters, especially variable speed controllers, uninterruptible power supply (UPS), and ac to dc converters. These devices are commonly another source of harmonics toward the supply system, as they usually involve using bridges in their construction.

In conclusion, the prevalence of harmonics in power systems, stemming from diverse sources like magnetic core equipment, high-power devices, and power electronics equipment, underscores the need for diligent management and mitigation strategies. The non-linear behaviors exhibited by these sources, whether due to magnetization curves, high-power consumption, or rectification processes, contribute significantly to harmonic distortion, thereby impacting power quality and system reliability. As reliance on power electronics continues to grow, addressing these harmonic sources becomes increasingly imperative to ensure the stable and efficient operation of modern power systems. By understanding the mechanisms behind harmonic generation and implementing appropriate measures through mitigation, the adverse effects of harmonics can be reduced, ultimately safeguarding the integrity of our power supply and sustaining optimal performance for diverse applications.

2.3.2 Effect of Harmonics

Throughout the power system, when there is a trend of rising harmonics attribution, there tends to be a detrimental impact on various components within the system. In terms of the component's details, the effect of harmonics is stated individually. The compilation that arises within the harmonics can be considered a simple and direct effect of the signal contamination of the current flow. Abnormal heating of materials and interruption of operations are two of the keys issued accustomed with the current harmonics.

The first affected component is conductors. As metallic-based components, abnormal heating can be considered the most damaging effect caused by current flow harmonics. Due to the power loss effect, heat will always be the product of current flow within the conductor resistivity. This problem is intensified by additional harmonics currents through how deep the currents penetrate the material's conduction, also known as the skin effect. The effect is proportional to the frequency, where increased harmonics order will contribute to increased skin effect. As greater current density will focus near the conductor's surface, the conductor's impedance will increase, contributing to a more significant loss in terms of I^2R.

Induction motor, as the second affected component having construction which almost similar features to the transformer[42]. Due to this, it is also subjected to iron and copper losses, especially in the rotor iron core and stator winding and rotor circuit. The skin effect also magnifies these losses, especially when the frequency is above 300 Hz. The main impact of harmonics on induction motors is an overheating effect due to iron and copper losses, especially in the stator winding. The impact of overheating is the shorter lifespan of the induction motor and decreased efficiency, vibration, and noise.

Transformer, meanwhile, is subjected to harmonic-related problems due to skin effects and eddy current losses[43]. Eddy current is the product of the AC magnetic field and involves circulation within the transformer core, opposing the core magnetic flux. In terms of losses, eddy current losses are related to I^2R variety and proportionally contributed to the frequency square. An increase of just two or three orders of harmonics will affect more significant losses, which will usually cause shorter operational life due to prolonged transformer overheating.

Another component effected is capacitor as capacitor's having characteristics of the decreasing impedance with increased frequency [32]. Thus, as the harmonics increase within the current's flows, the more the capacitor acts towards as a short, which shows that the capacitor is attracted to high frequencies harmonics. The harmonics result in the capacitor going into overload due to increased current flow. Another discrepancy regarding capacitors and harmonics is the likelihood of both components' resonance. When resonance occurs, it will affect the capacitor and other system parts in terms of severe and destructive damage.

Harmonics also pose significant challenges to battery in terms of multiple issues. Firstly, harmonics induce overheating within batteries by elevating temperatures and accelerating chemical reactions within the battery. This phenomenon expedites the degradation of electrolytes and electrode materials, compromising battery integrity. Additionally, high harmonic levels increase internal resistance within batteries, thereby reducing batteries effective capacity and leading to shorter discharge times. Moreover, harmonics accelerate the aging process of batteries through rapid cycling induced by fluctuating harmonic currents, causing mechanical stress and chemical degradation, ultimately shortening their lifespan. Furthermore, harmonics cause voltage fluctuations within the electrical system, disrupting the charging and discharging processes of batteries and potentially resulting in overcharging or undercharging, both of which can harm battery health. Finally, harmonics can induce corrosion in battery terminals and interconnecting cables due to heightened electrical stresses and current densities, further impeding battery performance.

Lastly, devices embedded with power electronics components can be highly sensitive toward interruption to harmonics distortion due to reliance on the voltage waveform for timing information. Zero crossings are usually applied in power electronic devices to define the component firing sequence. Subsequently, if the waveform for the zero crossing is shifted, it can lead to malfunction of operation. Nonetheless, most of the semiconductor switches depend on zero voltage operation to avoid electromagnetic interference and inrush current, and any deviation of the zero crossing can again contribute to the malfunction of the devices. One of the power electronic supply characteristics is the dependence on the supply voltage peak value to maintain the capacitor at full charge. An increase in harmonics distortion can lead to increasing or decreasing of the voltage supply waveform. The power supply may operate under or over standard voltage specifications, although the RMS may seem normal. Generally, if this occurred, it could also cause device malfunction.

In conclusion, the rising harmonics attribution within the power system can have a detrimental impact on various components within the system. The most affected components include conductors, induction motors, transformers, capacitors, and electronic devices. Each component is impacted differently by the harmonics, such as abnormal heating of conductors, overheating of induction motors, eddy current losses in transformers, overloading of capacitors, and malfunction of electronic devices. It is crucial to manage and control harmonics distortion within the power system to avoid damage to these components and ensure the reliable operation of the power system.

2.3.3 Harmonic Standards

The Institute of Electrical and Electronics Engineers (IEEE) has issued guidelines on harmonics based on IEEE 519-1992 (updated 2014) [44]. These standards outline important harmonic sources in power systems, illustrate system response to harmonic, and examine harmonic distortion's consequences on device and load operation. The standard also covers harmonic level determination methodologies and measurement requirements in power systems. Methods for creating reactive compensation and best practices for reducing harmonic distortion to acceptable levels for consumers and utilities are also discussed.

IEEE Standard 519-1992 shown in table 2-1 is extensively used as the reference standard since it provides comprehensive harmonic concerns guidance. It is the first standard to address harmonic issues in electrical power systems. Most research works in APF cite IEEE standard 519-1992, which specifies the 5% THD limit in electrical power systems [45].

Table 2.2: Current distortion limits for systems rated 120 V through 69 kV [44]

Maximum harmonic current distortion in percent of I_L						
Individual harmonic order (odd harmonics)[a, b]						
I_{SC}/I_L	$3 \leq h < 11$	$11 \leq h < 17$	$17 \leq h < 23$	$23 \leq h < 25$	$35 \leq h < 50$	TDD
< 20c	4	2	1.5	0.6	0.3	5
20< 50	7	3	2.5	1	0.5	8
50< 100	10	4.5	4	1.5	0.7	12
100< 1000	12	5.5	5	2	1	15
>1000	15	7	6	2.5	1.4	20

[a]Even harmonics are limited to 25% of the odd harmonic limits above.
[b]Current distortions that result in a dc offset, e.g., half-wave converters, are not allowed.

Table 2.3: International standard IEC 61000-3-2 [45]

Harmonic order	**Limits class A (A)**	**Limits class B (A)**	**Limits class C.**	**Class D (i)**	**Class D (ii)**
2	1.08	1.62	2	–	–
3	2.30	3.45	30*λ (*2)	3.40	2.30
4	0.43	0.64			
5	1.14	1.71	10	1.90	1.14
6	0.30	0.45			
7	0.77	1.15	7	1	0.77
8	0.23	0.34			
9	0.40	0.60	5	0.50	0.40
10	0.18	0.27			
11	0.33	0.49	3	0.35	0.33
12	0.15	0.22			–
13	0.21	0.31	3	0.29	0.21
14	0.13	0.19	–	–	–
15	0.15	0.22	3	0.25	0.15
16	0.11	0.16	–	–	–
17	0.13	0.19	3	0.22	0.13
18	0.10	0.15	–	–	–

Limits class C. Harmonic current limit expressed as a percentage of the 50 Hz input current (%)
Class D (i) Permissible harmonic current per Watt input power (mA/Watt) (*1)
Class D (ii)Permissible harmonic current (A) (*1)

The International Electrotechnical Commission (IEC) shown in table 2-2, widely acknowledged as the curator of power quality standards, is another international institution working on detailed harmonic limits rules. IEC has created a set of standards known as Electromagnetic Compatibility (EMC) to deal with power quality difficulties. The IEC 61000 series concerns harmonics and interharmonics in low-frequency electromagnetic phenomena [46]–[48]

2.4 Harmonics Mitigation Techniques Using Power Filter

Harmonic power filters are filters utilized in electrical power networks to mitigate harmonic components produced due to the usage of nonlinear loads. The most frequent forms of harmonic power filters that are being employed are passive power filters, active power filters, and hybrid power filters, which is the combination of both. The usage of the filter type is usually influenced by the harmonic types and the severity of harmonics. Another factor contributing to the selection of filters being used in the electrical system is the characteristics of the harmonics. However, while filters are commonly employed to mitigate harmonics by providing low impedance paths to specific frequencies, their improper design or integration can inadvertently exacerbate the resonance phenomenon. This occurs when the frequencies targeted by the filters coincide with the resonant frequencies of the system's components, leading to amplification of harmonic currents or voltages. The consequences can range from equipment damage to system instability, posing significant challenges to the reliability and safety of the power network. Addressing harmonic resonance requires meticulous planning and design, encompassing proper sizing and placement of filters, consideration of system impedance, and in some cases, the implementation of active control strategies.

2.4.1 Passive Power Filter

In terms of design, capacitors, inductors, and resistors are the main components used to construct a passive power filter. As for the harmonics mitigation of voltage, current, and reactive power in an AC power system, the passive power filter is divided into topology, connection, and supply systems [4]. Low and high pass filters are the two main filters used in the system [37]. A low pass filter is applied to allow low-frequency power below the cutoff frequency to pass through. On the other hand, the high pass filter only permits high-frequency power over its cutoff frequency to pass. Meanwhile, the bandpass filter only allows a specified band of frequencies to pass, and at the same time filtering out higher or lower signals than the specified band of frequencies. Lastly, the band stop filter is the inverse of the bandpass filter. It blocks signals in a specified frequency band while allowing others to pass through. Variant types of passive filters configurations are depicted in Figure 2.4.

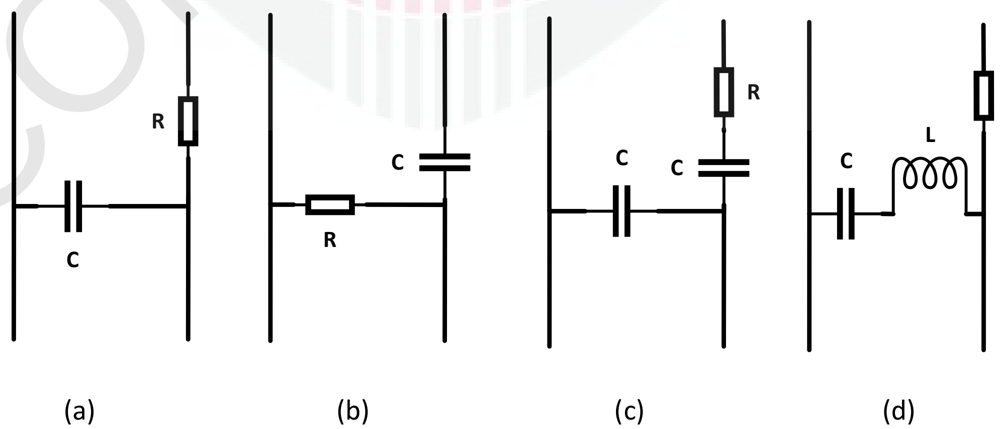

Figure 2.3: Types of passive power filters configurations: (a) low pass filter, (b) high pass filter, (c) band pass filter, and (d) band stop filter [7].

The passive filter is widely employed in power systems because of its low cost, dependability, and simplicity. Its most common applications include industrial installations with more than 500 kVA nonlinear loads, power factor correction, as well as voltage and current distortion reduction to avoid any disturbances to sensitive loads or overloads. This filter is typically coupled in parallel with nonlinear loads to provide low-impedance alternatives for specific harmonic currents exclusively. As a result, the distorted currents can be restored to their original sine wave pattern.

Although within the simplicity of the design, the underlying disadvantage of a passive filter is that its design dictates the need to tune the filter to a specific harmonic frequency, which is usually limited to a single specified type of load [7][49]. Due to this requirement, the filter may fail to solve random changes in an AC system, resulting in resonance effects [50]–[52]. Another criterion that needs to be considered is that multiple harmonics may require additional filters.

2.4.2 Active Power Filter

The Active Power Filter (APF) represents an advanced technological solution for addressing power quality issues, particularly harmonics. Employing solid-state semiconductor power switches such as metal-oxide-semiconductor field-effect transistors (MOSFETs) and insulated-gate bipolar transistors (IGBTs), along with passive components, APFs improve power conditions by filtering, dampening harmonic components, managing reactive power for power factor correction and voltage regulation, balancing three-phase loads, and mitigating voltage flicker. APFs are available in four primary configurations: series, parallel (shunt), hybrid APFs, and unified power quality conditioners (UPQC).

Series APFs are specifically engineered to protect sensitive loads from voltage distortions by eliminating voltage harmonics, thereby ensuring that loads receive a pure sinusoidal supply voltage [53]–[55]. These filters are classified into three categories: single-phase two-wire, three-phase three-wire, and three-phase four-wire. By injecting the appropriate voltages in series between the Point of Common Coupling (PCC) and the load, series APFs effectively address most voltage-based power quality issues [56]–[58]. They provide sinusoidal balanced voltage across linear loads with a self-supporting DC bus, making them particularly effective at reducing harmonics in supply current for voltage-fed nonlinear loads with relatively low ratings, such as diode rectifiers with large DC bus capacitors.

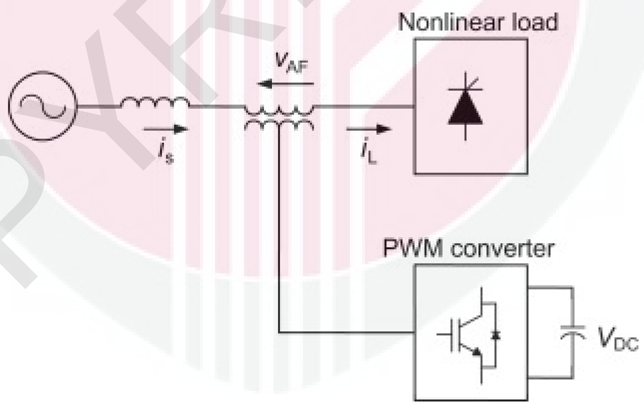

Figure 2.4: Series Active Power Filter Configuration [58].

APFs exhibit superior and flexible performance compared to passive filters, as they can simultaneously suppress multiple harmonic currents and operate independently of the power system's impedance characteristics, thus avoiding resonance issues. The integration of voltage source inverters (VSIs) in series APFs facilitates precise and dynamic compensation of voltage harmonics in real-time. This precise modulation ensures a stable and reliable power supply, minimizes disruptions caused by harmonic distortions, and enhances the performance and efficiency of electrical systems and equipment. Consequently, APFs are well-suited for demanding conditions where passive filters may be ineffective due to resonance issues as APFs can operate independently of the power system's impedance characteristics.

2.5 Shunt Active Power Filter

With the proliferation of non-linear loads and renewable energy sources, harmonic distortion and reactive power imbalance have become significant concerns for power utilities. Shunt active power filters (SAPFs) are a promising solution to address the power quality problems associated with modern power systems, especially when dealing with the related issues of current. SAPFs, when connected in parallel to the load, can effectively mitigate harmonic components and enhance the reactive power compensation, thereby improving the overall power quality. Due to their scalability and flexibility, SAPFs have gained significant attention from researchers and industry practitioners, leading to numerous studies and applications in recent years [59]. Thus, a review of SAPFs includes the principle of operation, control strategies, and the latest development and challenges in their implementation.

2.5.1 Principle Operation of Shunt Active Power Filter

SAPF construction usually consists of a voltage source inverter (VSI) and attached to a DC-Link capacitor functioning as a voltage storage for the system, as shown in figure

2.5. The VSI is typically connected in parallel with the voltage supply and the nonlinear loads. Generally, during installation, the SAPF is placed within the PCC near the end user side or, in most cases, directly at the nonlinear loads themselves. Since the primary function of the SAPF is to reduce the harmonic currents caused by nonlinear loads, it must be capable of providing instantaneous compensation directly to the sources[23].

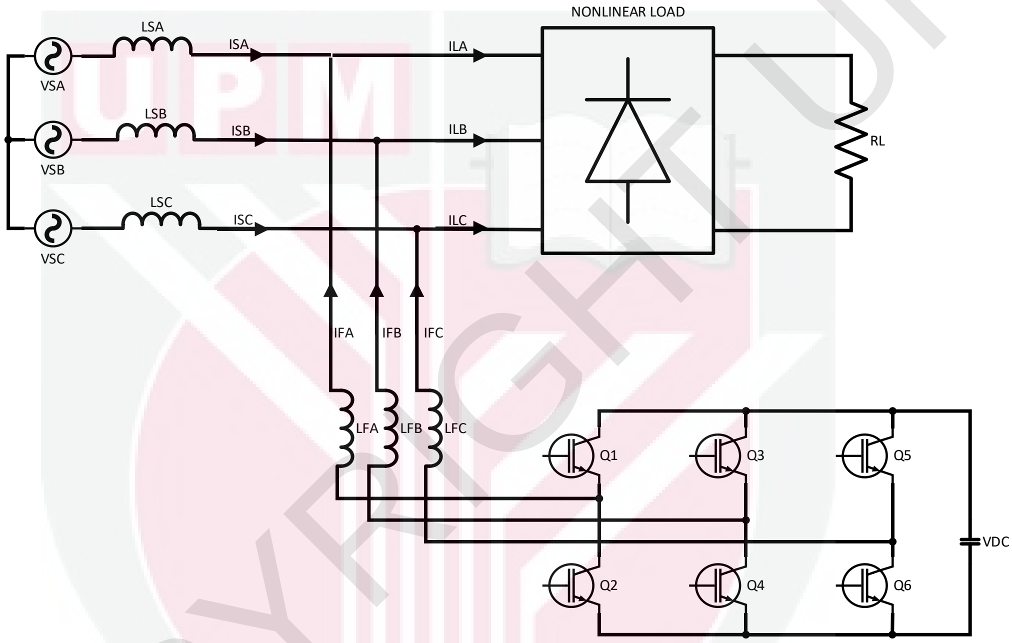

Figure 2.5: Block Diagram of SAPF in the system [23].

To mitigate the harmonics, the SAPF injects a specific value of AC current in phase but with amplitude inversion of harmonic current to the main power system. The current is known as the instantaneous filter current, denoted as if(t). As a result, the distorted waveform of the instantaneous supply current $i_S(t)$ will be reformed back to sinusoidal in shape, and the current phase will also be on par with the instantaneous supply voltage Vs(t). In other terms, the VSI uses the capacitor as a selfregulation source is required to draw some amount of regulating power from the power system. The current drawn from the power supply to maintain the voltage within the capacitor is known as instantaneous DC-link charging current, denoted as $i_{dc}(t)$. However, these changes will not affect any characteristic of the instantaneous load current $i_{LS}(t)$. The sums of all instantaneous currents that are taking place at the PCC can be represented as:

$$i_S(t) = i_{Ls}(t) - i_F(t) + i_{dc}(t) \quad (2.5)$$

Utilizing the Fourier series, the distorted $i_{Ls}(t)$ waveform can be divided into two current components [40] which included the instantaneous fundamental load current $i_{Fund}(t)$ and the instantaneous harmonic load current $i_H(t)$. Based on this consideration, the $i_S(t)$ in equation (2.3) can be expanded as:

$$i_S(t) = i_{Fund}(t) + i_H(t) - i_F(t) + i_{dc}(t) \quad (2.6)$$

During the mitigation process, if the compensation current $i_F(t)$ is equal in magnitude to the harmonics current $i_H(t)$, at this point, the anticipated instantaneous compensated supply current $i_{S,comp}(t)$ can be calculated as;

$$i_{S,comp}(t) = i_{Fund}(t) + i_{dc}(t) \quad (2.7)$$

Based on equation 2.7, it can be confirmed that after applying the SAPF at PCC, the supply current will be able to supply fully sinusoidal fundamental current throughout the nonlinear load operations. Additionally, the supply current can also provide the corresponding DC-Link charging throughout the SAPF operation period. Simultaneously while operating with SAPF, the power system must supply real power for the operation of the nonlinear load and real power for regulating the DC-link voltage and compensating for SAPF's power loss [60], [61]. In general, the operation of SAPF is highly dependent on their control system. Figure 2.6 illustrates the fundamental components of a control system within the digital implementation. As depicted in the figure, the control system mainly comprises of three algorithms.

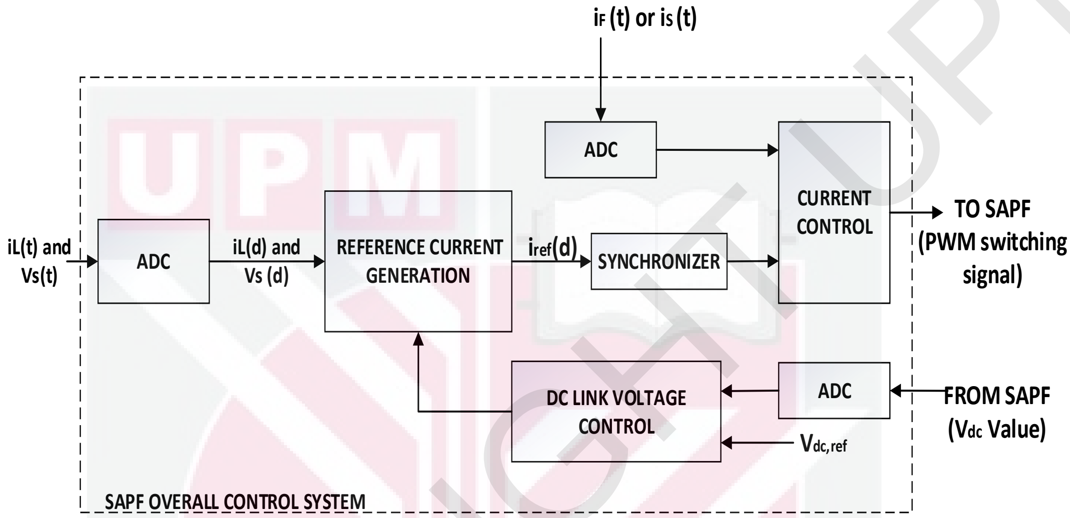

Figure 2.6: Basic Control of SAPF in the system

The mentioned algorithms are for generating reference current, current control, and DC-link voltage control. The operation of these algorithms is interdependent with one another. Additionally, the current control algorithm must respond faster than the voltage control algorithm for better performance. Thus, dynamic behavior of both control algorithms can be improved to achieve better control. Table 2.4 summarises the functions of all control system components which includes Analogue-to-Digital Converter (ADC), Reference Current Generation, Current control, DC-Link Voltage Control and Synchronizer.

Table 2.4: Functions of all components of the control system

Component/Algorithm	Function
Analogue-to-Digital Converter (ADC)	Conversion of the analog measurement into a digital signal for all measured signals.
Reference Current Generation	Based on the digital signal input supplied, which are the load current iL(d) and supply voltage vS(d), the algorithm will produce the appropriate digitally time-based reference current signal $iref$(d).
Current control	To control the digital signal compensation current signal iF(d) by generating Pulse-Width-Modulation (PWM) switching signal.
DC-Link Voltage Control	To regulate the digital DC-link voltage signal Vdc(d), for maintaining according to the reference value.
Synchronizer	To coordinate the phase of $iref$(d) according to the phase of an operating power system. As a result, the SAPF's functioning

2.6 Reference Current Generation

An indispensable aspect of the operation of APFs is the availability of reference voltage or currents, which serve as a guide for the flow of APFs. Ensuring that the injected current of SAPFs is in sync with the reference current is a critical aspect of SAPF operation. Various algorithmic methods have been thoroughly examined and proposed to generate appropriate reference currents. These algorithms are typically categorized as time-domain and frequency-domain extraction methods [62], and they are used to determine, approximate, and extract harmonic components from load currents [63]. Figure 2.7 illustrates the different types of reference current generation algorithms that will be discussed in greater detail in subsequent sections of this chapter.

2.6.1 Frequency-domain Algorithms

Frequency-domain techniques, in general, are used to extract harmonic components of load currents where the components are represented as amplitudes in terms of their respected frequency components. Fast Fourier transform, wavelet-packet transform, and Kalman filter are commonly used frequency-domain techniques. In the context of operation, frequency domain techniques usually rely on the periodic characteristics of distortions because the control signal is generated based on past distortion patterns. Compared to time-domain techniques, these extraction algorithms are infrequently utilized in functioning SAPF attributed to factors such as complexity, historical practices, cost considerations, and the suitability of time-domain techniques for addressing a wide range of power quality concerns effectively and efficiently.

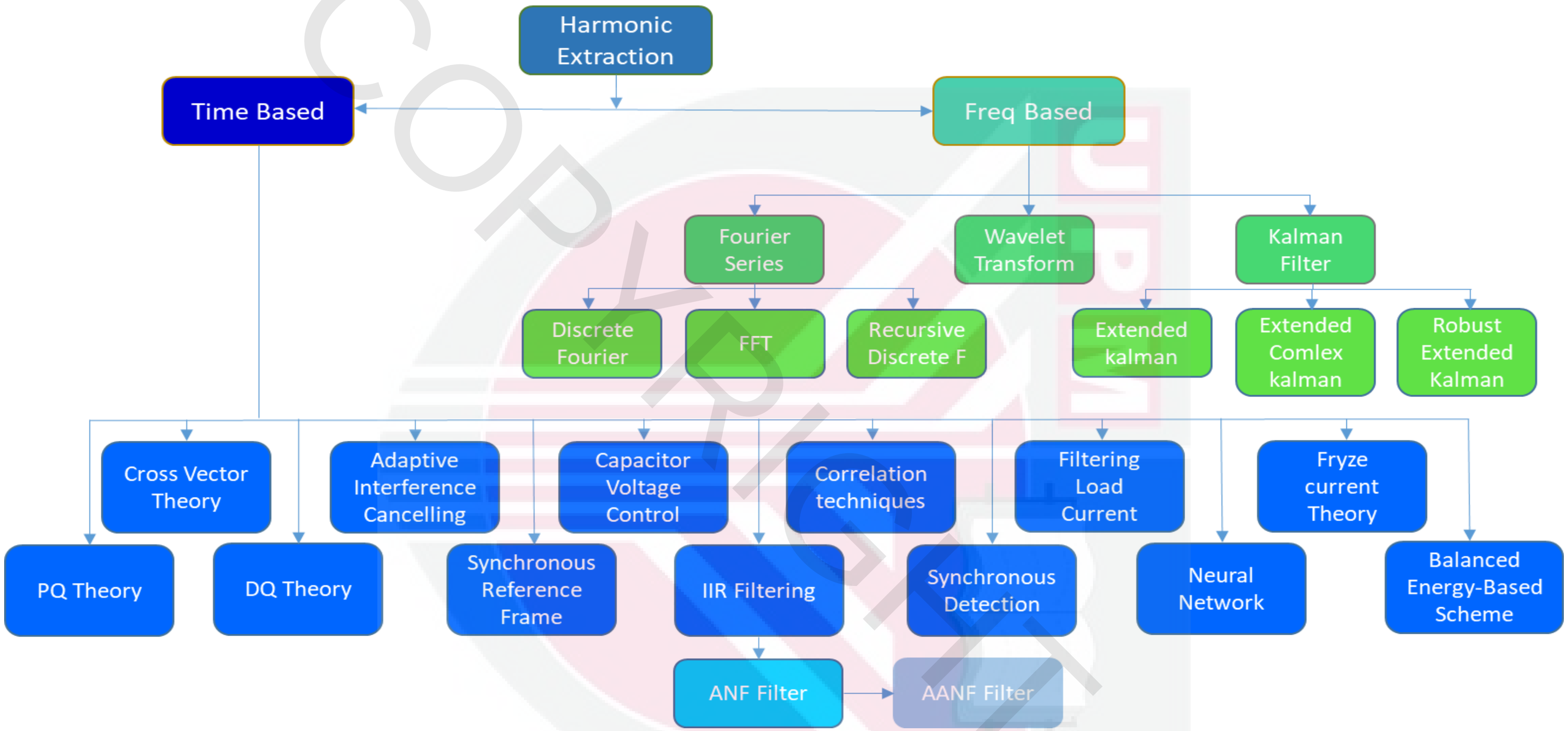

Figure 2.7: Various types of harmonic extraction algorithms

2.6.1.1 Fast Fourier Transform and Discrete Fourier Transform

Fast Fourier transform (FFT) method was developed from the standard Fourier series. FFT was created to calculate the harmonic components within periodic signals. As the FFT progresses to discrete Fourier transform (DFT), the extraction technique is improved in terms of simplification of implementation, quick extraction algorithm computation speed, and steady-state accuracy.

This extraction approach, however, has a major drawback where it requires a constant periodic input signal with no time-varying frequency to work correctly. Significant mistakes in magnitude and phase angle can be introduced when there is a considerable frequency variance in the FFT [64]. The algorithm requires data for at least one complete cycle to work properly, causing a slow dynamic response especially when involved in SAPF computing [65]. As a result, the time it takes to collect enough data samples increases. Also, due to buffer and de-buffer procedures that occur in two continuous cycles, the recovered harmonic components are two cycles out of date. As a result, they are suited for low-variable load circumstances.

Furthermore, for frequency domain algorithms to have accurate representation of the waveform frequency components [66], it is advantageous to sample the signal at the points where the zero crossing occurs. Otherwise, spectral leakage and picket-fence effects will occur [67]. In addition, for actual applications, strict synchronization between sampling and the fundamental frequency is required in order to reduce leakage effects of DFT [68]. Some researchers use countermeasures such as windowing, interpolating, and harmonic grouping to improve this extraction process.

In addition, although the DFT is computationally efficient, it is susceptible to the accumulation of mistakes and instability [68]. Upgraded algorithms, while potentially offering improved accuracy and capabilities, may come at the cost of increased computational load [69]. Furthermore, many DFT-based methods still require a complete data cycle to function accurately.

2.6.1.2 Wavelet-packet Transform.

The wavelet-packet transform (WT) algorithm was developed to address the lack of time frequency localization FFT algorithms. The advantages of the WT method are that it requires a short duration oscillating waveform instead of a whole cycle of the stationary waveform [70], [71]. As a result, extracting harmonic components of nonperiodic signals (containing a stationary component and a transient signal, which are common in power quality (PQ) disturbances) is achievable [72].

However, the realization of this extraction procedure is entirely dependent on the mother wavelet functions and the finite-impulse response of digital filter. It also inherits the problem of time delays and a large computational overhead [63] .

2.6.1.3 Kalman Filter

The Kalman filter is a series of mathematical equations that employ noisy and erroneous measurement data to create a computationally efficient (recursive) technique for estimating the past, present, and future states of a dynamic system, making it particularly valuable in fields such as control systems, navigation, and signal processing [73]–[75]. This approach has been extensively researched and applied in a variety of settings. In the APF, reference generation is critical for achieving the compensation goal. The Kalman filter calculates and tracks current harmonics of the grid and assumes the grid frequency to be constant. A mathematical model based on a single-phase filter that can recognize harmonics and unbalance with less computational effort has recently been developed. However, because the derivation based on axis rotation is applied to the model, the method indicates constant frequency under a time-variant model, which has certain drawbacks in terms of constant frequency [76]–[78]. In the digital approach described, the time-invariant reduces the computational effort required. As a result, frequency variation is considered, which uses an extended Kalman filter to determine the grid's frequency [79][80]. This concept, however, suffers from oscillations during frequency transients, which are unsuitable for process control, and it is also incapable of rejecting amplitude transients in the voltage [81]. Extended Kalman Filter linearizes the nonlinear process and measurement models around the estimated state to perform state estimation using linear equations. While this linearization is an approximation and may introduce errors, it allows the Kalman Filter to work with nonlinear systems by iteratively updating state estimates based on new measurements [82]. As this technique uses the most recent available estimates; therefore, the propagation equations are valid when both estimate real states are almost identical.

2.6.2 Time Domain Algorithm

The time domain algorithm is an algorithm that studies the signal or function's value where the signal is seen as real numbers at various separate instances in discrete time or continuous time. This domain plays a crucial role in the APF as it works in real computational time and does not involve changing the data. Thus, the algorithm should be able to work faster and more straight forward with implementation on minimum computational steps when compared to the frequency domain algorithm. Due to this characteristic, the commonly studied algorithm in the APF is based on the time domain. Three time-domain algorithms that are frequently implemented to generate reference currents are the instantaneous reactive power theory, the synchronous-frame-based transformation, as well as the balanced energy-based scheme. However, based on the current studies, many more branches of time domain algorithms arise, such as adaptive interference canceling, neural networks, and adaptive notch filters.

2.6.2.1 Instantaneous Reactive Power Theory

The instantaneous reactive power theory, commonly known as instantaneous real and reactive power theory (p-q theory). Its primary function is to calculate or extract instantaneous real power and reactive power of loads within three-phase systems. This method involves the conversion of both the supply voltage and load current, and it is done in two different planes. The first transformation is the conversion from a-b-c coordination, a three-phase stationary reference frame, to α-β coordination, which is a two-phase stationary reference frame [83], [84]. The second transformation is achieved by utilizing the Clark-Concordia transformation. The transformation between these two types of coordination is shown in Figure 2.8.

Based on this extraction algorithm, DC and AC components can be obtained by calculating the instantaneous real and reactive power where Low Pass Filters (LPFs) or High Pass Filters (HPFs) are applied to extract these two components individually.

However, when using these filters, time delays occur because these filter applications can degrade the dynamic performance of SAPFs [85], [86].

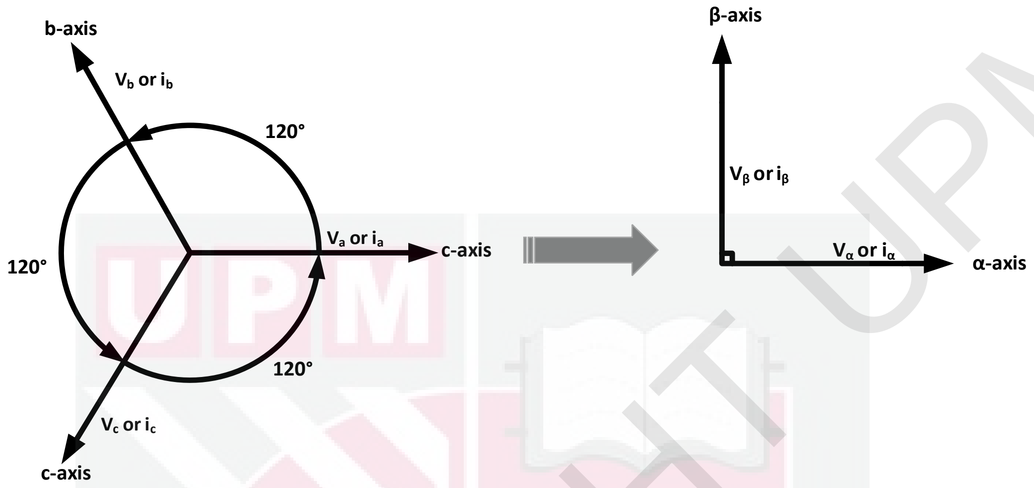

Figure 2.8: Voltage and current transformation for an instantaneous power theory [62].

In addition, the accuracy of the extraction algorithm can deteriorate in two situations, an imbalanced three-phase system and a distorted three-phase supply voltage. As a result, only balanced three-phase system with undisturbed three-phase supply voltage is proposed to employ this extraction procedure [87], [88].

Furthermore, the transformation (from a-b-c coordination to α-β coordination) and de-transformation (from α-β coordination to a-b-c coordination) processes apply complex mathematical equations which require high speed and high accuracy of Digital Signal Processing (DSP) [89]. And for the implementation of the algorithm, high numbers of voltage and current transducers are needed for the transformation processes [62].

Another important criterion in applying the algorithm is synchronization of the phase of generated reference currents, usually obtained using Phase-Locked Loops (PLLs) or Zero-Crossing Detectors (ZCDs) [90].

2.6.2.2 Synchronous Frame Based Transformation

The synchronous-frame-based transformation known as d-q transformation, is a more dependable extraction method when dealing with unbalanced three-phase systems. The transformation is based on the transformation to a two-phase system from a three-phase system using a rotating system at angular velocity ω (synchronous speed) [91]. This technique is called instantaneous active and reactive current theory (id – iq theory). This extraction procedure only transforms a three-phase load current. Applying this algorithm will involve two stages of current's transformation. First from a-b-c coordination to α-β coordination and followed by from α-β coordination to rotating d-q coordination using the Park transformation [92].

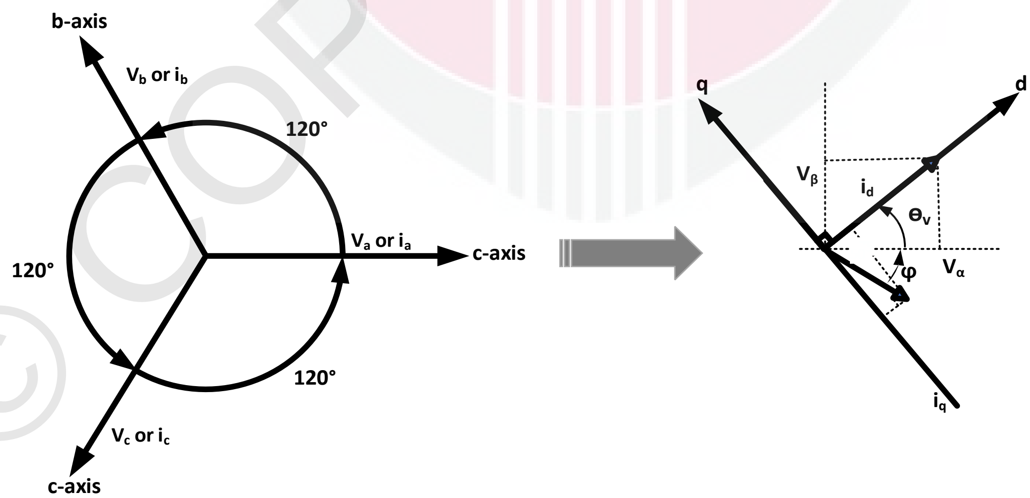

Figure 2.9: Illustration of the transformation from a-b-c coordination to d-q coordination [93].

Compared to the p-q theory, the load currents in the d-q coordinate can also be divided into two main components which are the DC and AC components. Subsequently, Low Pass filters (LPF) or High Pass Filter (HPF) are applied to extract these two components [81]. A Phase Lock Loop (PLL) is necessary for the Park transformation process to acquire the sine and cosine functions of the three-phase supply voltage. Indirectly, applying the PLL will result in the phase of a reference current created to match the phase of power systems in operation [56].

In some applications of the d-q algorithm, the function of PLLs is substituted by calculation for angle θv of instantaneous supply voltages [93], [94]. However, this modification complicates the extraction algorithm as it necessitates the conversion of the three-phase supply voltage from a-b-c coordination to α-β coordination.

Typically, various voltage and current transducers are needed for the d-q transformation, and applying low-pass or high-pass filters will contribute to time delays [95]. As a result, it will impact SAPFs' dynamic performance.

2.6.2.3 Fryze Current Control

Fryze Current Control (FCC) is a control strategy used in APF to mitigate harmonic distortion and improve power quality in electrical power systems. The FCC strategy uses a combination of harmonic detection and control techniques to regulate the APF current to cancel out the harmonics generated by the load [96]. The FCC strategy is based on the instantaneous reactive power theory, which produces a reference current that is injected into the system to cancel out the harmonic current.

The Fryze minimization method introduces a power definition that decomposes power into active power and generalized reactive power [97]. This decomposition allows for accurate detection and analysis of harmonic currents [98]. The reference current is generated based on the frequency and amplitude of the harmonic current. The reference current is calculated by determining the minimized currents from the average values of the three-phase instantaneous active power and equivalent conductivity [99]. The proportional gain is used to reduce the steady-state error, while the integral gain is used to reduce the transient error. The PI controller uses the difference between the measured harmonic and reference currents to generate the control signal that regulates the APF's current which is used to adjust the controller's response to changes in the system. Another configuration that plays an important role within the FCC is the type of filter application within the algorithm. The filter used will influence the sensitivity of the algorithm response.

One of the limitations of the FCC strategy is that it has a limited range of harmonic cancellations. The FCC strategy can only cancel out harmonics up to a certain frequency. Beyond the defined frequency, the performance of the APF decreases, and the THD level increases. This limitation may not be suitable for applications requiring high harmonic mitigation levels [99].

In addition, the FCC strategy may have a slow response time, which may not be ideal for applications that require a fast transient response. The slow response time is due to using an integrator in the control loop, which introduces a delay in the system's response. The FCC strategy is also sensitive to variations in the system parameters, such as the PI controller gains and the reference current, which can affect the APF's performance and may require frequent recalibration.

2.6.2.4 Balanced Energy-Based Scheme

Balanced Energy Based Scheme exploits dc-link voltage regulation of SAPFs to estimate or extract the peak amplitude of reference currents. By maintaining the system's active power balance, this extraction algorithm states that the voltage control signal of a voltage controller can be regarded as the estimated peak amplitude of a reference current [100]. On the plus side, since the current measurement is unnecessary, this extraction algorithm has demonstrated a straightforward implementation. Furthermore, it can be used with both single-phase and three-phase systems [101].

The synchronization of the phase of generated reference currents is usually coordinated using PLLs or other synchronization algorithms [102]. However, the generated reference current is less accurate and any latency or errors in control signal processing can adversely impact the energy balance, potentially causing voltage deviations. It is because the estimated peak amplitude is entirely dependent on the control gain of the voltage controller [103].

Furthermore, maintaining a consistent energy balance requires continuous monitoring and adjustment, which may introduce complexities and necessitate sophisticated control algorithms [104]. This could elevate the cost of the control system and render the SAPF less economically viable, especially for smaller installations or systems with budget constraints.

2.6.2.5 Artificial Neural Network-Based Extraction Method

The artificial neural network (ANN) is widely utilized across technical domains and has recently gained popularity in power electronics. ANN techniques typically involve training procedures using different patterns and algorithms, which can improve current utility compensation for voltage and current harmonic distortion [105]–[108]. Weight-updating techniques facilitate quick reactions and adjust the learning parameters to reduce errors between actual and desired outputs. However, traditional ANN structures are challenging to execute due to their bulky nature, which requires extracting and measuring all current harmonic orders and also involves high computational load [109].

In response, Adaline-based neural networks have emerged as a robust alternative. Adaline's three-layer feed-forward structure simplifies the extraction process by reducing the convergence time [110]. For example, in a case where the 3rd and 5th harmonics need to be isolated from a noisy signal, Adaline can achieve this more swiftly and with less computational overhead than a traditional ANN [106]. Based on this Adaline-based techniques have been proposed for specific use-cases in power quality such as disturbance voltage regulation where Adaline can rapidly identify voltage sags and swells, including their harmonic components, thus facilitating faster corrective actions and harmonic estimation process [111]. Adaline's faster convergence enables timely and accurate estimation, even in dynamically changing conditions, especially in inverter control techniques.

While Adaline has some advantages for online harmonic extraction, it also has certain disadvantages. One limitation is that it may not be suitable for complex nonlinear problems and may require extensive training data to achieve accurate results [112]–[114]. Another disadvantage of Adaline is that it is sensitive to noisy input data and fundamental frequency drifts, which can lead to inaccurate predictions [115], [116]. Additionally, Adaline depend on the learning rate where the choices of the rate may cause instability within the Adaline [117].

2.6.2.6 Adaptive Notch Filter

In addition to the previously mentioned methods, the APF also employs the notch filter method, which is easy to design and handle changes in load. The adaptive notch filter was introduced in the study as a processing method for harmonics and interharmonics, using time domain signal analysis [118].

The ANF has been shown to have a high harmonic rejection ratio, which allows it to filter out unwanted harmonics effectively. However, the DC-Link control method or algorithm is not well-defined, which limits its ability to process information. Some studies have explored using ANF for three-phase applications, which can extract reactive harmonic currents and perform harmonic decomposition [119]. However, these studies have been limited to monitoring and extraction only and it has not yet explored the full potential of the ANF in controlling APF [120].

Other studies also have attempted to integrate the ANF into the PQ algorithm for shunt APF in a three-phase four-wire system. While this approach has shown promise, it has also increased the algorithm complexity, which can compromise the ability of ANF to filter the fundamental signal of the system directly [121]. This algorithm uses the ANF transformation process, and integration must be included for filtering purposes.

While the ANF has shown potential as a powerful processing method for harmonics and interharmonics in APFs, further research is needed to explore its full potential and develop more efficient control methods that take full advantage of its capabilities.

2.7 DC-link Voltage Control Algorithms

The DC-Link capacitor is essential in SAPF, primarily for maintaining constant DC voltage and providing power during transients, thus minimizing power fluctuations due to reactive power correction [122]. Harmonic currents can disrupt the power balance, necessitating the DC capacitor to compensate, which may alter the DC voltage from its reference value. The DC-Link Voltage controller corrects these discrepancies to maintain stable output power [123]. Various algorithms like sliding mode control, fuzzy logic, and conventional PI voltage regulators are being researched to optimize DC-Link voltage, minimizing disruptions and balancing instantaneous power mismatches.

Sliding Mode Control (SMC) for DC links in active power filters operates on nonlinear principles, adjusting system dynamics to ensure convergence towards specific conditions [124] [125]. SMC enhances performance by allowing the system to glide along predefined boundaries, offering robustness against parameter fluctuations [126] [127]. However, challenges include vulnerability to "chattering" phenomena, increased design complexity, and the need for sophisticated feedback mechanisms, potentially raising costs and requiring expert knowledge [128][129][130][131].

Fuzzy logic offers an alternative for DC link control by managing complex and nonlinear dynamics using linguistic norms and fuzzy reasoning [132][130][131]. It enhances system responsiveness and robustness against parameter changes, requiring less dependence on precise mathematical models [135][136]. Despite its simplicity and practicality, developing precise control guidelines for fuzzy logic controllers can be challenging and time-consuming, necessitating in-depth system understanding and algorithm refinement [132].

The Proportional Integral (PI) voltage regulator is a straightforward and effective method for maintaining DC-Link capacitor voltage. It offers high accuracy and responsiveness, making real-time adjustments to fluctuations [20], [137]–[139]. The PI regulator allows customization through precise calibration of KP and Ki values, though it relies on trial and error for optimal settings, which can be time-consuming, especially in complex systems with interconnected components [140]–[146]. Despite these challenges, the PI regulator remains an excellent choice for DC-Link voltage control due to its efficiency and precision.

The DC-Link capacitor is crucial in SAPF for maintaining constant voltage and balancing power during transients. To optimize its performance, various control algorithms are employed. Sliding Mode Control (SMC) offers robust performance but faces challenges like "chattering" and complexity. Fuzzy logic manages complex dynamics effectively but requires detailed system understanding for precise control. The Proportional Integral (PI) voltage regulator is simple, accurate, and responsive, though it relies on trial and error for optimal settings. Each method has unique advantages and challenges in maintaining stable DC-Link voltage.

2.8 Optimization Techniques

Optimization refers to the process of finding the best solution or the most efficient use of resources to achieve a specific goal. It involves identifying the optimal set of parameters or variables that will result in obtaining maximum or minimum value objective function. The objective function could be any metric or cost function desired to be optimized in a particular application, such as accuracy, efficiency, or error rate. This process is crucial in fields like scientific research, engineering, and machine learning, where model performance depends on optimization quality.

Numerous optimization methods exist, from brute-force algorithms to sophisticated ones [147]. Brute-force methods like grid and random search are practical for low-dimensional problems but inadequate for high-dimensional ones. Deterministic algorithms, such as Newton's method and gradient descent, work well with specific objective function properties but struggle with complex, non-convex functions [148]. Stochastic algorithms, like genetic algorithms and particle swarm optimization, are better suited for complex, non-convex problems [149].

Genetic Algorithms (GAs) use evolutionary principles to solve optimization problems, mimicking biological evolution with operators like reproduction, crossover, and mutation. GAs aim to find global extremum values of a function, avoiding local traps [149] [150]. The process starts with a population of chromosomes representing decision variables. New chromosomes are produced through crossover and mutation, and the best ones are selected to form a new population. This cycle continues until convergence or a set number of iterations [151]. However, GAs can suffer from premature convergence, computational complexity, parameter sensitivity, lack of transparency, and do not guarantee finding the global optimum [152]–[154].

Particle Swarm Optimization (PSO), inspired by the collective behavior of bird flocks or fish schools, was introduced by Kennedy and Eberhart in 1995 [155]. Developed to mimic birds' synchronized flight patterns and regrouping behavior, PSO was found to have optimization features, leading to its modification for optimization tasks. PSO uses a population of particles that move through the search space to find the optimal solution. Each particle updates its position based on its personal best and the swarm's global best, guided by cognitive and social components [156].

PSO shares three typical phases with other population-based optimization algorithms: initialization, comparison, and improvement, as depicted in Figure 2.10.

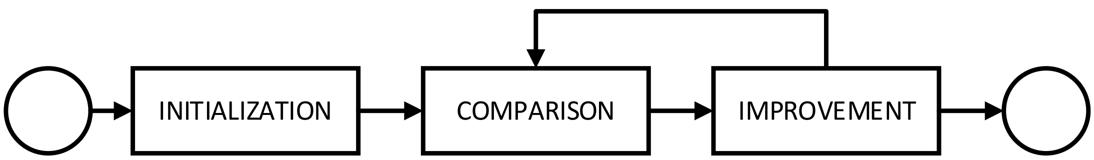

Figure 2.10: Relationship between the three main phases in PSO [155].

In PSO, particles (agents) represent potential solutions, and a swarm is the group of these particles. A larger swarm size can result in better initial variety, especially in a D-dimensional search space, but increases computational time. The number of iterations determines the time for particle movements. The PSO algorithm shows that more agents lead to better initial states and movement processes, though at the cost of increased computation time.

PSO is simple, efficient in high-dimensional spaces, fast in convergence, versatile, robust, and does not require gradient information [155]. Its ease of implementation allows enhancement of output based on simulated data without requiring prior knowledge of the problem.

2.9 Applications of Shunt Active Power Filter

Shunt Active Power Filters (SAPFs) are essential in industrial applications to enhance power quality by addressing harmonics, compensating for reactive power, and balancing loads. In industries with significant non-linear loads, such as those using variable frequency drives and other power electronics, SAPFs mitigate harmonic distortion, ensuring compliance with standards like IEEE 519 and protecting sensitive equipment from damage.

As the emergence of renewable sources like solar and wind often introduce power quality issues due to their intermittent nature, generating harmonics and causing voltage fluctuations. APFs mitigate these issues by filtering out harmonics, reducing voltage variations, stabilizing frequency, and ensuring reliable energy supply. They also provide reactive power compensation, improving the power factor, reducing transmission losses, and enhancing grid stability. Furthermore, APFs balance loads by dynamically adjusting power flow, essential for maintaining a stable distribution of electricity [158]. As shown in Figure 2.11, application of shunt active power system involves the integration DG inverter, voltage and current sensing, and DC Link capacitor. For the system to be working in the system, embedded harmonics extraction algorithm, DC link voltage control algorithm and PWM switching algorithm are placed within the system. The higher the response, the better the SAPF capabilities to work in mitigating the harmonics.

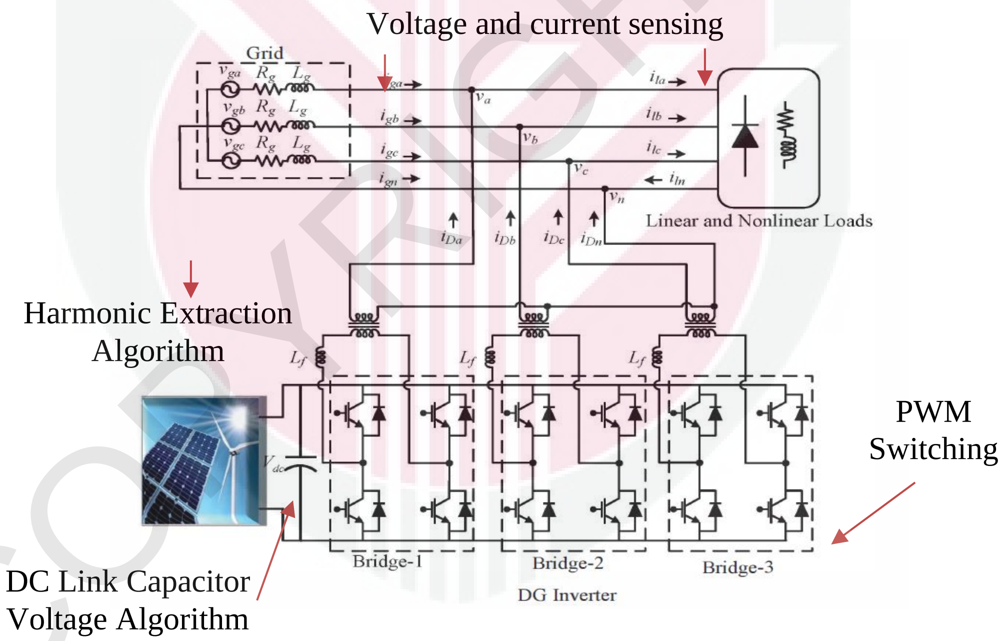

Figure 2.11: Schematic of grid-tied three-phase DG inverter system [157].

Additionally, in manufacturing plants and facilities with large inductive loads, SAPFs provide reactive power compensation, improving power factor, reducing electricity costs, and increasing power system capacity. They also play a crucial role in balancing loads in plants with uneven single-phase loads, reducing neutral currents and preventing equipment overheating. For industries requiring stable voltage, such as semiconductor manufacturing and data centers, SAPFs help to regulate voltage levels, mitigating sags, swells and flicker [159].

2.10 Summary

Power quality issues, particularly current harmonics, have increased due to the rise of nonlinear loads. This has led to a focus on filtering techniques, especially passive and active power filters, with SAPF being favored for its effectiveness in mitigating current harmonics.The current reference generation algorithm, crucial for SAPF, is divided into time and frequency domain algorithms. Among these, the Adaptive Notch Filter (ANF) stands out for its real-time harmonic tracking, resilience to dynamic system conditions, and precise harmonic isolation even under non-stationary conditions. However, ANF lacks features necessary for DC-link control in SAPF, necessitating improvements for efficient harmonic extraction.

DC-link voltage control is also vital, with algorithms like sliding mode control, fuzzy logic, and conventional PI voltage regulators being explored. The PI voltage regulator is preferred for its robust, stable performance and ease of implementation, ensuring precise and responsive voltage regulation. Though tuning PI controllers can be time-consuming and may require periodic adjustments, integrating optimization techniques enhances the controller's ability to maintain DC-link voltage stability.

CHAPTER 3

METHODOLOGY

3.1 Introduction

A shunt active power filter is a type of filter that is used in power systems to mitigate harmonic distortion and thus improve power quality. This chapter discusses the development of a shunt active power filter (SAPF) for three-phase systems in detail. The primary focus of this chapter is on the operational SAPF design. This chapter also includes the development of two key algorithms, the proposed harmonic extraction algorithm and the current control algorithm. The harmonic extraction algorithm identifies and extracts harmonic components from the input signal. Meanwhile, the current control algorithm regulates the current flowing through the SAPF.

In addition to the above, the chapter explores the application of a voltage control algorithm using proportional-integral (PI) control in conjunction with an optimization algorithm. This algorithm aims to maintain a stable output voltage from the SAPF by adjusting the control parameters based on the feedback from the system.

Figure 3.1 depicts the methodology employed in both the simulation and experimental works. The simulation work is divided into steady state and dynamic state operation, with corresponding evaluation criteria provided in the flow chart. The process begins with the mathematical design of the SAPF to obtain component calculations, followed by modeling using MATLAB/Simulink and then developing the algorithm for fundamental signal extraction.

Moving on to the experimental stage, emphasis is given to the design, development, and testing of the hardware setup, including implementing PCB circuits for SAPF and sensors. The fundamental signal extraction and DC-Link voltage control algorithm are executed using a DSpace (RS1104) processor. Experimental work is carried out to validate the simulation results, with testing performed for steady and dynamic state operations.

3.2 Design Consideration

An operational shunt active power filter (SAPF) design involves a combination of hardware and software components. For a SAPF to achieve the optimal performance, factors such as reference selection, DC-link voltages, DC-link capacitors, and filter inductors must carefully be considered. The highlights for the fundamental assumptions underlying the design of SAPF, providing valuable insights into the design process and facilitating the development of efficient and effective SAPF systems are [11]:

1. Shape of instantaneous supply voltages is fully sinusoidal,

2. Distortion of instantaneous supply currents is 5%,

3. Reactive power compensation capability of the SAPF is fixed, and

4. Operation of the SAPF is in the linear modulation mode $0 \leq ma \leq 1$. Note that ma is the modulation factor.

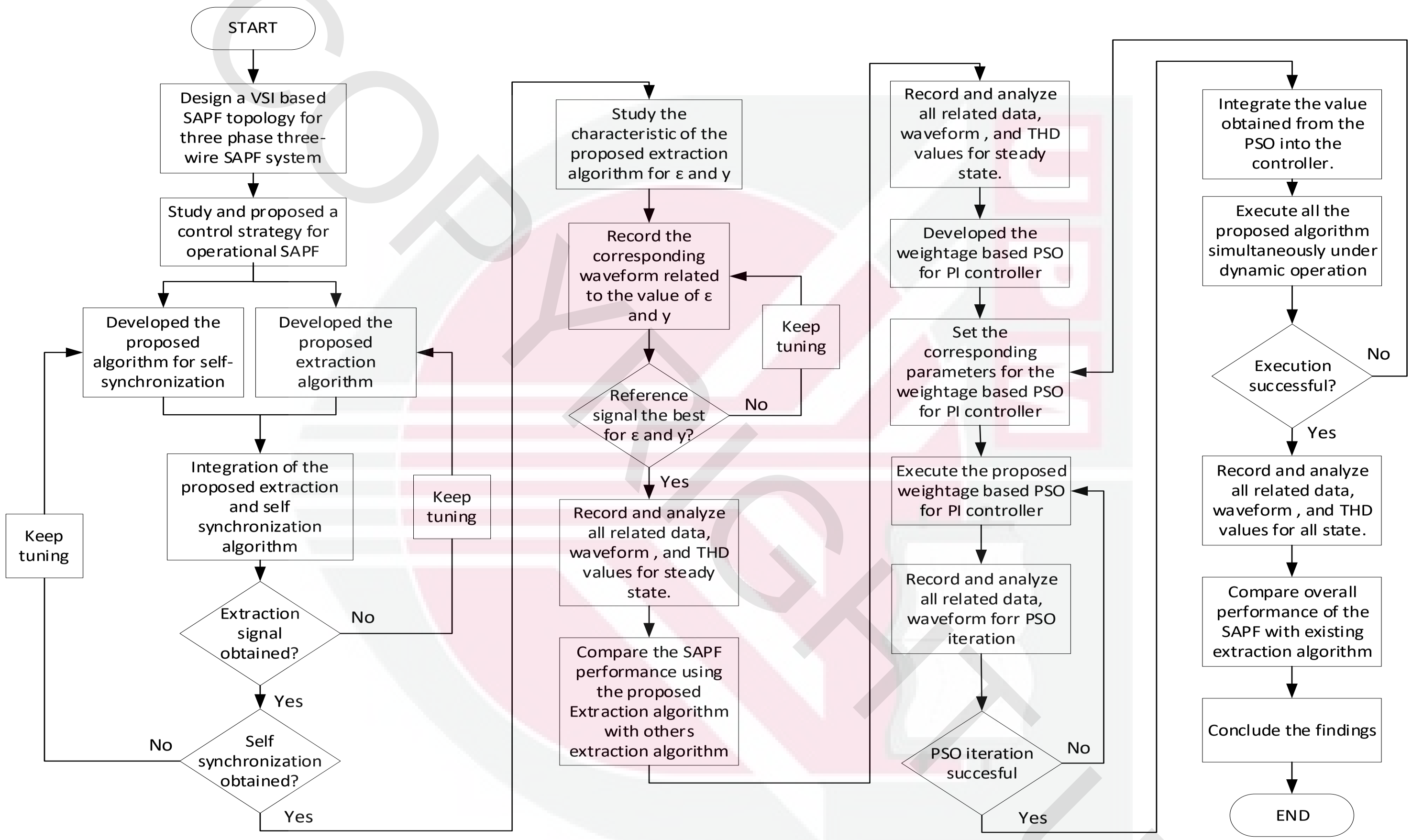

Figure 3.1: Flowchart of the proposed methodology

3.2.1 Implementation of Shunt Active Power Filter

In this proposed SAPF configuration, a conventional arrangement is followed. It consists of three main elements know as three-phase voltage source inverters (VSI), the controller circuit of APF, and a non-linear load. The VSI topology is being used as the configuration for the three-phase three-wire SAPF. The VSI generates corrective output corresponding to the controller circuit, which controls the APF's operation. The non-linear load is considered the source of the current harmonics that contaminate the supply source.

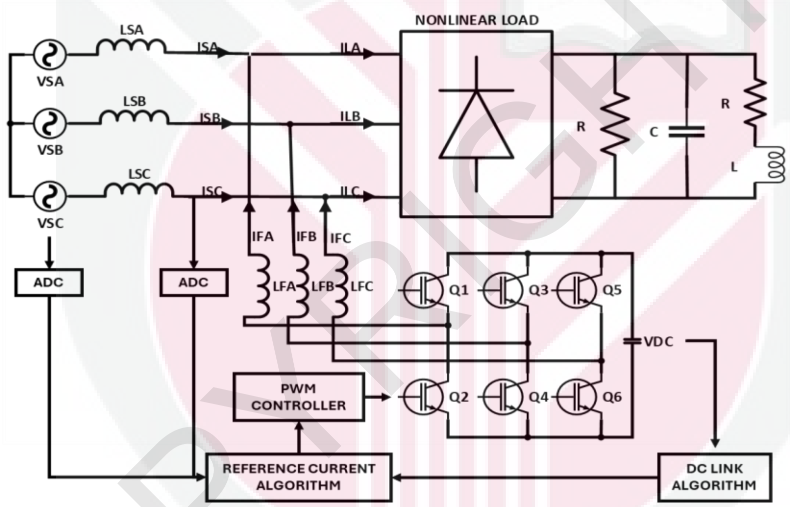

Figure 3.2: Shunt Active Power filter configuration.

The controller circuit is considered as the central processing point of the system, where it utilizes a reference current algorithm to extract the reference signal for the SAPF. The reference signal is then subtracted from the distorted signal to obtain the filtering signal. The filtering signal is then compared and translated by the switching algorithm to generate the gating signal for the VSI. This gating signal enables the VSI to generate the corrective output to mitigate the harmonics introduced by the non-linear load. This algorithm minimizes the current harmonics in the load current by maintaining the current waveform shape similar to the sinusoidal waveform.

Overall, the proposed SAPF configuration with VSI topology, reference current algorithm, and switching algorithm effectively mitigate the harmonics generated by non-linear loads in power systems.

3.2.1.1 Configuration of Nonlinear Loads

As discussed in the previous chapter, current harmonics occurred in the electrical power grid system is due to the contribution of the nonlinear loads. Within this research work, the generation of current harmonics is contributed from the arrangement of a three-phase rectifier that is related to the three types of predetermined loads: pure resistive, inductive, and capacitive. The basic configuration of those loads is shown in Figure 3.2. The inductive load combines the inductor and resistor in series, while the capacitive load is a combination of capacitor and resistor in parallel connection.

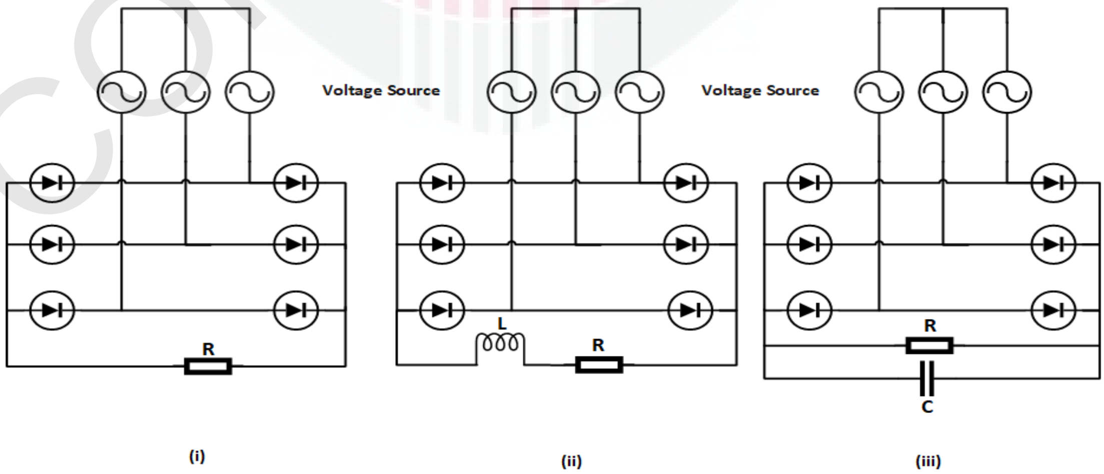

Figure 3.3: Nonlinear loads (i) pure resistive (ii) inductive loads and (iii) capacitive loads

Depending on the load configuration, various waveform distortions can occur in the load and source current that contributes to the harmonics. Based on this, a multiple configuration of loads is applied during the steady state and transient state to create effects of various waveforms during the operation of SAPF.

3.2.1.2 Selection of Reference DC-link Voltages

One of the main criteria in developing the SAPF is the balanced energy schemes between the SAPF and the supply system. The supply of SAPF is determined by the DC-link reference value, where it follows the concept of reactive power compensation. For the DC-Link voltage (V_{DC}) to work satisfactorily, it should be in higher magnitude when compared to the source voltage V_S.

Figure 3.3 shows a single-phase circuit diagram and a single-line diagram of SAPF operation. Regarding the single-line diagram, SAPF will regulate the instantaneous fundamental current $I_F(t)$ following the principle of compensation of balanced reactive power to compensate reactive power of the nonlinear load.

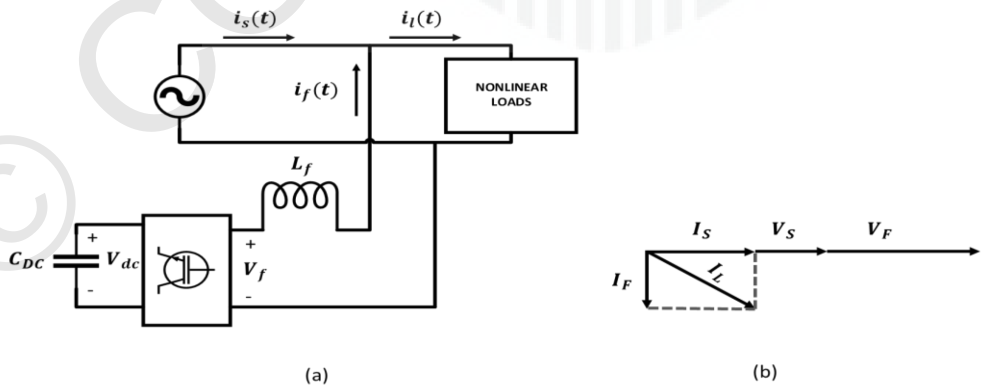

Figure 3.4: (a) Per-phase circuit and (b) single-line diagram of the SAPF (for reactive power compensation) [160].

As the source current $I_S(t)$ is in phase with V_S, then for an optimized result, the phase of $I_F(t)$ must be orthogonally in line with V_S. Based on this condition, the filter voltage V_F across the SAPF can be defined as [160]:

$$V_F = V_S + j\omega L_F I_F \tag{3.1}$$

Based on the configuration of this single line diagram, the three-phase reactive power (QF) that the SAPF produces can be expanded as:

$$\mathrm{QF} = 3\mathrm{V}_S\mathrm{I}_S \ = \ 3\mathrm{V}_S\left(\frac{V_F}{\omega L_F}\right)\left(1 - \frac{V_S}{V_F}\right) \tag{3.2}$$

where I_S is the peak amplitude for instantaneous fundamental supply current, V_F is the peak amplitude of the instantaneous fundamental SAPF voltage, ω is the angular frequency of operating power systems, and L_F is the filter inductor. In this condition, the upper limit of the V_F is determined based maximum capacity of the SAPF as given in following calculation [161].

$$\frac{dQ_F}{dV_S} = 0; \qquad \frac{d}{dV_S}\left(\frac{3\mathrm{V}_S V_F}{\omega L_F} - \frac{3{\mathrm{V}_S}^2}{\omega L_F}\right) = 0; \qquad V_F = 2\mathrm{V}_S \tag{3.3}$$

According to the above equation and the statement that the DC-Link should be higher than V_S, the operative range of V_F can be stated as:

$$0 < V_F < 2\mathrm{V}_S \tag{3.4}$$

With the PWM converter is assumed to operate in linear modulation mode, then [162]:

$$m_a = \frac{2\sqrt{2}V_F}{V_{DC}}, \quad for\ m_a = 1,\ V_{DC} = 2\sqrt{2}V_F \tag{3.5}$$

Throughout this work, selection of the DC-Link reference refers to equations 3.4 and 3.5.

3.2.1.3 Design of DC-link Capacitors

In the operation of the SAPF, DC-Link capacitors function as energy storage. Its main operation is to supply reactive power required for mitigation purposes and to constantly maintain the DC voltages. In estimating the value for the DC-Link capacitor, the principle of energy conversion is applied. The design of DC-Link capacitor depends on the instantaneous power flow during the changing load state. The principle of the DC-Link capacitor can be defined as [162]:

$$\frac{1}{2}C_d[V_{DC}^2 - V_{DCa}^2] = 3V_p\alpha I T_s \qquad (3.6)$$

where V_{DC} is the base of DC bus voltage, V_{DCa} is the minimum of DC bus voltage level, α is the overloading factor, V_p is the phase voltage, I is the phase current and T_s is the time constant for the DC bus voltage to retain its value.

3.2.1.4 Design of Filter Inductors

Filter inductors are one of the essential design criteria to be considered in developing the SAPF. The filters are utilized to reduce the ripple of compensation currents; that is due to the switching activity of SAPF [33]. They are designed according to the principle of harmonic current reduction [11, 33]. In the linear modulation mode, the ripple current I_{Fh} can be represented using the maximum harmonic voltage V_{Fh}, which occurs at the frequency $m_a\omega$. It can be written as

$$I_{Fh}(m_\alpha \omega) = \frac{V_{Fh}(m_\alpha \omega)}{m_\alpha \omega L_F} \tag{3.7}$$

Eventually, the rating value of LF can be determined by solving (3.1) and (3.7) simultaneously.

3.3 Proposed Algorithms

The proposed algorithm for the system is as follows.

3.3.1 Extended Fryze Adaptive Notch Filter

The concept of an adaptive notch filter (ANF) is based on the idea that for a specified frequency, the frequency gain will be in zero condition, while for other circumstances of frequencies, a linear gain is applied to them [163]. Ideally, the ANF works through this unique characteristic which is based on a linear gain applied for all the frequencies except for a specified frequency where its gain is zero. Based on this characteristic, the filter can withdraw an implicit signal of a sinusoidal waveform from the measured component of the electrical power system of the specified frequency. ANF has been well-researched in removing noises within the sinusoidal waveform [11].

Originally, ANF is based on an IIR filter [16]; however, with the improvement in the notch frequency, the filter can adapt to notch frequency that change with time by tracking the input signal frequency variation. This tracking characteristic eliminates the need for a consistent signal frequency, as usually required for the typical notch filter to work efficiently. The dynamic operation for the ANF can be referred to the following set of differential equations. [164] The block design of the ANF is shown in Figure 3.5.

$$\ddot{x} + \theta^2 x = 2\varepsilon\theta e(t) \quad (3.8)$$

$$\dot{\theta} = -yx\theta e(t) \quad (3.9)$$

$$e(t) = u(t) - \dot{x} \quad (3.10)$$

Based on the given differential equation above, the ANF consists of the following elements. Firstly, the input signal of the ANF is represented by u(t). The frequency estimation of the ANF system is given by θ. Meanwhile, the accuracy and convergence speed are determined by two coefficients within the ANF known as y and ε [121], [165], [166]. However, the two coefficients must compensate each other for the ANF to work effectively and most efficiently. Lastly the $\dot{\theta}$ represents the updated law for frequency estimation [13]. For the selection of two variable coefficients of the ANF is done by using PSO method.

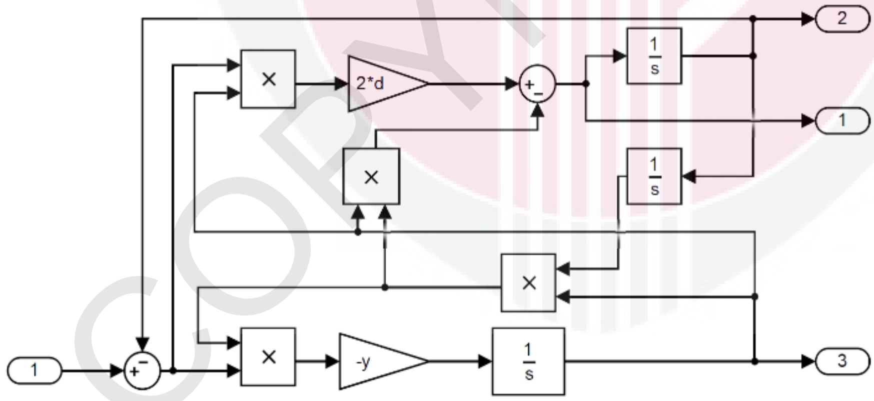

Figure 3.5: ANF structure for a single system [16].

For functional single sinusoidal input u(t) = A_1 sin (ω_0t + φ_1), the mentioned ANF has a unique characteristic where it has a unique periodic orbit at O as shown in equation 3.11 [167]. After the implementation of a single ANF system, three functional outputs are produced from the ANF, namely the filtered cos signal denoted by $\overline{x}$ but in negative magnitude, the filtered sin signal denoted by $\dot{\overline{x}}$ which is identical to the input signal and, finally $\overline{\theta}$ which represents the frequency of the signal [168].

$$O = \begin{pmatrix} \bar{x} \\ \dot{\bar{x}} \\ \bar{\theta} \end{pmatrix} = \begin{pmatrix} -A_1 \cos(\omega_0 t + \ \varphi_1)/\omega_0 \\ A_1 \sin \omega_0 \ (\omega_0 t + \ \varphi_1 \ ) \\ \omega_0 \end{pmatrix} \tag{3.11}$$

As the ANF function is expanded for application within a three-phase power system of SAPF, the measurement of the waveform will involve three-phase waveforms of voltage and current for supply and load. Based on this consideration, the three-phase sinusoidal voltage or current will be represented based on equation 3.12.

$$u(t) = \begin{pmatrix} u_a(t) \\ u_b(t) \\ u_c(t) \end{pmatrix} = \begin{pmatrix} A_a \sin(wt + \emptyset_{a)} \\ A_b \sin(wt + \emptyset_{b)} \\ A_c \sin(wt + \emptyset_{c)} \end{pmatrix} \tag{3.12}$$

In the context of three phase application, the ANF can be enhanced to track frequency more effectively because it operates within the same electrical power system and shares the common frequency that is represented by ω_0 as in equation 3.12 [169]. Corresponding to three phase operation, the frequency law for all the three phase ANF can be shared, simplifying the ANF complexity by reducing the integration function order from the 9 to the 7. The ANF will work in parallel order in extracting the fundamental components by sharing the common frequency over time [170]. The improved fundamental equation for the three-phase system ANF can be nominated in equations 3.13 to 3.15, where the phase is represented as n for phases a, b, and c.

Meanwhile, the updated law of frequency is based on the summation of the error signal of all three phases.

$$\ddot{x}_n + \theta^2 x_n = 2\varepsilon\theta e_n(t) \tag{3.13}$$

$$\dot{\theta} = -y\theta \sum x_n \, e_n(t) \tag{3.14}$$

$$e_n(t) = u_n(t) - \dot{x}_n \tag{3.15}$$

Expanding the equation to the respective phase yields the ANF phase error equation in equation 3.16. The error for each phase is then inserted into equation 3.14, resulting in the ANF phase update law given in equation 3.17.

$$e_n(t) = \begin{pmatrix} e_a(t) \\ e_b(t) \\ e_c(t) \end{pmatrix} = \begin{pmatrix} u_a(t) - \dot{x}_a \\ u_b(t) - \dot{x}_b \\ u_c(t) - \dot{x}_c \end{pmatrix} \tag{3.16}$$

$$\dot{\theta} = -y\theta \sum x_n \, e_n(t) = -y\theta\big(x_a e_a(t) + x_b e_b(t) + x_c e_c(t)\big)$$

$$= -y\theta(x_a(u_a(t) - \dot{x}_a) + x_b(u_b(t) - \dot{x}_b) + x_b(u_c(t) - \dot{x}_c))$$

$$= -y(\theta x_a(u_a(t) - \dot{x}_a) + \theta x_b(u_b(t) - \dot{x}_b) + \theta x_b(u_c(t) - \dot{x}_c)) \tag{3.17}$$

Based on the update law in equation 3.17, the ANF for each phase is given as equation 3.18, where θ is obtained from the integration of $\dot{\theta}$ and x which is obtained from the double integration of $\ddot{x}$ [171].

$$\begin{pmatrix} ANF_a \\ ANF_b \\ ANF_c \end{pmatrix} = \begin{pmatrix} \ddot{x}_a + \theta^2 x_a = 2\varepsilon\theta e_a(t) \\ \ddot{x}_b + \theta^2 x_b = 2\varepsilon\theta e_b(t) \\ \ddot{x}_c + \theta^2 x_c = 2\varepsilon\theta e_c(t) \end{pmatrix} \tag{3.18}$$

The detailed implementation of the multi-block for the three-phase ANF is shown in Figure 3.6, which contains the arrangement of error multiblock, update law multiblock, and ANF substructure multiblock for a complete three-phase ANF. As shown in the block, the ANF shares the same frequency law [172].

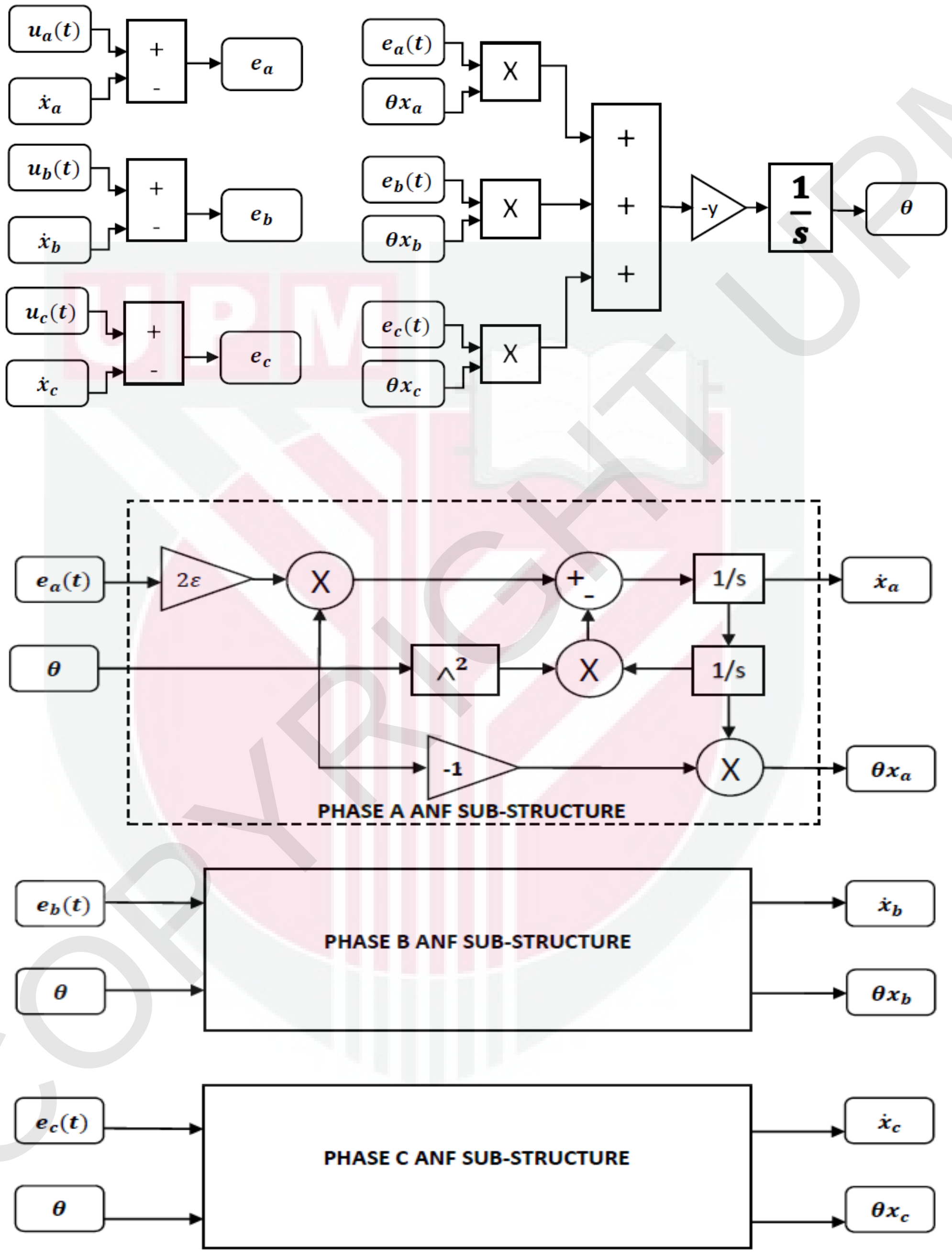

Figure 3.6: Error multiblock, update law multiblock, and sub-structure multiblock for three-phase ANF [172].

When using an adaptive notch filter (ANF), it is crucial to recognize and manage potential drawbacks, such as phase shift and gain variations, which can affect the signal quality. The phase shift introduced by the ANF can distort signal components' temporal relationships, impacting accuracy in signal analysis, especially critical in communication and audio systems. Moreover, gain variations from the ANF can distort signal amplitudes, crucial in maintaining fidelity in audio and sensor data analysis.

The Adaptive Notch Filter (ANF) addresses the drawbacks of traditional notch filters by dynamically adjusting its notch frequency to match the input signal, effectively suppressing specific frequencies while minimizing phase shift and gain variations. Key features include adaptive notch frequency, continuous frequency tracking, dynamic parameter adjustment, stability analysis for maintaining stability, and noise immunity to reduce external influences. The ANF's adaptability and its focus on signal tracking enable it to overcome traditional filter limitations, ensuring improved signal quality in signal processing applications.

3.3.1.1 Reference Current Estimation

In a three-phase power system, the power flow usually consists of absolute, reactive, and harmonics powers. Thus, the power term containing all the efficient and non-efficient powers terms in the three-phase system is defined as equation 3.19 [173].

$$S_e^2 = (3V_{e1}I_{e1})^2 + (3V_{e1}I_{eH})^2 + (3V_{eH}I_{e1})^2 + (3V_{eH}I_{eH})^2 \quad (3.19)$$

where $(3V_{e1}I_{e1})^2$ refers to the fundamental effective apparent power and $(3V_{e1}I_{eH})^2 + (3V_{eH}I_{e1})^2 + (3V_{eH}I_{eH})^2$ refers to nonfundamental effective apparent power. By applying ANF for the measured voltage and current, their fundamental components can be extracted, and the fundamental power for the system can be obtained based on the extracted components. Centered on this, the estimation of the reference supply current will be produced. However, to ensure the successful task of SAPF, the DC-Link voltage needs to be controlled to ensure that it is maintained at the reference value. As the DC-Link of a SAPF acquires its power from the line and is accustomed to losses due to switches and active power transfer, the DC-Link voltage is exposed to various disturbances, which could lead to voltage instability. To be overwhelmed with this condition, DC-Link control is crucial to the SAPF. This system determines and compares the DC-Link reference with the sensed DC-Link voltage. The error between the reference (v_{dcref}) and measured DC-Link voltage ($v_{dcsense}$) is passed into the proportional-integral (PI) controller (P_{dc}). The loss is then integrated into the instantaneous power equation, as in equation 3.20.

$$\overline{p}_{3\phi} = v_a i_a + v_b i_b + v_c i_c + P_{dc} \tag{3.20}$$

The error or difference ($e_{vdc}(t)$) is obtained from the DC-Link voltage measurement is shown in equation 3.21, and the PI controller is applied towards the error to obtain the value as power losses of the DC-Link shown in equation 3.22 [174].

$$e_{vdc}(t) = v_{dcref} - v_{dcsense} \tag{3.21}$$

$$P_{dc} = P_{dc}(t-1) + K_p\big(e_{vdc}(t) - e_{vdc}(n-1)\big) + K_i e_{vdc}(t) \tag{3.22}$$

Meanwhile, the three-phase reference supply is obtained through the Fryze equation [97], [99], [175], [176], where this method determines the reference current based on the average value of the 3-phase instantaneous power. The equivalent conductivity calculates the average current, while the average admittance (G_e) is determined based on the concept of aggregate voltage as follows [130]:

$$G_e = \frac{\overline{p}_{3\phi}}{V_\Sigma^2}, \tag{3.23}$$

where $V_\Sigma^2 = sum\ of\ voltage = \sqrt{v_a^2 + v_b^2 + v_c^2}$,

When the equation is expanded, the reference current can be given as,

$$i_{\overline{ref}k} = G_e v_k\ ,\ k = (a, b, c\ ) \tag{3.24}$$

$$i_{\overline{ref}k} = \begin{bmatrix} i_{\overline{ref}a} \\ i_{\overline{ref}b} \\ i_{\overline{ref}c} \end{bmatrix} = \begin{bmatrix} \frac{(v_a i_a + v_b i_b + v_c i_c + P_{dc}) \times v_a}{\sqrt{v_a{}^2 + v_b{}^2 + v_c{}^2}} \\ \frac{(v_a i_a + v_b i_b + v_c i_c + P_{dc}) \times v_b}{\sqrt{v_a{}^2 + v_b{}^2 + v_c{}^2}} \\ \frac{(v_a i_a + v_b i_b + v_c i_c + P_{dc}) \times v_c}{\sqrt{v_a{}^2 + v_b{}^2 + v_c{}^2}} \end{bmatrix} \tag{3.25}$$

On this basis, the ANF with Fryze power control can produce the individual reference, ($i_{\overline{ref}k}$) current for each phase sequence obtained from equation 3.25, as mentioned.

3.3.2 Particle Swarm Optimization Algorithm

Particle Swarm Optimization (PSO) is an algorithm that simulates the social behavior of swarming animals to solve optimization problems. Each particle, representing a potential solution, starts with random positions and velocities in a D-dimensional search space. Particles evaluate their positions using a fitness function, tracking their personal best and the swarm's global best positions. In each iteration, particle velocities are updated based on their current velocity, personal best, and global best, with random factors for exploration. Positions are then updated accordingly. This process repeats until convergence or a set number of iterations, with the global best position considered the optimal solution. PSO efficiently balances exploration and exploitation for complex problem optimization.

The algorithmic expression for PSO can be described mathematically using equations (3.26) to (3.31). Equation (3.26) denotes that the initial value of the *i*th particle, which consists of d optimization parameters or variables. The search space for the particle, $\boldsymbol{x}_i(0)$, represented in equation (3.27), is uniformly distributed between the minimum and maximum values. Initial optimization process and potential solutions are generated randomly in the first step using equation (3.28), as mentioned in step 01 of Table 3.1 [155].

$$\boldsymbol{x}_i(0) = [e_1, e_2, \dots, e_d]^T \tag{3.26}$$

$$\boldsymbol{x}_i(0) \sim U(\boldsymbol{x}_{min}, \boldsymbol{x}_{max}) \tag{3.27}$$

$$\boldsymbol{x}_i(0) \sim R(\boldsymbol{x}_{min}, \boldsymbol{x}_{max}) \tag{3.28}$$

To evaluate the optimization problem, a fitness function, also known as an objective function, is required. The fitness function will be represented as $f(\boldsymbol{x}_i)$. The second phase of execution involves comparing each agent in the swarm intelligence (SI) to other agents in the group. Each iteration involves two comparisons, first the fitness of each particle is compared to its own personal best record ($\boldsymbol{pbest}$) and second the fitness of the swarm ($\boldsymbol{gbest}$). Equations (3.29) and (3.30) show how each particle compares its performance with its own best record and the swarm best record [177], [178].

$$\boldsymbol{pbest}_i = \begin{cases} \boldsymbol{pbest}_i(t-1), & f(\boldsymbol{x}_i(t)) \leq f(\boldsymbol{pbest}_i(t-1)) \\ \boldsymbol{x}_i(t), & f(\boldsymbol{x}_i(t)) > f(\boldsymbol{pbest}_i(t-1)) \end{cases} \quad (3.29)$$

$$\boldsymbol{gbest} = \begin{cases} \boldsymbol{gbest}(t-1), & f(\boldsymbol{x}_i(t)) \leq f(\boldsymbol{gbest}(t-1)) \\ \boldsymbol{x}_i(t), & f(\boldsymbol{x}_i(t)) > f(\boldsymbol{gbest}(t-1)) \end{cases} \quad (3.30)$$

In the final phase of the algorithm, the objective is to enhance the solutions by moving the agents. The process is achieved by relocating agents with low fitness values towards those with higher fitness values. In the case of PSO, particles move towards the current best particle in the swarm ($\boldsymbol{gbest}$) and its personal best record ($\boldsymbol{pbest}$), which is represented by equations (3.30) and (3.31) [21].

$$\boldsymbol{v}_i(t+1) = \omega \times \boldsymbol{v}_i(t) + c_1 \times r_1 \times [\boldsymbol{pbest}_i(t) - \boldsymbol{x}_i(t)] + c_2 \times r_2 \times [\boldsymbol{gbest}(t) - \boldsymbol{x}_i(t)] \quad (3.31)$$

In PSO, the velocity of the ith particle at iteration is determined by three components: history, cognitive, and social. The history component $\omega \times \boldsymbol{v}_i(t)$, acts as momentum, with the inertia coefficient, ω controlling the reliance on previous velocity where smaller value favors exploration over exploitation. The cognitive component $c_1 \times r_1 \times [\boldsymbol{pbest}_i(t) - \boldsymbol{x}_i(t)]$, drives the particle to replicate its past success, where c_1 is the cognitive coefficient and r_1 introduces randomness. The social component $c_2 \times r_2 \times [\boldsymbol{gbest}(t) - \boldsymbol{x}_i(t)]$, rives the particle to follow the swarm's best solution, where c_2 is the social coefficient and r_2 adds randomness. These components combine to update the velocity $\boldsymbol{v}_i(t+1)$, leading to a new particle position in the search space, as described in equation 3.32 [179].

$$\boldsymbol{x}_i(t+1) = \boldsymbol{x}_i(t) + \boldsymbol{v}_i(t+1) \quad (3.32)$$

For fine-tuning PI parameters in the SAPF, weightage-based particle swarm optimization (WBPSO) is proposed. The basic equation for the WBPSO is as in equation 3.33, in this equation for single output multiple input configuration, the error of the WBPSO is based on the THD final value and the DC-Link voltage absolute error. The criteria are being added with weightage for each input configuration based on its priority, where w_1 and w_2 values are ranged between 0 to 1. A normalization criterion N_1 and N_2 are also added to ensure that the priority of each selected input is appropriately designated. Where for this configuration the normalization value of N_1 and N_2 are selected as 0.5.

To ensure that the PSO works in optimal operation, constraints involved in the control parameters of PSO need to be defined. The swarm size affects the convergence rate and the algorithm's ability in premature or over convergence. The inertia weight ω is another critical parameter, balancing exploration, and exploitation, with a high inertia weight favoring global search and a low weight favoring local search. Additionally, the cognitive c_1 and social c_2 coefficients influence the particles' movements towards their own best-known positions and the swarm's best-known positions, respectively. Proper tuning of these coefficients is essential to avoid local minima and ensure convergence. Another control constraint that needs to be taken into consideration when applying the PSO is the upper and lower limit of each agent need to be determined to ensure that the optimization iteration process will be sufficient. In the simulation the upper limit and lower limit of the Kp and Ki is set to 0 and 100.

$$Error = w_1\, x\, (FVTHD_1(t))N_1 + w_2\, x\, (FEDC_2(t))N_2 \quad (3.33)$$

To improve the WBPSO in terms of overshoot and steady-state error (SSE), the sum of means square error criteria in the equation is added, as shown in equation 3.34.

$$SSE = \sum_{k=1}^{N} w_1 \, x \, (FVTHD_1(t))N_1 + \sum_{k=1}^{N} w_2 \, x \, (FEDC_2(t))N_2 \quad (3.34)$$

In the final equation, steady state error, also known as SSE, and overshoot, also known as OS, are given lower emphasis than settling time (Ts), in which the PBEST and GBEST are updated following the priorities DC-link voltage error and THD value.

3.3.3 Linear Proportional-integral Controller Optimization

To optimize the PI controller for the application of the SAPF, the controller is tuned up using the WBPSO. The values of lower and upper limit of Kp and Ki for the controller are initially set for the purpose of iteration values. The values of particles, iteration and fitness function are set. For the offline simulation set up, the values that being implemented are particles equal to 6, dimensions equal to 2 and fitness function is 5. The values of the suggested Kp and Ki will be implemented in the controller and will be run for each of the particle's values. For every iteration done, the value of error towards the DC link will be recorded and compared based on the result for the best value.

Two suggested methods that are being used to tune the PI controller based on the WBPSO which are FE and SSE. In the FE, the final error is determined by the last values of DC link error and the THD value, while for the SSE method is determined by the sum square error value of the DC link voltage and the THD final values.

3.4 Simulation Work

In this work, MATLAB/ Simulink is used for modeling, simulating, and analyzing the proposed power system, SAPF, EFANF, and WBPSO-optimized PI controller. MATLAB/ Simulink was chosen since it supports automatic code generation and continuous testing and verification of the embedded system. Figures 3.7 and Figure 3.8 show the simulation model of all the proposed circuits and algorithms. The simulation consists of:

(a) Three-phase power source connected to nonlinear loads.

(b) SAPF with DC-Link. The equations of DC-Link for optimization are covered by equations 3.33 and 3.34.

(c) EFANF algorithm block. This block is manifestation of equations 3.8 to 3.25.

Detailed simulation models are shown in Appendix A. For the specification of source voltage and load variables that are used in the experiment is given in table 3-2.

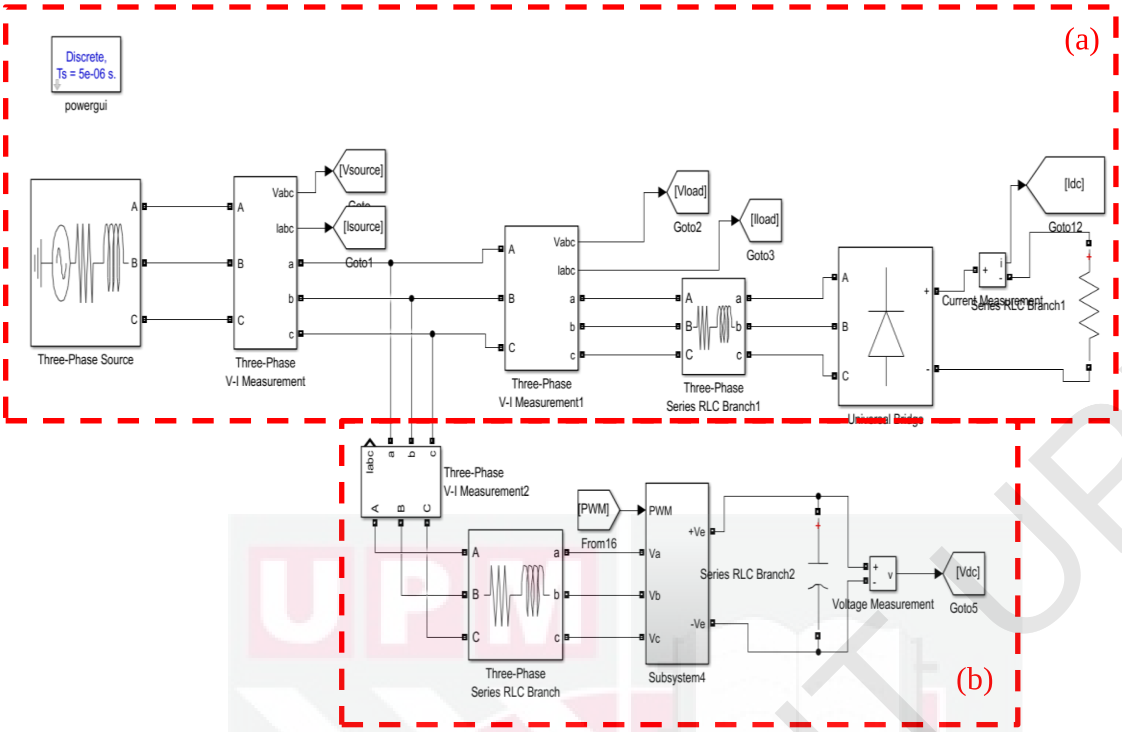

Figure 3.7: Simulation work of electrical power system.

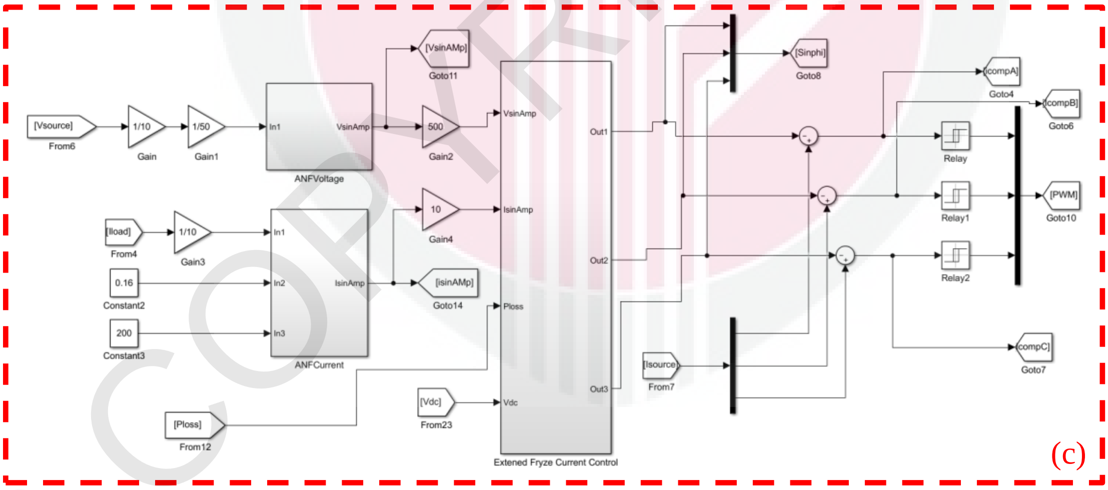

Figure 3.8: Simulation work of EFANF

Table 3.1: Specifications adopted in simulation and experimental works.

Description	Values
Three-phase supply voltage	415 V (Exp:100 V)
Line inductor L_s and filter inductor L_f	1 mH and 5mH
DC-link capacitor C_{dc} and voltage $V_{dc\ ref}$	4700 uF and 700 V (Exp: 200 V)
Power Bridge Rectifiers SKD62 (nonlinear load)	V_{RSM} = 800V, I_D = 60 A
Resistive load	R_1 = 80 Ω R_2 = 50 Ω R_3 = 32 Ω
Inductive load (inductor and resistive in series)	R_1L_1 = 77 Ω and 77 mH R_2L_2 = 53 Ω and 53 mH R_3L_3 = 32 Ω and 32 mH
Capacitive load (capacitor and resistor in parallel)	R_1C_1 = 50 Ω and 12 μF R_2C_2 = 50 Ω and 17 μF R_3C_3 = 50 Ω and 36 μF

3.5 Experimental Work

The laboratory hardware setup was later developed to validate simulation results of the proposed algorithm. The hardware consisted of measurement circuits with current and voltage sensors, a three-phase inverter connected to the filtering inductor as SAPF, and DSpace RS1104 as the controller. For the SAPF, a configuration of three-phase VSI with DC-link. The prominent role of the DSpace is to implement the harmonics extraction algorithm, which will generate the reference current based on the EFANF. For the experiment, the supplied voltage of the system is set at 50Hz, 100 Vrms (line-to-line voltage).

In Figure 3.9, a comprehensive view of the experimental setup is presented. This figure represents the various components involved in the experimental setup, including the measurement circuits, three-phase inverter, and DSpace RS1104 controller. This figure also depicts the connection between these components, which help to establish the overall system architecture. Figure 3.10 outlines the input and output (IO) settings for the DSpace unit. It shows how DSpace IO board connection types, and the connection with DSpace. The figures also show the capacitor that being used by DC-Link for the VSI and three inductors used as the filtering inductor for each phase.

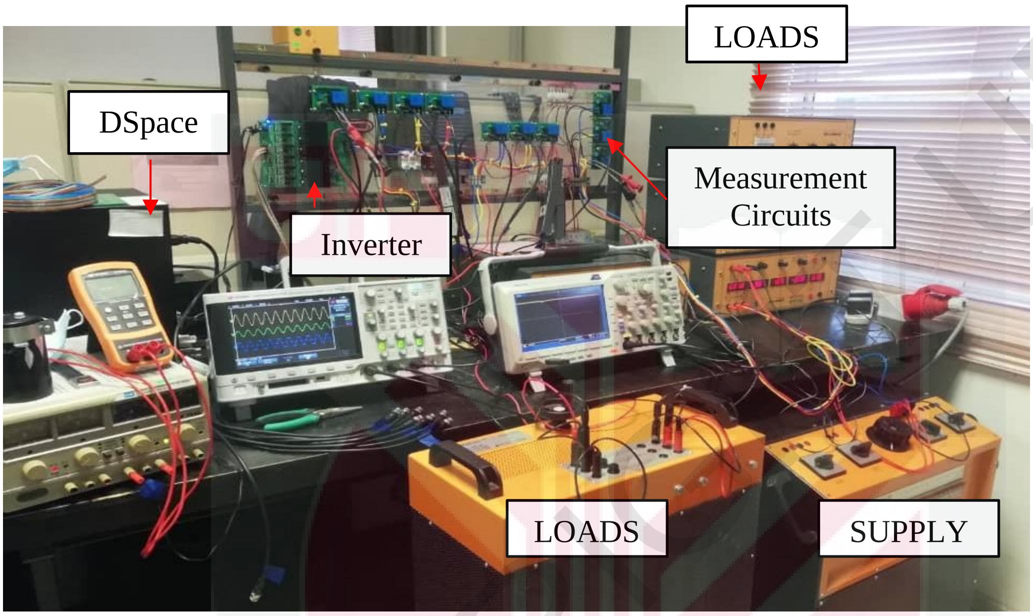

Figure 3.9: Comprehensive view of the experimental setup.

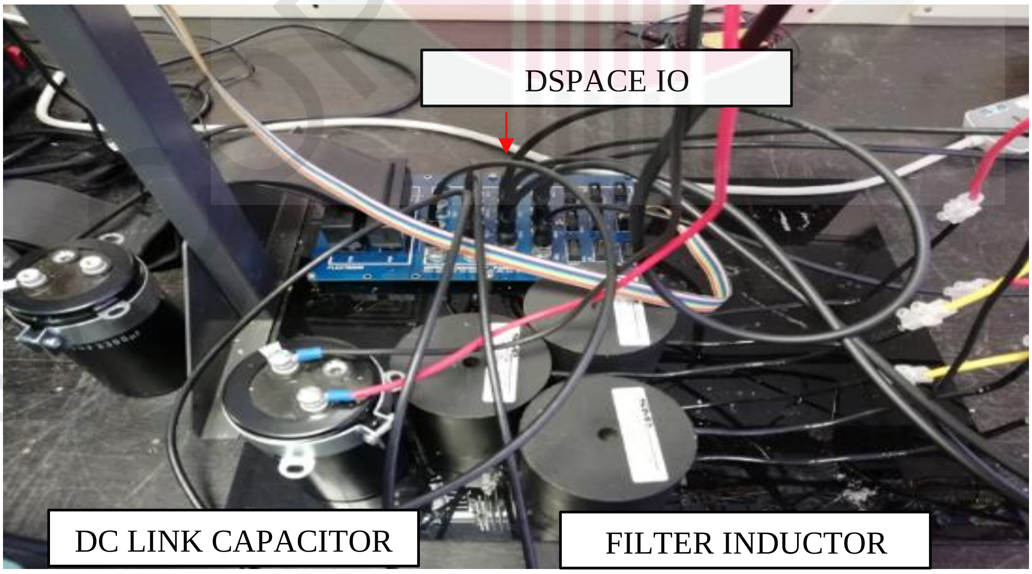

Figure 3.10: DSpace IO unit and filter inductor

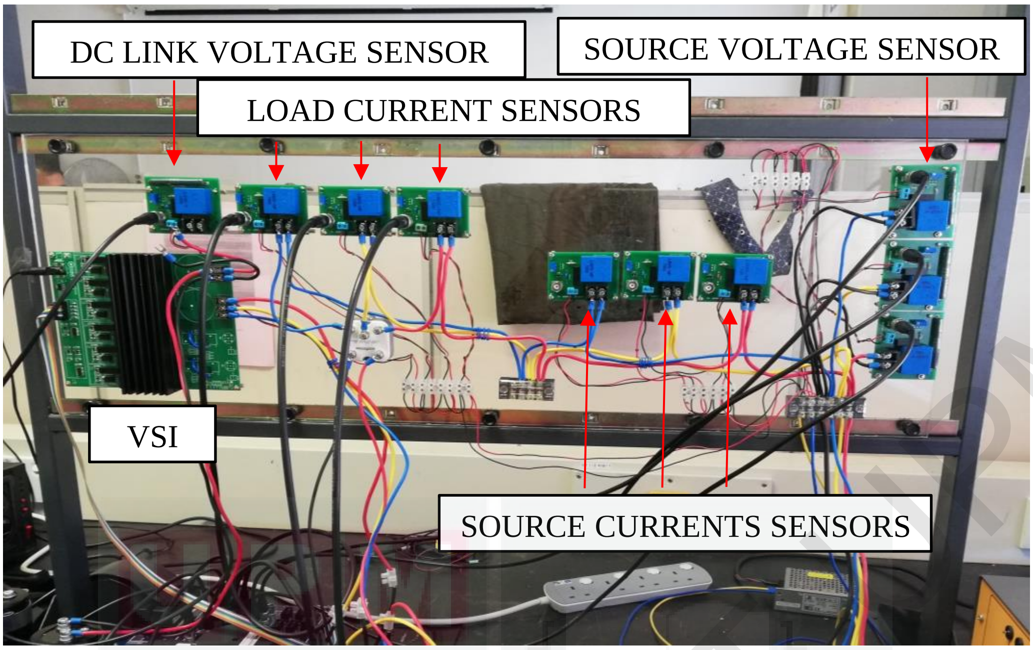

Figure 3.11: Voltage sensor, current sensor, and VSI

Figure 3.11 provides a detailed view of the sensor configuration used in the experimental setup. It shows the arrangement of the sensors, which are directly connected to the DSpace IO. The three-phase voltage sensor measures the voltage across each phase, while the three-phase source current sensor measures the current flowing from the power supply to the inverter. The three-phase load current sensor measures the current flowing from the inverter to the load, and the DC-Link voltage sensor measures the voltage across the DC-Link capacitor. All these measurements are feedback to DSpace for processing proposed algorithms and switching.

All experimental data is captured using the oscilloscope. However, in terms of detailed analysis of the THD, it is being done by assistance of Matlab Simulink to obtain more precise data on the order of harmonics and also due to the limitation of the oscilloscope

3.6 Summary

The development of both SAPF and proposed algorithms has particularly been elaborated. Furthermore, the proposed algorithms' function, principal operation, and characteristics are explained in this chapter. In this work, the function of the proposed algorithm is expanded using a combination of two Adaptive Notch Filter and Fryze algorithms for reference current generation algorithm and DC-Link power control algorithm. The proposed EFANF has a self-tracking characteristic, so the proposed extraction algorithm can work as a reference current synchronizer. Other than that, it is predicted that the performance of the SAPF using ANF and Fryze voltage control algorithms is better than conventional voltage control algorithms. Throughout the implementation of the WBPSO, the Kp and Ki values are also tuned for the best weightage of DC-Link voltage control and THD mitigation. Also, by applying WBPSO, the application of PI is simpler to be implemented and does not put extra burden the microprocessor operation, such as fuzzy and other DC-Link voltage controls.

CHAPTER 4

RESULTS AND FINDINGS

4.1 Introduction

This chapter presents the results and findings by focusing on two principal algorithms as described in the methodology section. The first discussion involves the harmonics extraction algorithm, the extended Fryze adaptive notch filter (EFANF). A comprehensive analysis of the EFANF algorithm's performance is provided through detailed simulations and experimental scenarios. The chapter includes steady-state simulation results and experimental verifications, demonstrating the algorithm's effectiveness in harmonics extraction. Additionally, transient-state simulations and experimental validations corroborate these findings. The chapter also explores the characteristics of EFANF self-synchronization and its efficacy in synchronizing multiple ANF units. The individual and integrated algorithm performance is validated experimentally, confirming its practical applicability. The performance of the shunt active power filter (SAPF) using the EFANF is compared with that of the PQANF, assessing the total harmonic distortion (THD) value and response time.

The second major focus of the chapter is on DC-link voltage control using weightage-based particle swarm optimization (WBPSO). The chapter presents simulation results optimizing the PI controller with WBPSO, which are validated through experimental comparisons, demonstrating the algorithm's effectiveness. All results and findings are aligned with the objectives stated in Chapter 1 and adhere to the methodology outlined in Figure 3.1.

4.2 Harmonics Extraction Algorithm

The main criterion of the algorithm implemented in the SAPF is the harmonics extraction algorithm. The primary function of this algorithm is to extract the harmonics and produce the reference current to be applied by the SAPF to mitigate the harmonics.

The suggested extraction algorithm is simulated on the proposed parameters mentioned in Chapter 3.

4.2.1 Steady State Simulation

The initial verification stage for the harmonic extraction algorithm is the simulation of the proposed algorithm. Multiple simulations are done to evaluate the effectiveness of the proposed EFANF in extracting the harmonics and generating reference currents for the SAPF. For the initial simulation, the EFANF focuses on steady-state conditions for three types of loads which are pure resistive loads, inductive loads, and capacitive loads. The load parameter for the steady-state simulation is referred to Table 3.1. Based on the simulation, the result of the harmonics extraction algorithm focuses on improving the THD value acquired. The priority objective of the SAPF is to comply with the requirement of the THD value required by IEE Standard 519, which is set to be below 5%.

Hence, the effectiveness of using the proposed EFANF is assessed under the steady-state conditions of resistive, inductive, and capacitive nonlinear loads which are based on five criteria.

1. Changes of the waveform for instantaneous voltage source before and after applying SAPF.
2. Changes of the waveform for instantaneous current source before and after applying SAPF.
3. Ability to maintain the phase for the instantaneous currents source (with respect to the phase of the instantaneous voltages source).
4. Changes in THD value of instantaneous currents source before and after applying SAPF.
5. The changes of the desired value overall DC-link voltage during steady-state conditions.

Based on the criteria above, the waveforms for the simulated power system using SAPF with EFANF are shown in Figures 4.1 (resistive load), 4.2 (inductive load), and 4.3 (capacitive load). These figures display waveforms for the affected instantaneous voltage sources, current sources, load sources, and filter current sources for each load type. The sequence is as follows: the first and second figures show supply voltage and current waveforms; the third figure is the load current waveform and the final figure presents the filter current waveform. One of the characteristic studies, as mentioned in the steady state condition, is the waveform shape. The initial waveform of the current source affected by the nonlinear loads is shown in the current load waveform. From the current source shown in each of the respective Figures 4.1, 4.2, and 4.3 are after being applied by the SAPF. It highlighted that the harmonics extraction algorithm managed to mitigate the waveform of the instantaneous current source towards the sinusoidal waveform through multiple nonlinear load types and values.

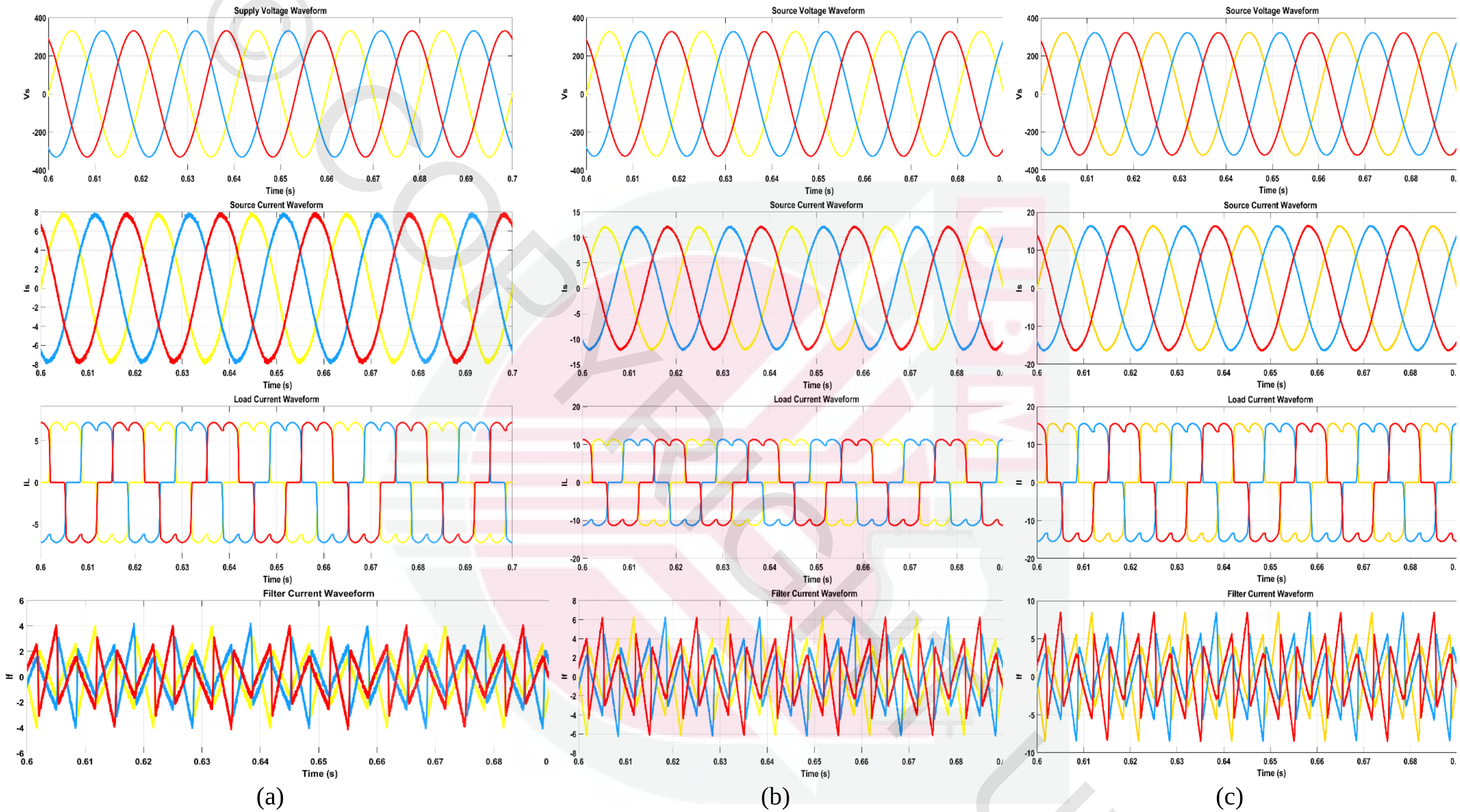

Figure 4.1: Instantaneous voltage sources, instantaneous current sources, instantaneous load sources, and filter current sources for (a) R_1, (b) R_2, and (c) R_3.

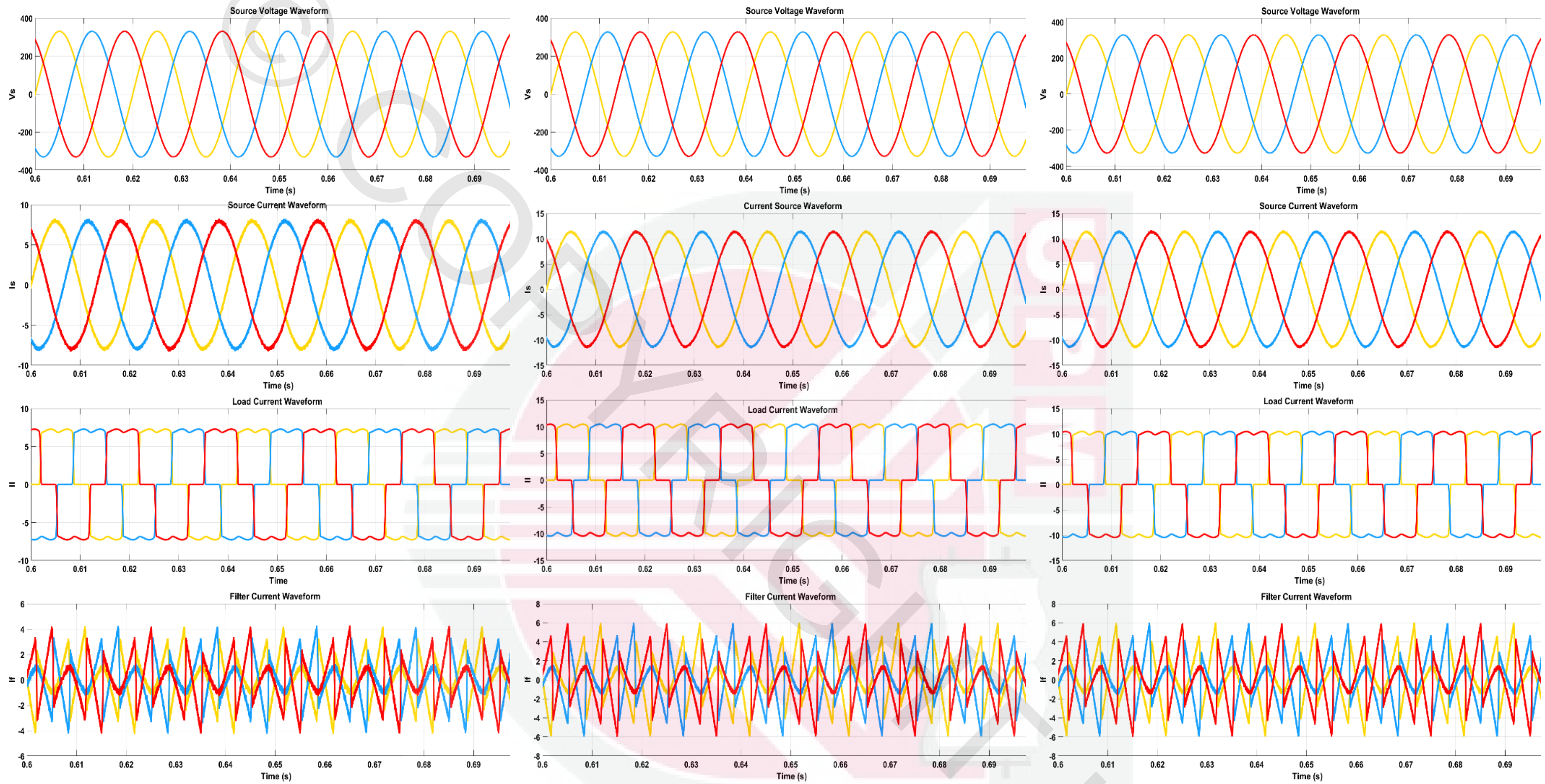

(a) (b) (c)

Figure 4.2: Instantaneous voltage sources, instantaneous current sources, instantaneous load sources, and filter current sources for (a) R_1L_1, (b) R_2L_2, and (c) R_3L_3

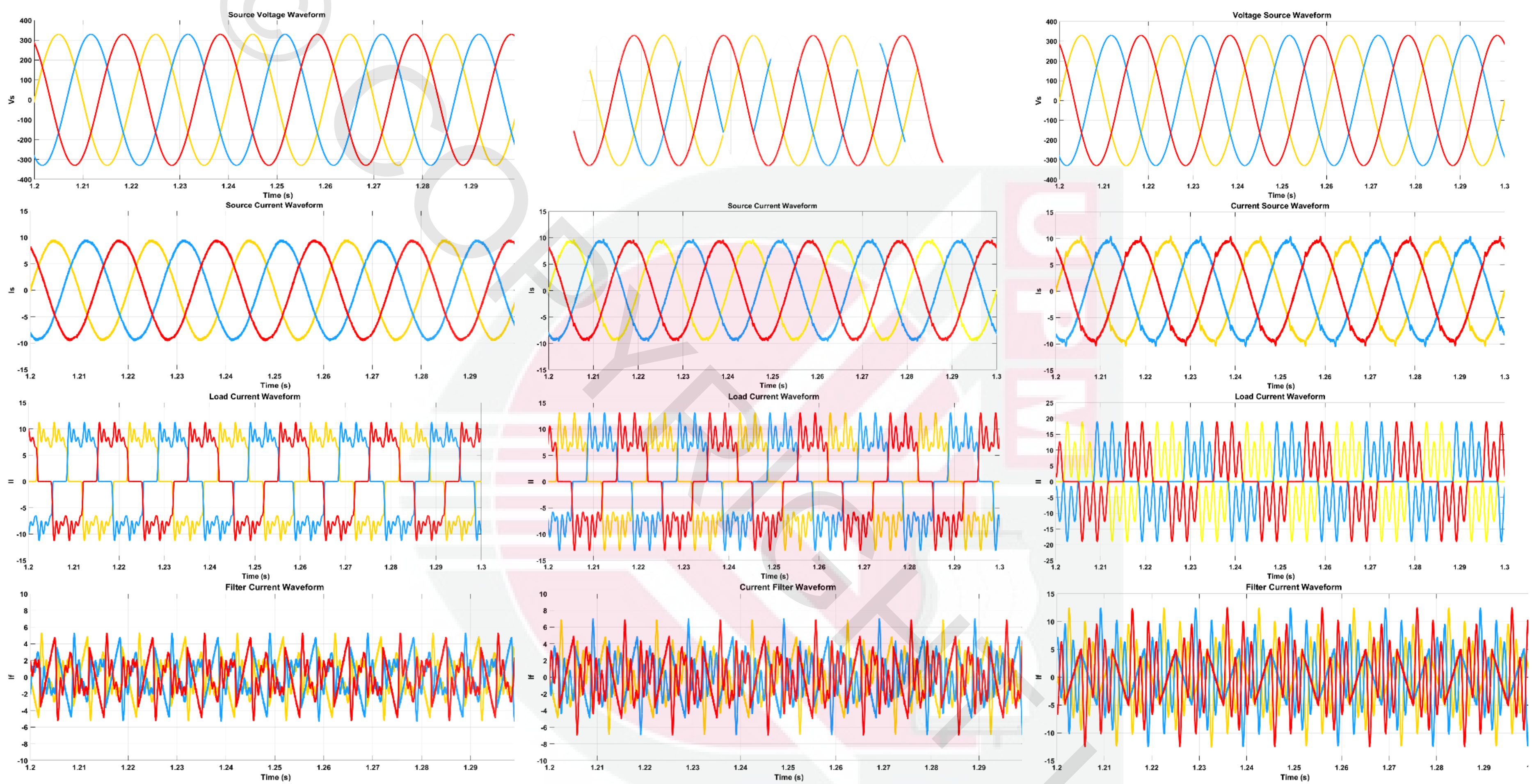

(a) (b) (c)

Figure 4.3: Instantaneous voltage sources, instantaneous current sources, instantaneous load sources, and filter current sources for (a) R_1C_1, (b) R_2C_2, and (c) R_3C_3

Another criterion of EFANF implementation in the SAPF that needs to be analyzed is the decomposition of instantaneous supply current THD value before and after compensation for all the three-loads conditions. For the results using MATLAB Simulink, the THD harmonic order is investigated until the 20th order. The results for the mentioned loads under steady-state operation are given in Figure 4.4, Figure 4.5, and Figure 4.6. From all figures, the THD values for resistive load, inductive load, and capacitive load before compensation is lingering at a value of 28.68% for R_1, 28.18% for R_2, 27.75% for R_3, 28.30% for R_1L_1, 27.80% for R_2L_2, 27.80% for R_3L_3, 32.05% for R_1C_1, 39.87% for R_2C_2 and 75.92% for R_3C_3.

After the proposed harmonic extraction is applied within the SAPF, the values of the THD after compensation achieved the designated values well below the requirement where the THD values for the respective loads are 2.46% for R_1, 1.64% for R_2, 1.25% for R_3, 2.41% for R_1L_1, 1.73% for R_2L_2, 1.25% for R_3L_3, 2.55% for R_1C_1, 2.49% for R_2C_2 and 4.22% for R_3C_3. The respective values show that the proposed EFANF can supply an effective reference current source for the SAPF to reduce the harmonic values below the required 5% IEEE standard for all the given loads.

Based on this value it shows that EFANF works effectively in generating the reference current for harmonic mitigation where the effect can be seen from the result that proposed EFANF algorithm effectively mitigate harmonics of all the multiple load types in steady-state conditions where the SAPF can lower the harmonics to be below than 5%.

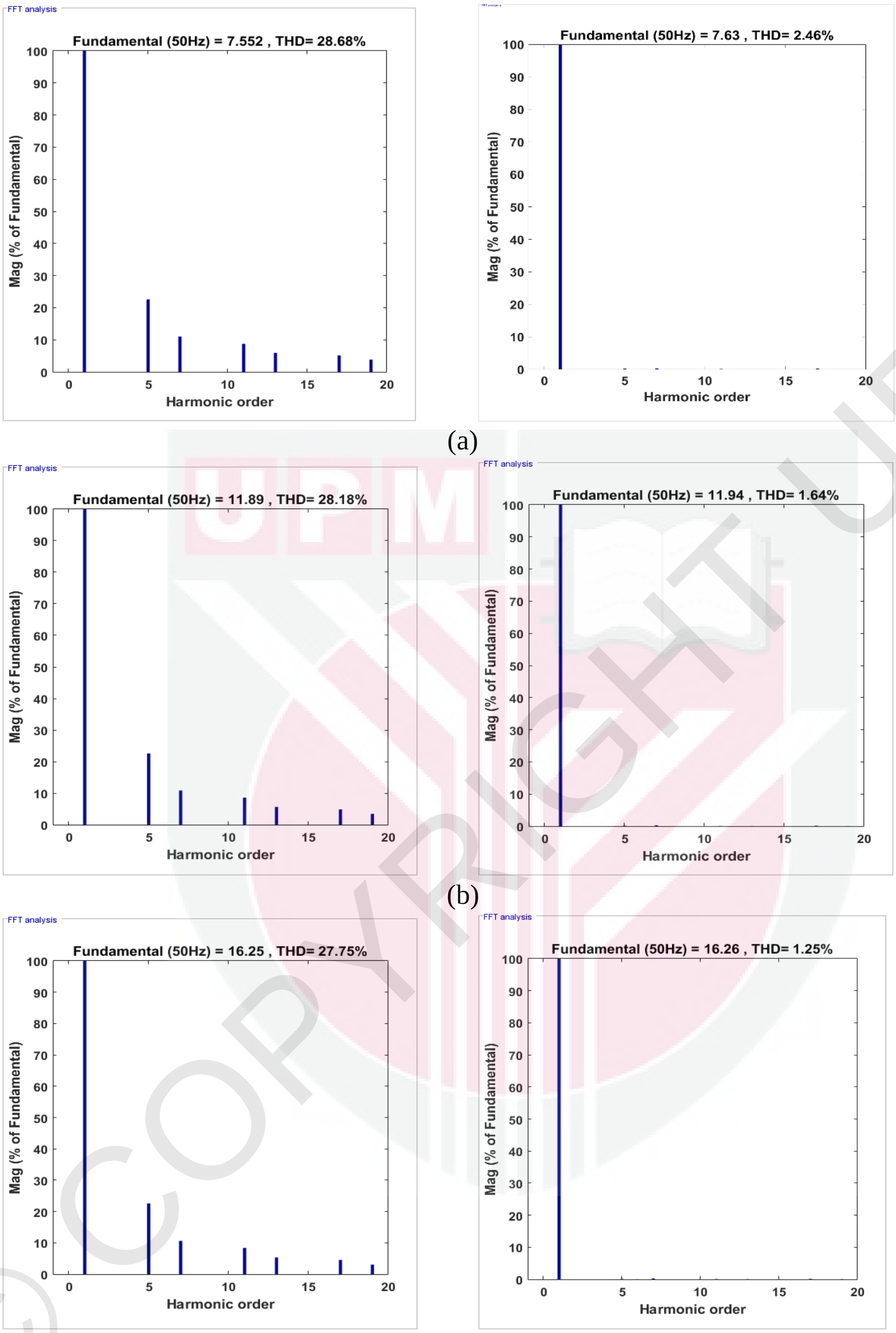

(c)

Figure 4.4: Harmonics spectrum of resistive load before and after mitigation (a) R_1 (b) R_2 and (c) R_3

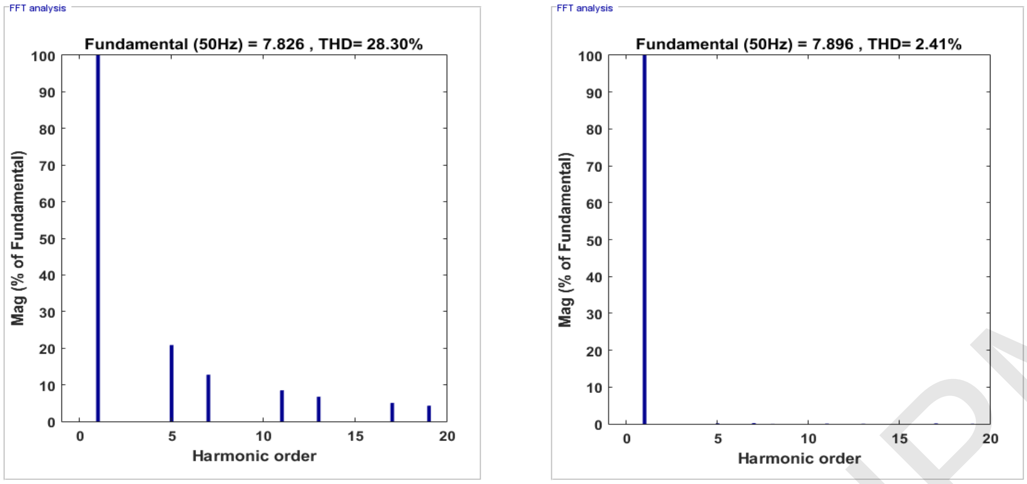

(a)

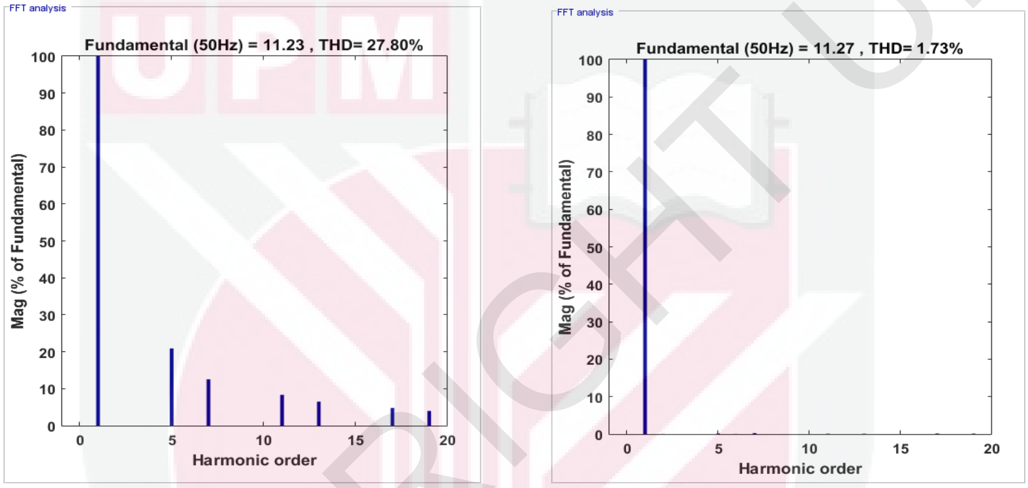

(b)

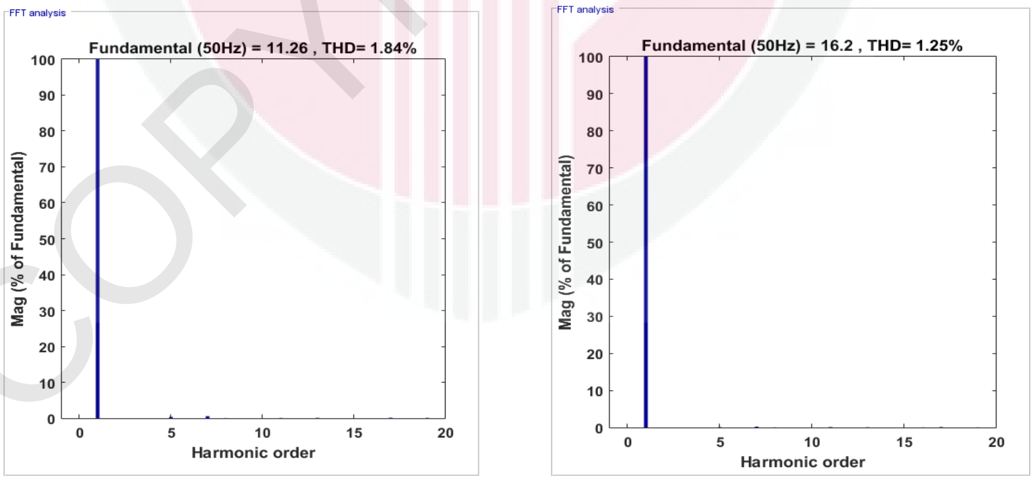

(c)

Figure 4.5: Harmonics and after mitigation for Inductive Load (a) R_1L_1 (b) R_2L_2 and (c) R_3L_3

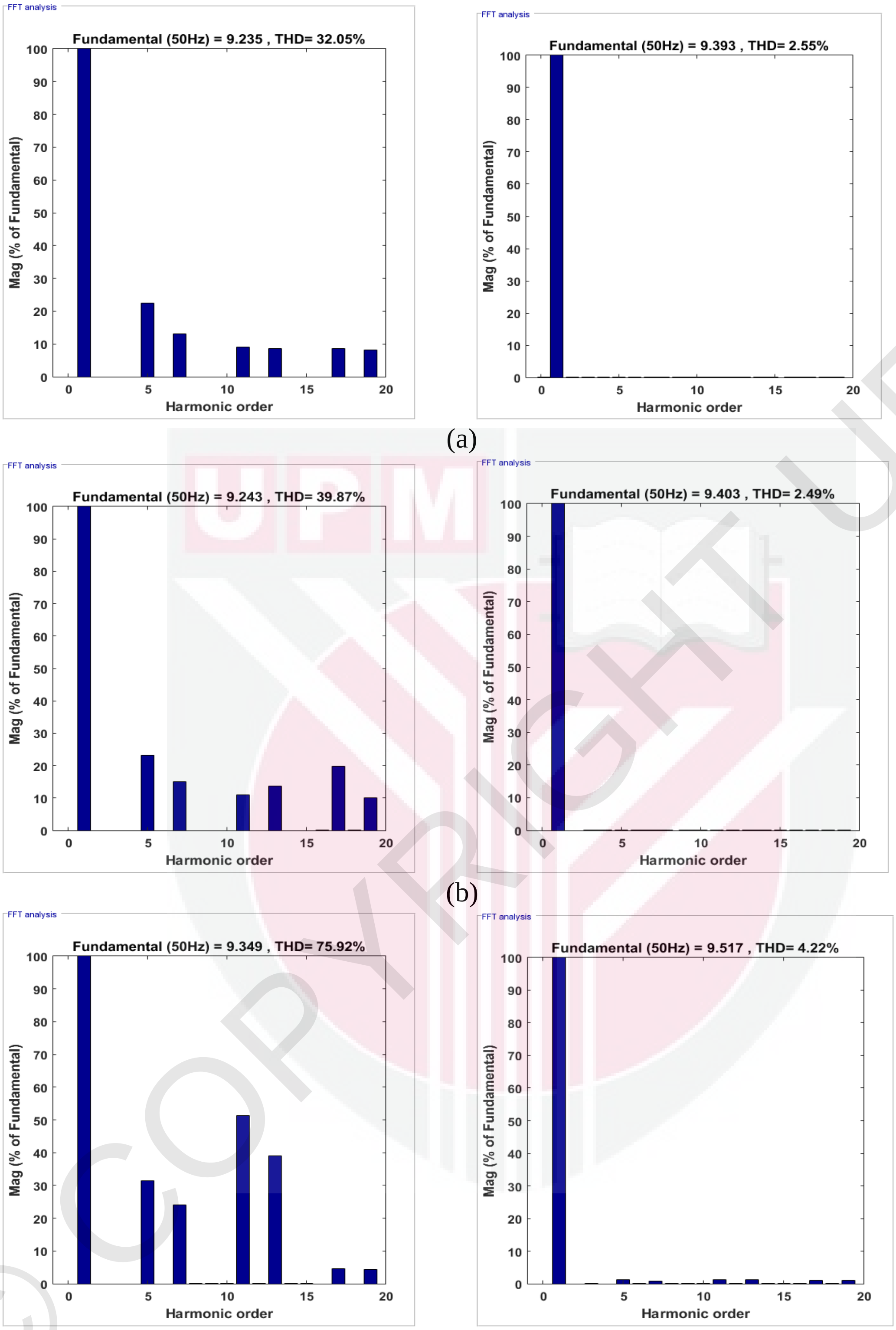

(c)

Figure 4.6: Harmonics before and after mitigation for Capacitive loads (a) R_1C_1, (b) R_2C_2, and (c) R_3C_3

A comparative analysis is also done between the proposed harmonics extraction algorithm with conventional Fryze, PQ with LP filter, and PQ with ANF to analyze the effectiveness of the EFANF algorithm. The comparison result for all the mentioned algorithms can be referred to in Figure 4.7. Based on the comparison, the proposed algorithm has the lowest THD values compared to other extraction algorithms for resistive and resistive with inductive load. For the resistive load, the EFANF has the lowest THD value, which ranges between 1.25% to 2.46 % for all the load values, while the Fryze has the highest THD ranging from 2.81% up to 3.39 %. For PQ with LP filter, the THD ranges between 1.35 % and 2.57 %, and for the PQ with ANF, the range of THD is between 1.7 % to 2.71%.

When applied to the inductive load, the EFANF algorithms also have the lowest THD, the range is between 1.25 % to 2.41% for all load values. PQ with LF filter is the second lowest, where the THD is between 1.35% to 2.48%, followed by PQ with ANF where the obtained THD value is between 1.48 % to 2.62%. The Fryze algorithm records the highest THD which is between 2.47% to 2.95%.

Meanwhile, when simulated for the capacitive load, the EFANF has the lowest THD except for R_3C_3, where the proposed algorithm is second. The range of THD for EFANF is 1.95 to 2.5%, PQ with LP filter is 2.1% to 3.19 %, PQ with ANF is 2.57 to 2.64%, and finally for Fryze algorithm is 14.17% to 14.43%. Based on this finding, EFANF have higher mitigation values compared to others algorithm dues to simplicity EFANF algorithm compares to PQ based algorithm as PQ based algorithm involve on transformation of planes with may cause delay and data loss.

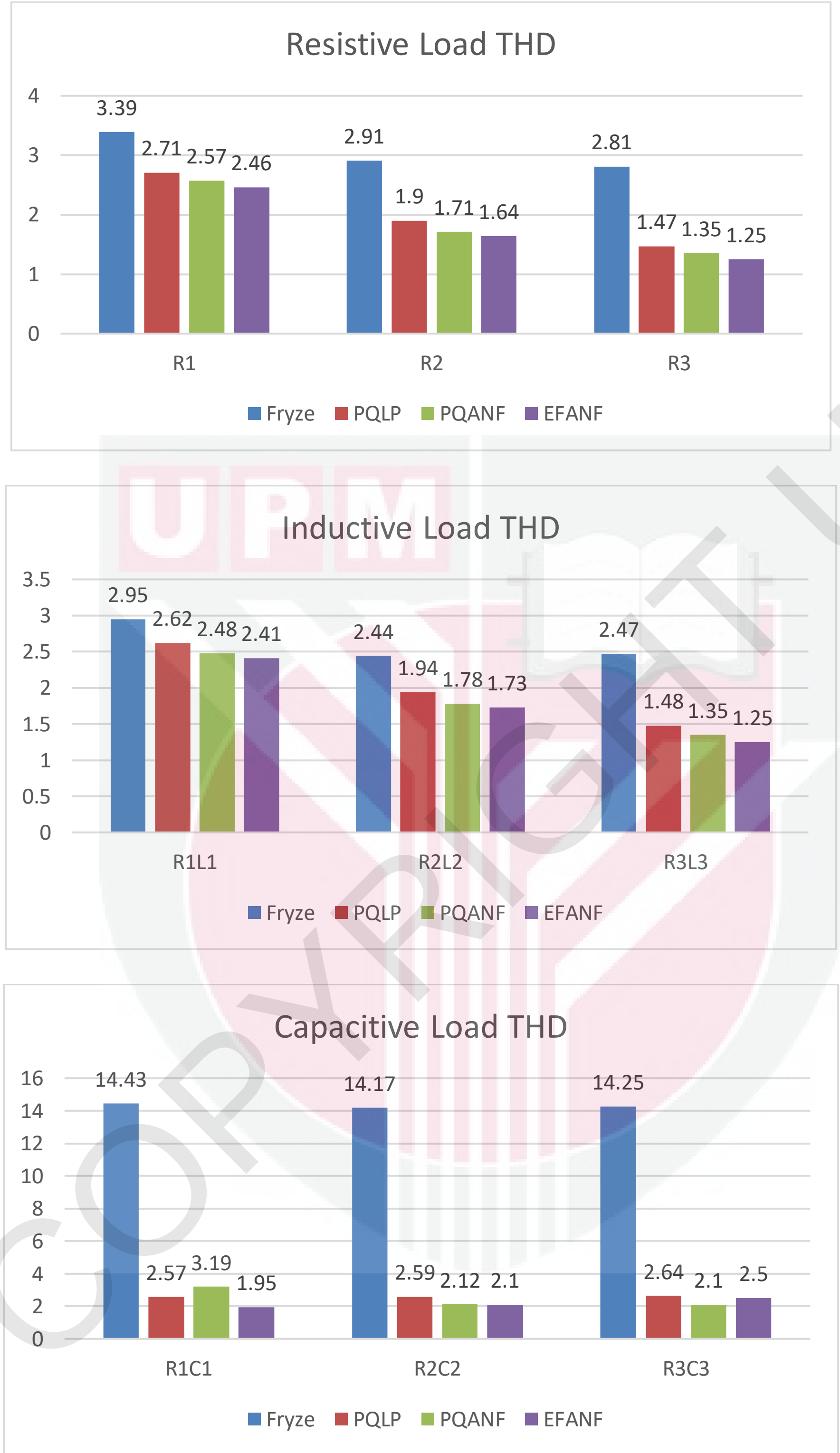

Figure 4.7: Comparison THD for resistive, inductive, and capacitive loads for Fryze, PQLP, PQANF, and EFANF.

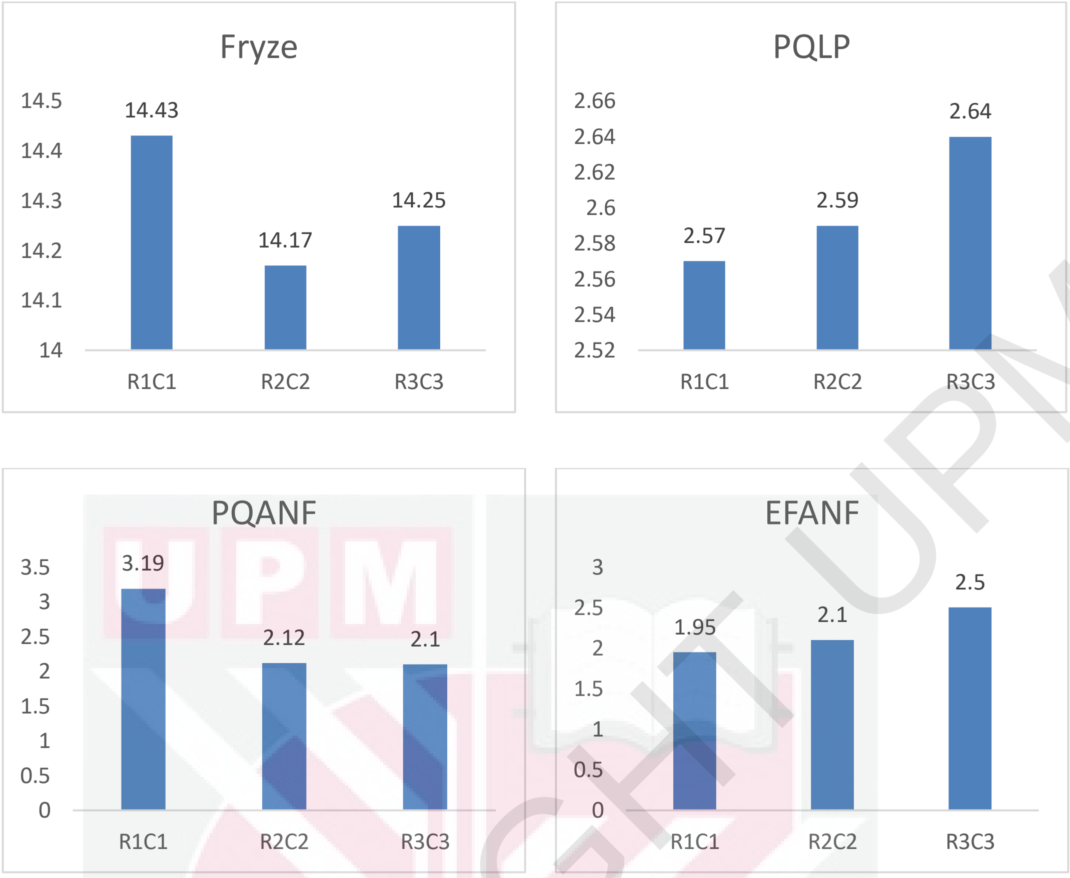

Figure 4.8: Detailed THD comparison capacitive loads for Fryze, PQLP, PQANF, and EFANF.

In terms of detailed comparison of all the harmonics extraction algorithms for capacitive loads, Figure 4.8 shows that the Fryze algorithm is the least effective in terms of obtaining the lowest THD. However, in terms of the sequence of the THD values after mitigation, the EFANF and PQLP show the same pattern of higher THD value with higher values of capacitive load but with EFANF range from 1.95% to 2.5% compared to PQLP which range from 5.7% to 2.64%.

Another notable characteristic is that PQANF responds inversely where THD decreases as the capacitor value increases, ranging from 3.19% down to 2.1% with increasing load. The THD after compensation meets the requirement of IEEE standard for almost all algorithms except for the Fryze algorithm. Nonetheless, the simulation result shows that out of all, EFANF shows the best mitigation applied to the same specification of SAPF.

This occurrence is due to characteristics of the PQANF where the algorithm has better characters in mitigation higher value of capacitive compare to others algorithm.

4.2.2 Steady State Experimental Verification

A laboratory hardware setup was developed to validate the proposed EFANF practically, as the experimental design is presented in Chapter 3. During the testing procedure, the supplied voltage of the system is set at 50Hz, 100 Vrms (line-to-line voltage). The experimental results on the utilization of the proposed EFANF algorithm with PI DC-link control for resistive loads are shown in Figure 4.9. The results include source voltages Vsa , phase a current isa, phase b current isb and phase c current isc.

The SAPF with EFANF effectively mitigates the harmonic current in steady-state condition. The measurement uses an Agilent DSO-X 2014A oscilloscope for the experimental result, which covers source voltage, source current, load current, and filter current. The THD is calculated from the measured data downloaded from the oscilloscope. The data are processed for harmonics decomposition using FFT analysis in MATLAB/Simulink. From the results, the algorithm managed to reduce the harmonics of the source current with THD from 62% to 3.46 % for 80 Ω load, 28.77% to 3.73 % for 50 Ω load, and 28.56% to 3.99 % for 36 Ω load. All harmonics are managed to be reduced below the required IEE standard, which is 5%.

Figure 4.10 depicts Total Harmonic Distortion (THD) levels for phases IA, IB, and IC across three resistor values (R_1, R_2, and R_3) which reveal distinct differences in harmonic behavior among the phases. For Phase IA, the THD increases from 2.88% at R_1 to 2.94% at R_2, and further to 3.65% at R_3, indicating a significant sensitivity to decreasing resistance values. This substantial rise in THD suggests that Phase IA is particularly prone to harmonic distortion under lower resistance conditions. Phase IB exhibits a similar trend, with THD values rising from 2.89% at R_1 to 3.13% at R_2 and reaching 3.41% at R_3. Although the increase is more gradual compared to Phase IA, it still demonstrates a clear correlation between lower resistance and higher THD, highlighting Phase IB's moderate sensitivity to resistance changes.

In contrast, Phase IC shows a different pattern. The THD for Phase IC decreases slightly from 3.2% at R_1 to 3.11% at R_2, before increasing again to 3.19% at R_3. This non-linear response suggests that Phase IC's harmonic behavior is influenced by factors beyond just the resistance changes, indicating a more complex interaction of load characteristics and harmonics. Overall, these observations underscore the varying sensitivity of each phase to load resistance. Phase IA is the most affected by decreasing resistance, displaying the highest increase in THD. Phase IB follows a similar but less pronounced trend, while Phase IC's response is more variable and complex. The difference between the phase occurred due the unbalanced between the system which caused the varying of current flow and subject to the measurement of sensor during the experiment took places.

Nevertheless, the THDs of the three-phase supply current are also monitored to see the algorithm's effectiveness in the experimental work. The figure overall shows that for the experimental work the THD values range from 2.88% to 3.65%, following the IEE standard requirement.

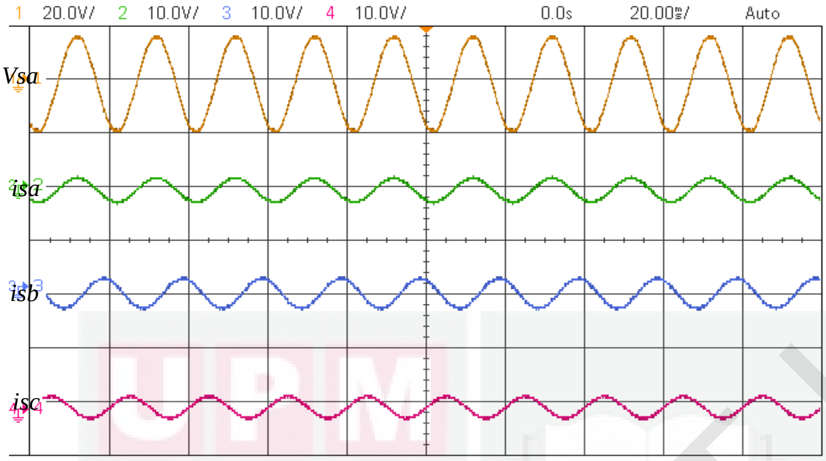

(a)

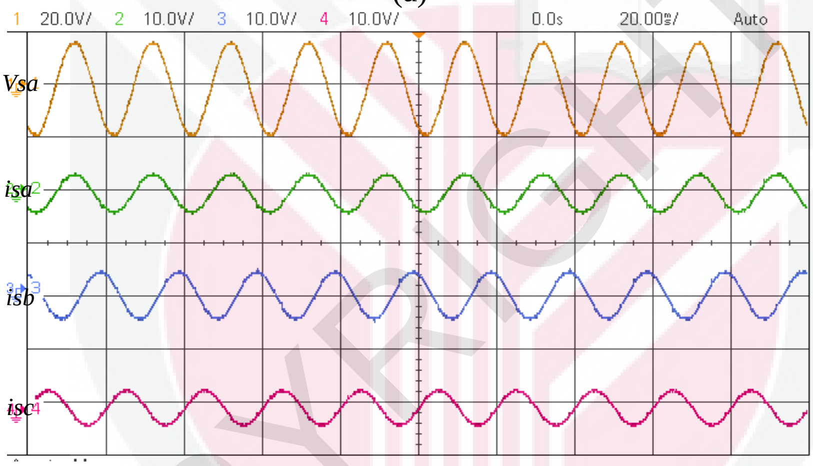

(b)

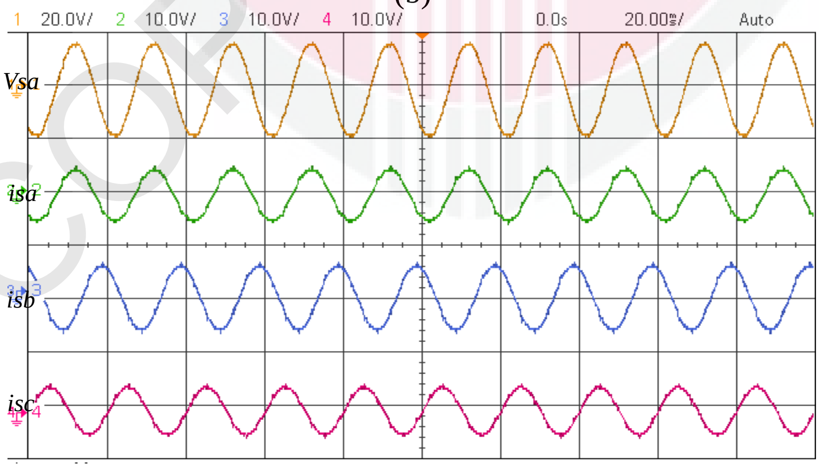

(c)

Figure 4.9: Experimental results of source voltage, phase a source current, phase b source current and phase c source current for (a) 82-Ω (b) 50-Ω and (c) 36-Ω loads.

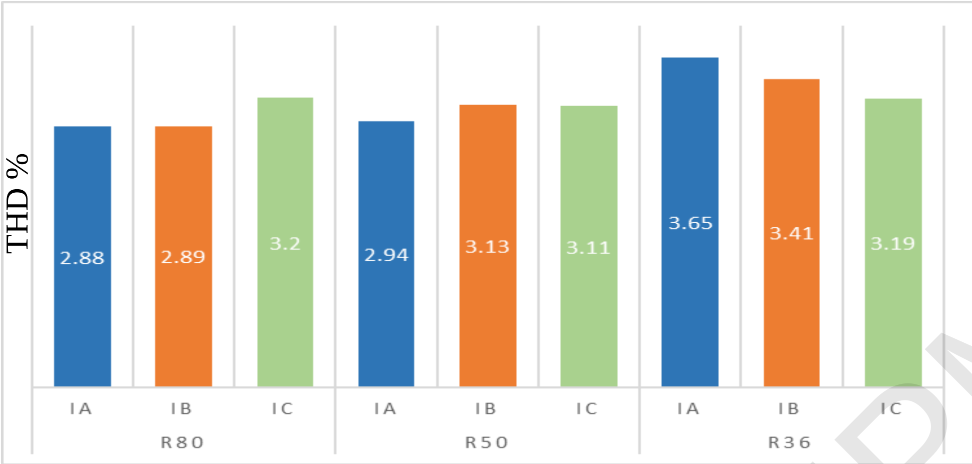

Figure 4.10: Experimental results of THD for three-phase source current after compensation.

The next experimental results are shown in Figure 4.11, highlighting waveforms of phase-a source voltage, source current, load current, and filter current in steady-state conditions for multi-resistive load values. Based on the figure, the source current waveform is in sinusoidal shape and is in phase with the measured source voltage showing that the mitigation is taking place in the source current. The given FFT harmonics analysis on the same figure shows that the harmonics are reduced as intended. Thus, THD is reduced for all the given loads to 3.46% for R_1, 3.73% for R_2, and 3.99% for R_3, respectively, as shown in the figure.

The experimental work further confirmed the proposed algorithm's response under steady-state conditions when introduced to inductive and capacitive loads, as shown in Figure 4.12 and Figure 4.13. The results indicated that the proposed algorithm successfully mitigated inductive loads with values R_1L_1, R_2L_2, and R_3L_3, reducing the THD of the source current to 2.70%, 2.63%, and 2.78%, respectively. These findings provide evidence of the proposed algorithm's effectiveness in managing THD for various loads.

The experimental work, as shown in Figure 4.13, also investigated the effectiveness of the proposed EFANF algorithm in mitigating THD for capacitive loads. The experiment results indicated that THD of the mitigated source current for capacitive loads were 2.52%, 2.99%, and 5.00% for R_1C_1, R_2C_2, and R_3C_3, respectively. These values were within the required IEEE standard, indicating the effectiveness of the proposed EFANF algorithm in producing the appropriate reference current for the SAPF to work effectively.

The THD value after mitigation can be seen is not having discrepancies in terms of values for resistive and inductive load. However, when changing into capacitive load the mitigation values of load to be decreases in terms of the increase of capacitive values. This is highly due to the shape of the load current changing drastically with the adding of capacitive value. This effect the reference current generation and reduces the effectiveness of the mitigation filter current within the SAPF.

Furthermore, the SAPF was observed to have better stabilities for resistive and inductive loads than capacitive loads. However, the EFANF algorithm could mitigate THD for all loads in the experimental setup. These findings suggest that the proposed EFANF algorithm effectively manages THD for different loads, which, as exposed in the experimental work, consist of resistive, inductive, and capacitive loads, and can be a valuable tool for improving power quality in electrical systems.

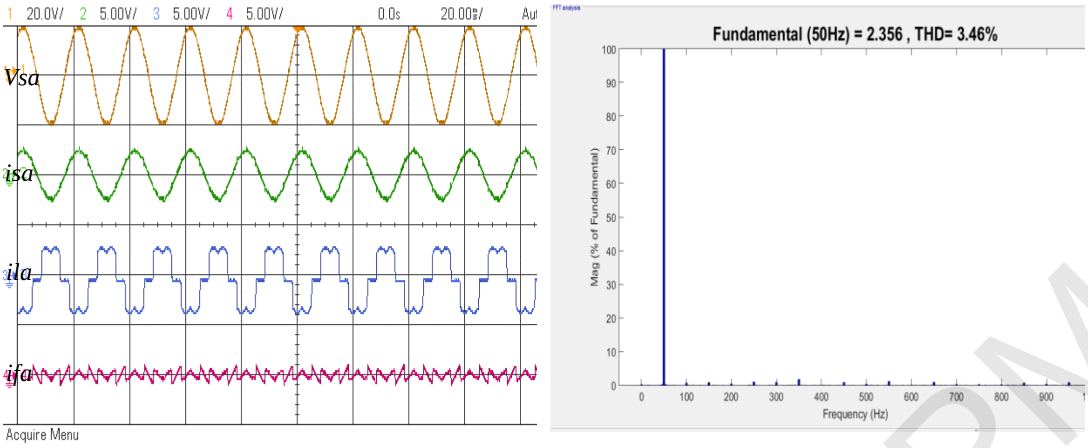

(a)

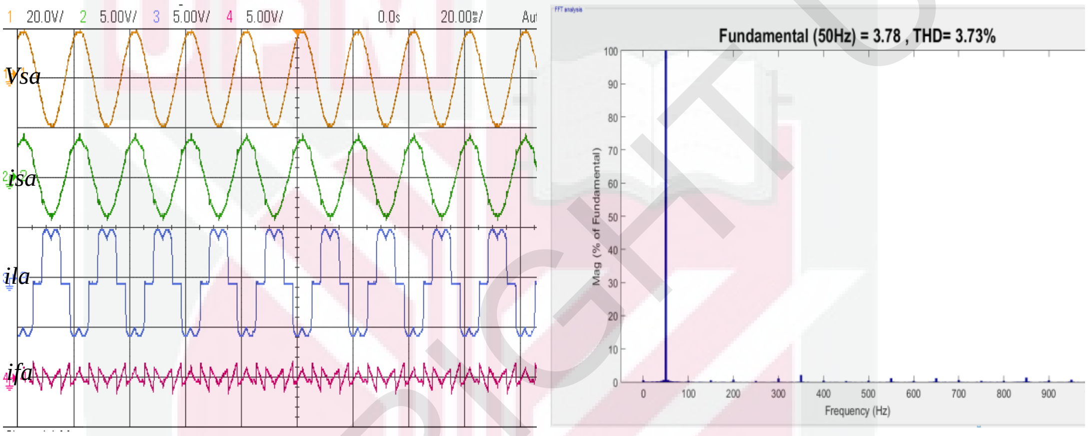

(b)

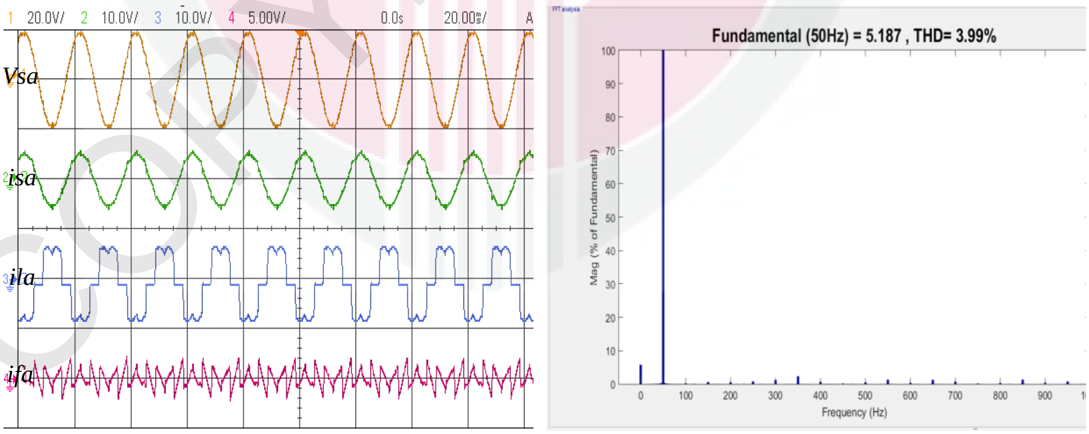

(c)

Figure 4.11: Experimental results of source voltage, source current, load current, filter current, and THD values for (a) R_1 = 82-Ω (b) R_2 = 50-Ω and (c) R_3 = 36-Ω loads.

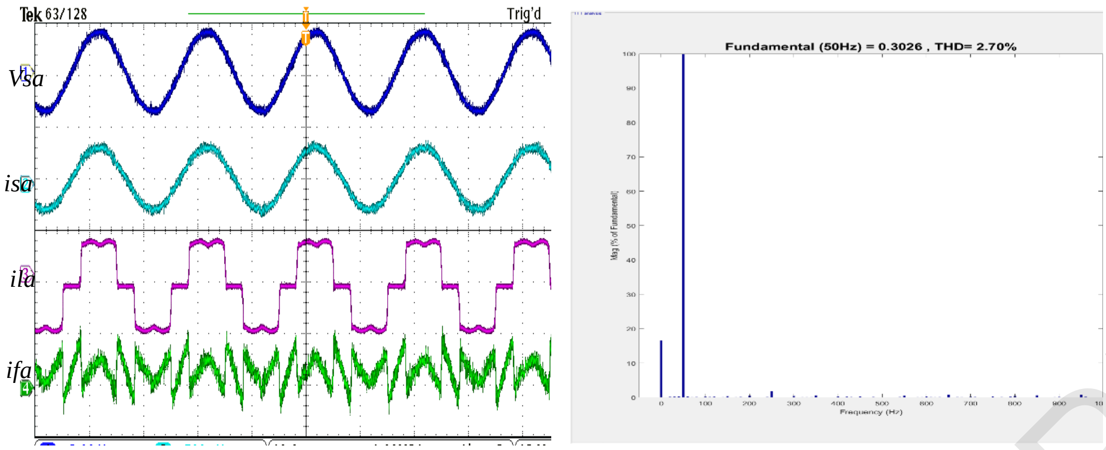

(a)

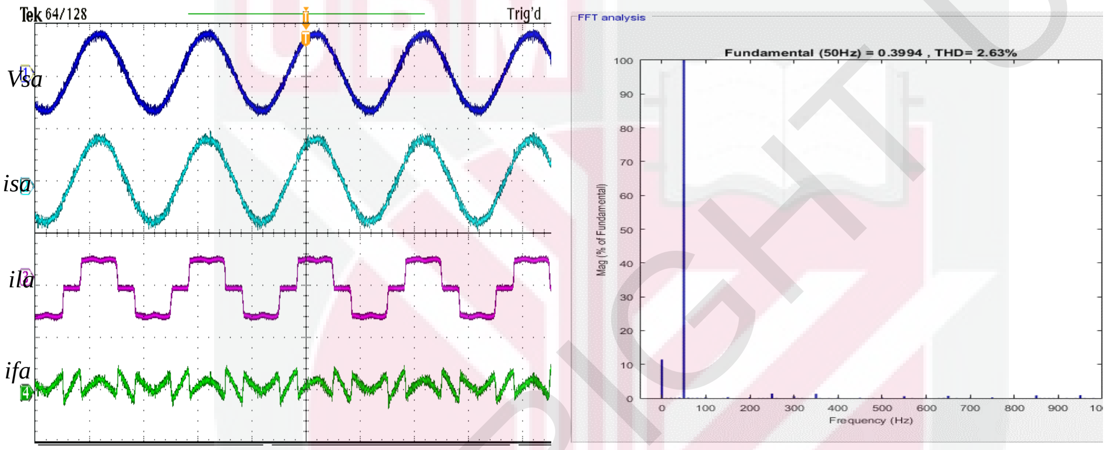

(b)

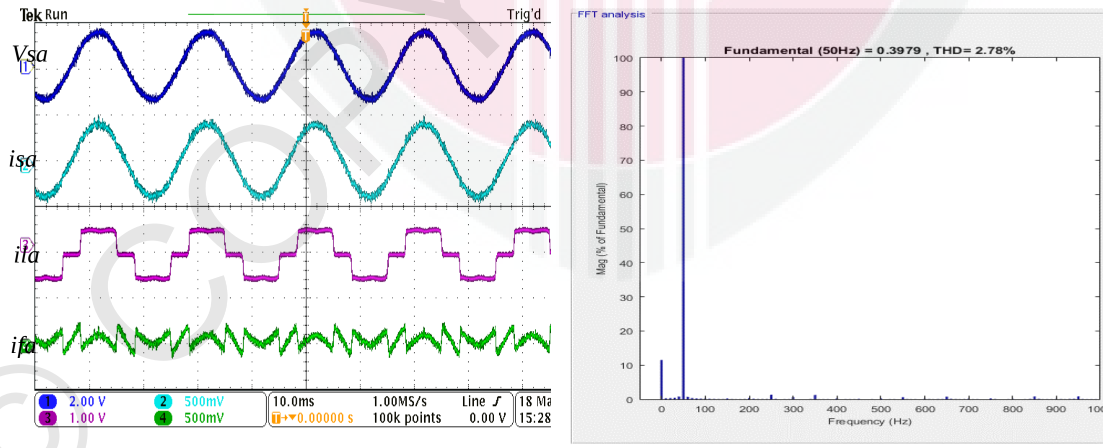

(c)

Figure 4.12: Experimental results of source voltage, source current, load current, filter current and THD values for (a) R_1L_1 = 67-Ω and 30mH (b) R_2L_2 = 69-Ω and 36mH and (c) R_3L_3 = 76-Ω and 41mH loads.

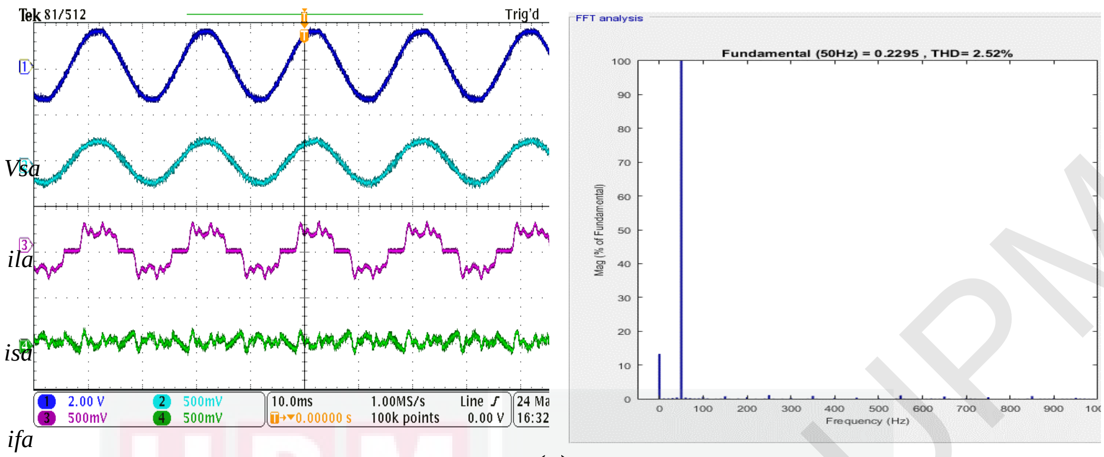

(a)

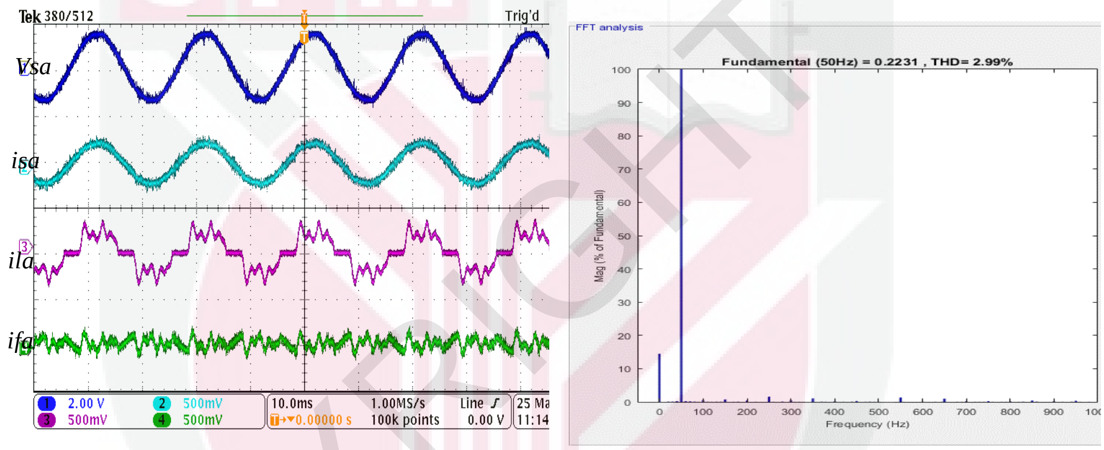

(b)

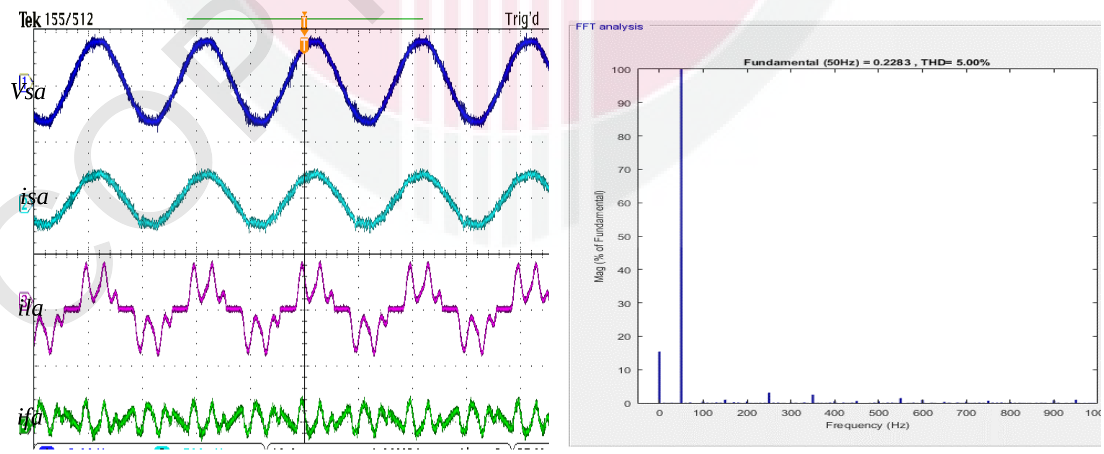

(c)

Figure 4.13: Experimental results of source voltage, source current, load current, filter current and THD values for (a) R_1C_1 = 60-Ω and 12uF, (b) R_2C_2 = 60-Ω and 17uF and (c) R_3C_3 = 60-Ω and 36uF loads.

Table 4.1: THD values before and after mitigation.

LOAD TYPE	ORIGINAL THD	THD AFTER MITIGATION (SIMULATION)	THD AFTER MITIGATION (EXPERIMENT)
R_1	28.68 %	2.41 %	3.46 %
R_2	28.18 %	1.64 %	3.73 %
R_3	27.75 %	1.25 %	3.99 %
R_1L_1	28.30 %	2.41 %	2.70 %
R_2L_2	27.80 %	1.73 %	2.63 %
R_3L_3	27.80 %	1.25 %	2.78 %
R_1C_1	73.91 %	2.55 %	2.52 %
R_2C_2	74.24 %	2.49 %	2.99 %
R_3C_3	74.68 %	4.22 %	5.00 %

The overall results of mitigation based on load types for steady state load are given in Table 4-1. The results show that the mitigation using EFANF has been effective in reducing the THD values for all load types. The results from simulations and experiments are consistent, though experimental values tend to be slightly higher than the simulated ones, which could be due to practical implementation challenges and non-ideal conditions not captured in simulations. RC loads, initially having higher THD values, also see substantial improvements of post-mitigation.

4.2.3 Transient State Simulation

The proposed algorithm is simulated to evaluate the adaptableness of the EFANF. The second criterion to be assessed for validating the effectiveness of the proposed algorithm is the capabilities of the algorithm to work efficiently in the dynamic state. The proposed algorithm is simulated under a dynamic-state condition where two dynamic load changes will be tested. The first dynamic condition is the change in value for the same load condition. In this simulation, the load values will change between three resistive loads, three inductive loads, and three capacitive loads. The changes in values will directly affect the amount of current and harmonics in the system. The weight of the load is simulated in terms of increasing and decreasing values to test the algorithm's response.

The adaptiveness of the proposed EFANF simulation result for dynamic state condition is shown in Figure 4.14 to Figure 4.17 for resistive load, Figure 4.18 until Figure 4.21 for inductive loads, and Figure 4.22 until Figure 4.25 for capacitive loads.

For the first dynamic analysis of resistive load, Figures 4.14 shows the source voltage, load current, and source current for decreased simulation load values. Figure 4.15 shows the reference, compensation, and filter current under a single-phase study. In contrast, Figures 4.16 and 4.17 show the same output during the increased simulation load. The transition changing time is given at 1s from 80Ω to 50Ω and from 36Ω to 50Ω in terms of value and the second transition time at 2s form 50Ω to 36Ω and from 50Ω to 80Ω. Based on the transition point at 1s and 2s, for both figures, the proposed algorithm maintained the sinusoidal shape of the source current waveform, as shown in Figure 4.14. During the transient from 86Ω to 50Ω, the source current increased from 7.882 A to 12.15 A, and the load current increased from 7.092 A to 11.39 A. Also, there are little changes within the source voltage values at the time of transition.

In terms of compensation and filter current, the values of each corresponding current also increased, where compensation current increased from 0.5394 A to 0.5853 A and filter current rose from 3.868 to 5.999A, as shown in Figure 4.15. For the second transient point of 50Ω to 36Ω, the respective changes are source current rose from 12.19 A to 15.85 A, load current from 11.33 A to 15.56 A, compensation current from 0.5863 A to 0.726 A, and filter current from 6.218 A to 8.772 A. Figure 4.16 and 4.17 show the dynamic conditions in inverse value where the changes are from 36Ω to 50Ω and 80Ω. This is due to the load change decrease the resistance thus increase the current. However, the waveform of the current source is maintained, and the respective output values are still maintaining the same range as the initial transition condition.

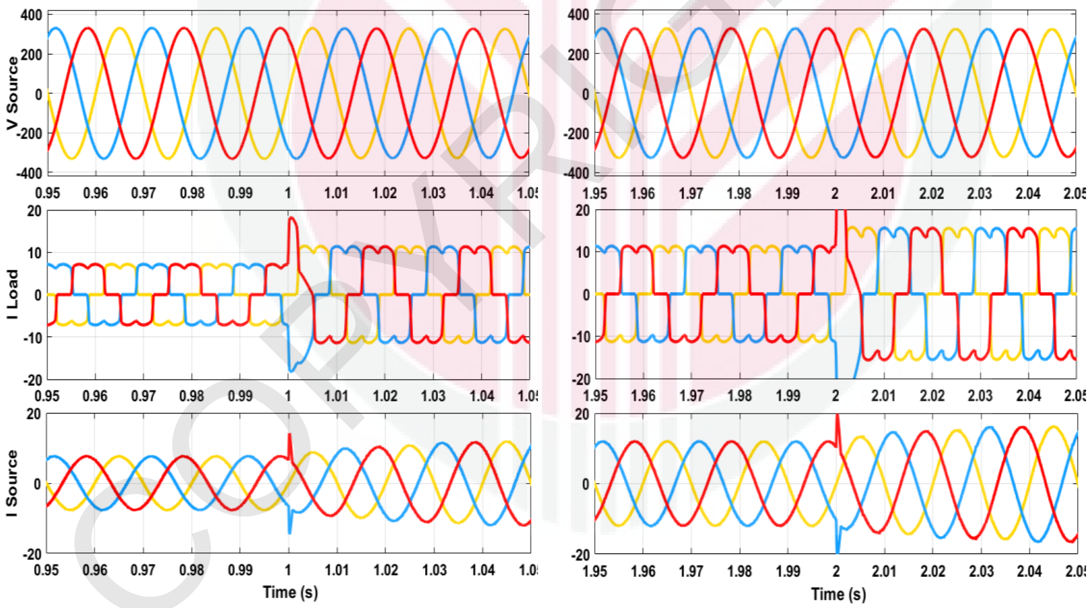

(a) (b)

Figure 4.14: Simulation results of source voltage, load current, and source current under transient-state conditions of (a) 86Ω to 50Ω and (b) 50Ω to 36Ω.

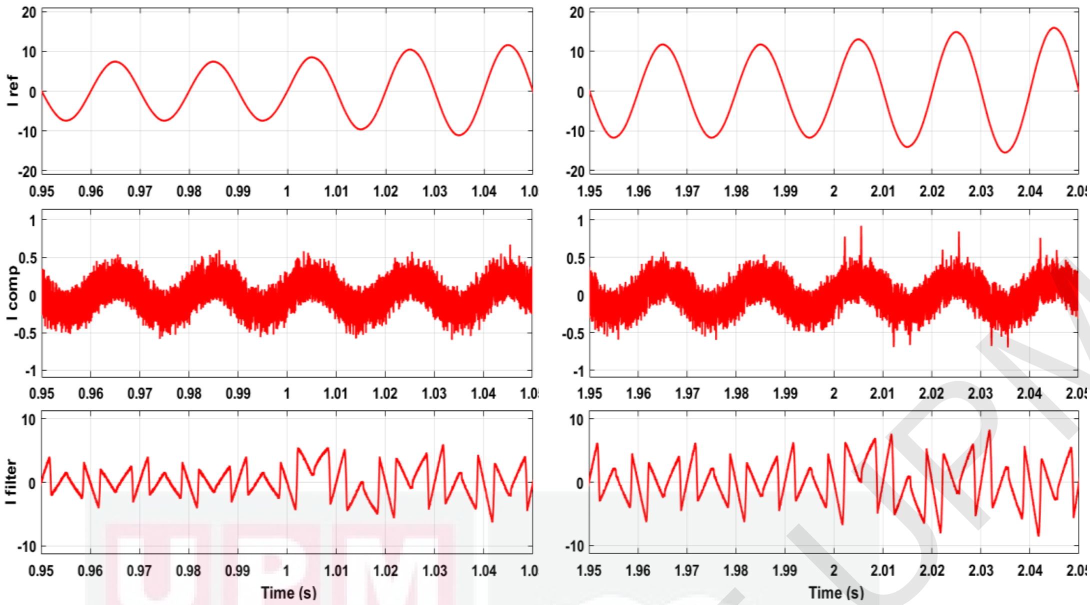

(a) (b)

Figure 4.15: Simulation results of reference current, compensation current, and filter current under transient-state conditions for (a) 80Ω to 50Ω and (b) 50Ω to 36Ω

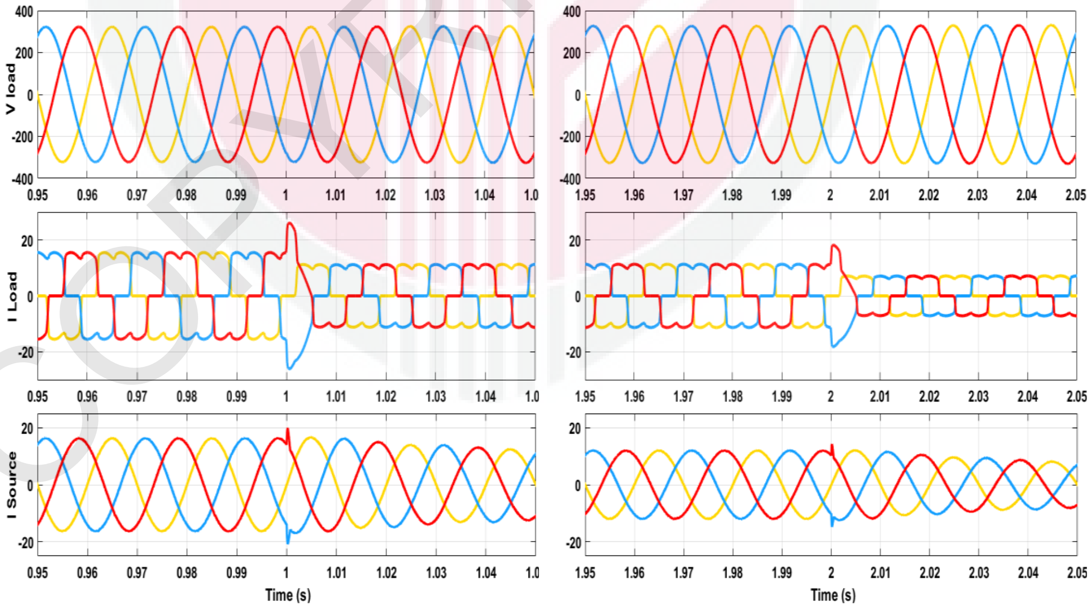

(a) (b)

Figure 4.16: Simulation results of source voltage, load current, and source current under transient-state conditions of (a) 36Ω to 50Ω and (b) 50Ω to 80Ω.

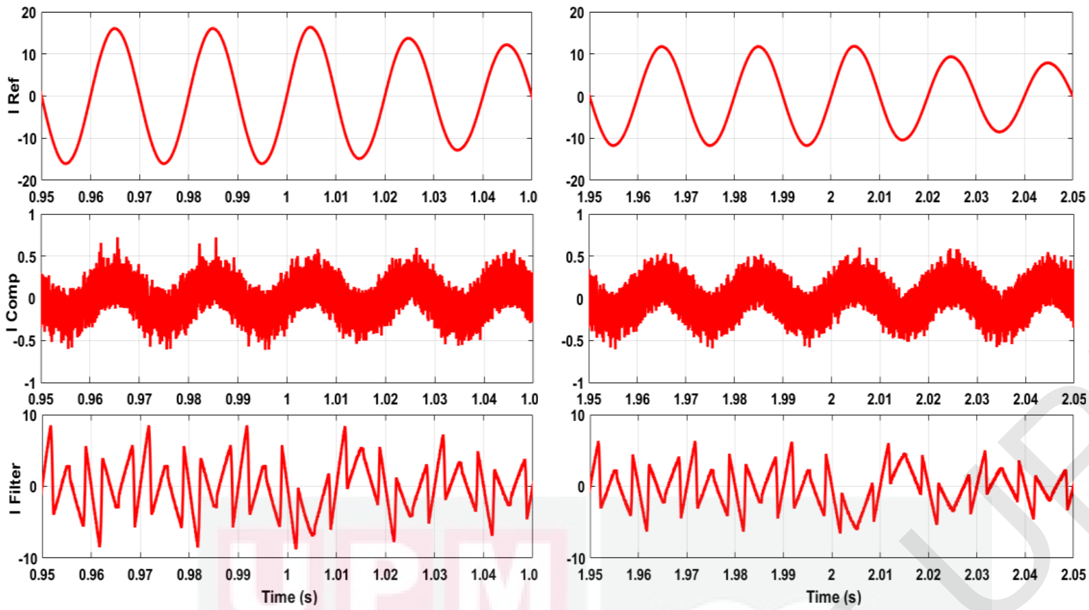

(a) (b)

Figure 4.17: Simulation results of reference current, compensation current, and filter current under transient-state conditions for (a) 36Ω to 50Ω and (b) 50Ω to 80Ω

The second load change being simulated is resistive with inductive load. Figures 4.18 and 4.20 show the three-phase waveform of source voltage, load current, and source current, while figures 4.19 and 4.21 represent the reference current, compensation current, and filter current under two transitions point which at are 1s from 77Ω and 77 mH to 53Ω and 53 mH followed by from 36Ω and 36 mH to 53Ω and 53 mH and at 2s from 53Ω and 53 mH to 36Ω and 36 mH followed by 53Ω and 53 mH to 77Ω and 77 mH. Same as the previous load, under the changes of different load values, the proposed algorithm managed to maintain the waveform of the source current within the desired sinusoidal waveform at both transition points for both decreased and increased load values. During the transition range, the current changes for the transition point are from 7.217 A to 10.31 A and rise to 14.91 A, and inversely for load value changes with reverse setting showing the algorithm adapt to changes.

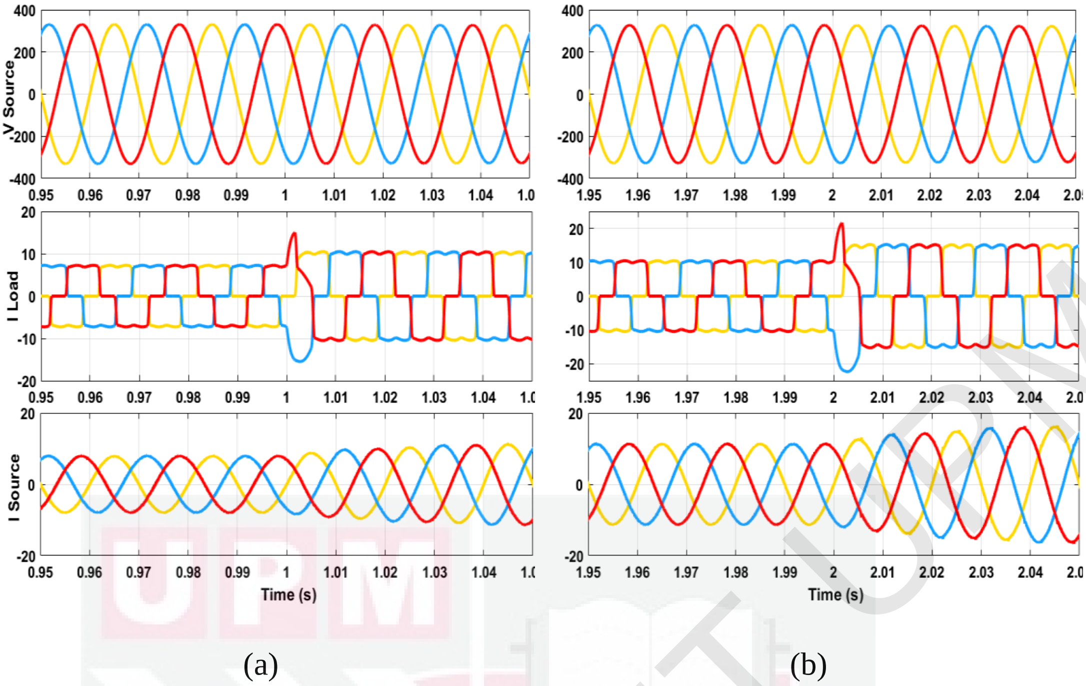

Figure 4.18: Simulation results of source voltage, load current, and source current under transient-state conditions of (a) R = 77Ω and L= 77 mH to R = 53Ω and L = 53 mH and (b) R = 53Ω and L= 53 mH to R = 36Ω and L = 36 mH

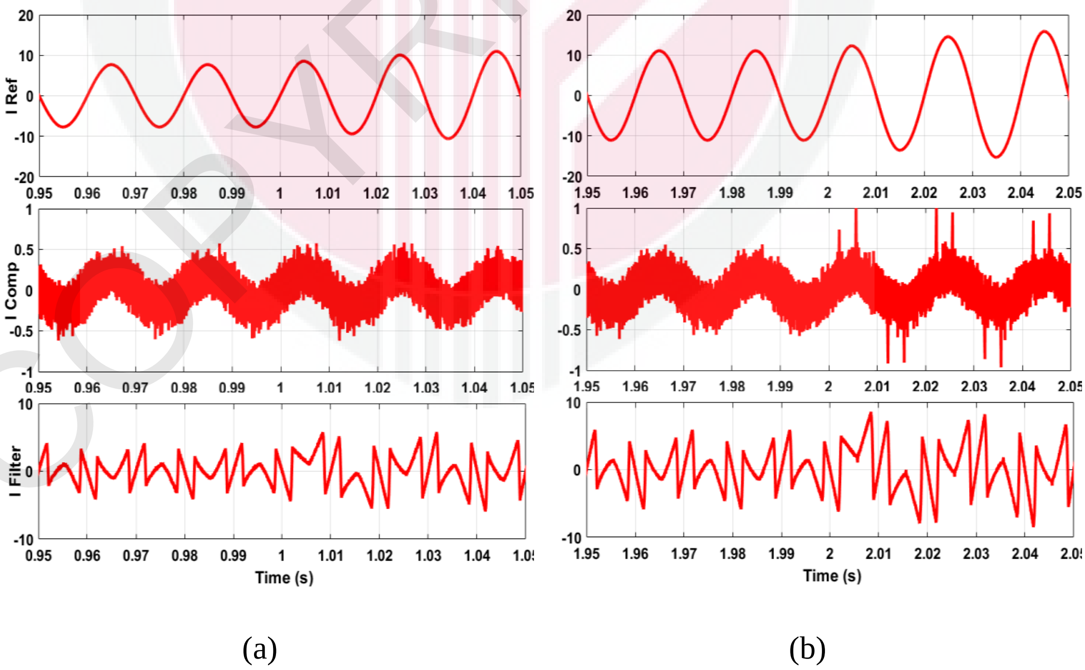

Figure 4.19: Simulation results of reference current, compensation current, and filter current under transient-state condition for (a) R = 77Ω and L= 77 mH to R = 53Ω and L = 53 mH and (b) R = 53Ω and L= 53 mH to R = 36Ω and L = 36 mH

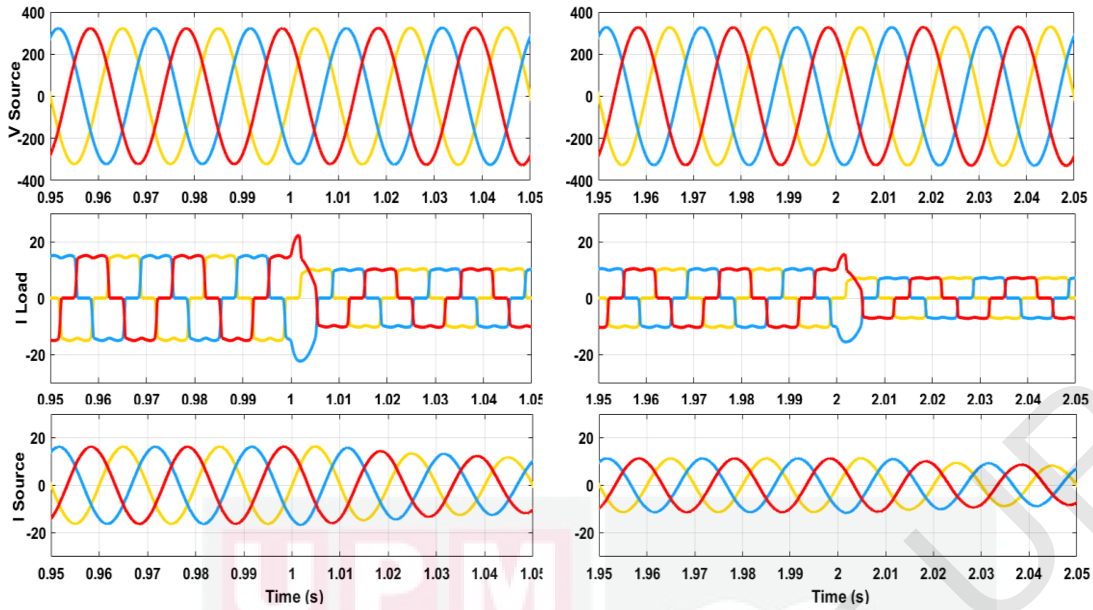

(a) (b)

Figure 4.20: Simulation results of source voltage, load current, and source current under transient-state conditions of (a) R = 36Ω and L= 36 mH to R = 53Ω and L = 53 mH and (b) R = 53Ω and L= 53 mH to R = 77Ω and L = 77 mH

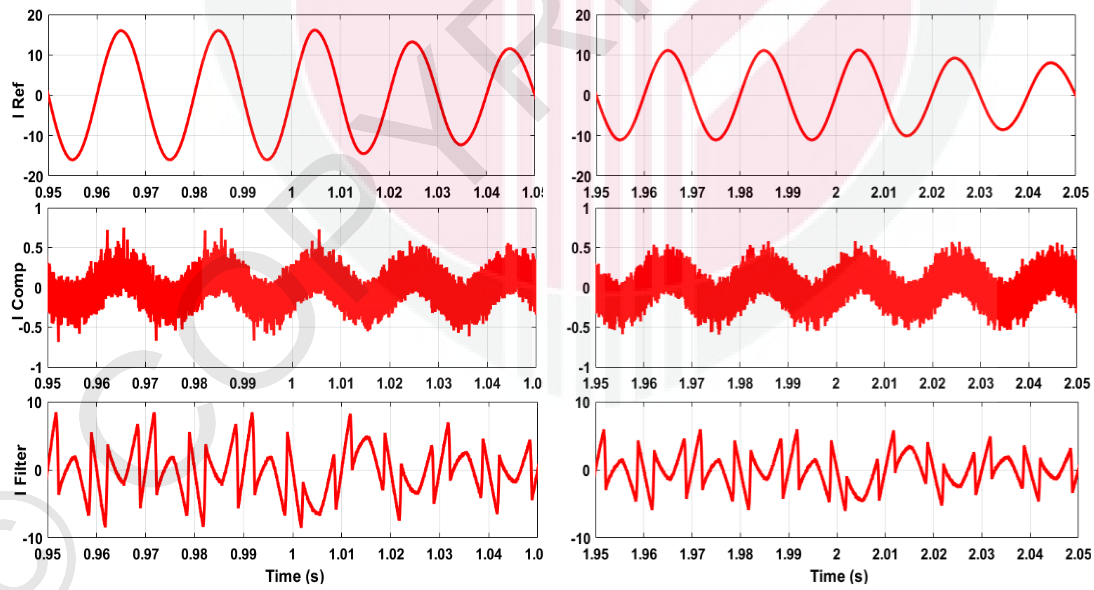

(a) (b)

Figure 4.21: Simulation results of the reference current, compensation current, and filter current under transient-state condition for (a) R = 36Ω and L= 36 mH to R = 53Ω and L = 53 mH and (b) R = 53Ω and L= 53 mH to R = 77Ω and L = 77 mH

The final simulation for the load change is the capacitive load. The three-phase waveform of source voltage, load current, and source current are shown in Figures 4.22 and 4.24. In contrast, reference current, compensation current, and filter current are given in Figures 4.23 and 4.25 for two transition points which are at 1s from 50Ω and 36 uF to 50Ω and 19 uF followed with 15Ω and 17uF to 50Ω and 19uF and at 2s from 50Ω and 19uF to 50Ω and 17 uF followed by 50Ω and 19uF mH to 50Ω and 36uF. Based on the output waveform, the proposed algorithm maintain the waveform of the source current within the desired sinusoidal waveform at both transition points for both decreased load values and increased load values. During the transition range, the current changes for the transition point are from maintaining around 11.38 A to 12.26 A for all the transition during the increased and decreased load values. However, significant changes occurred within the load current's shape due to an increase in the capacitive value where it caused spike during transition.

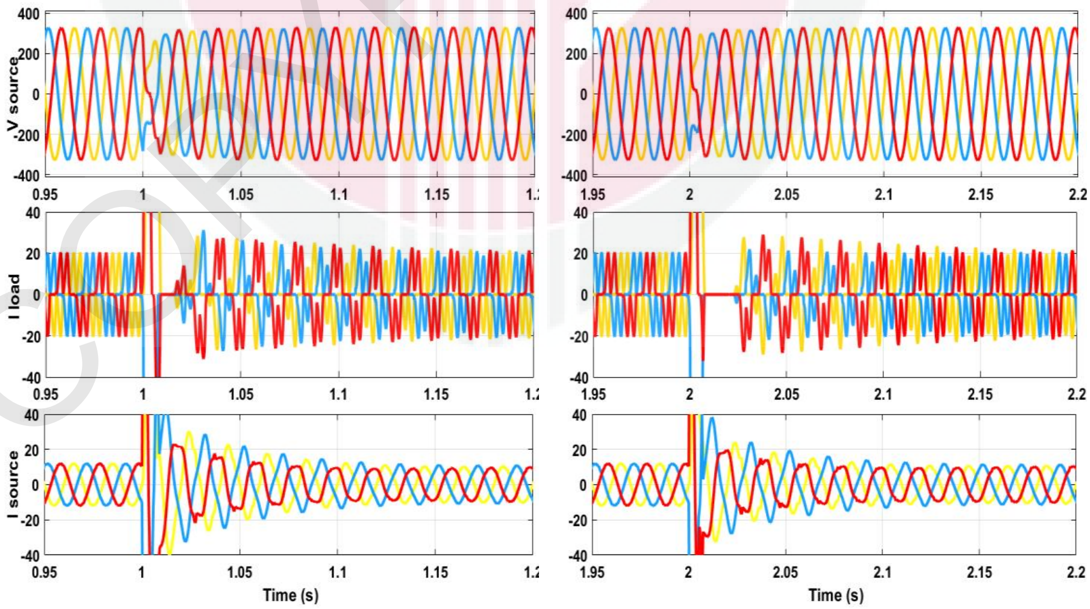

(a) (b)

Figure 4.22: Simulation results of source voltage, load current, and source current under transient-state conditions of (a) R = 50Ω and C= 36 uF to R = 50Ω and C= 19 uF, and (b) R = 50Ω and C= 19 uF to R = 50Ω and C= 17 uF

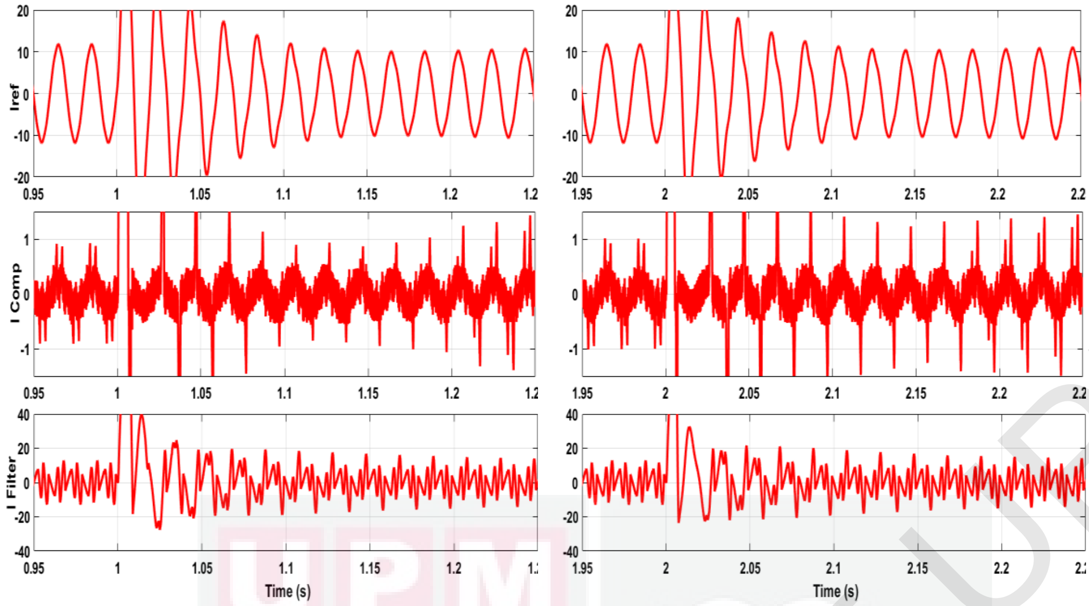

(a) (b)

Figure 4.23: Simulation results of reference current, compensation current, and filter current under transient-state conditions for (a) R = 50Ω and C= 36 uF to R = 50Ω and C= 19 uF, and (b) R = 50Ω and C= 19 uF to R = 50Ω and C= 17 uF

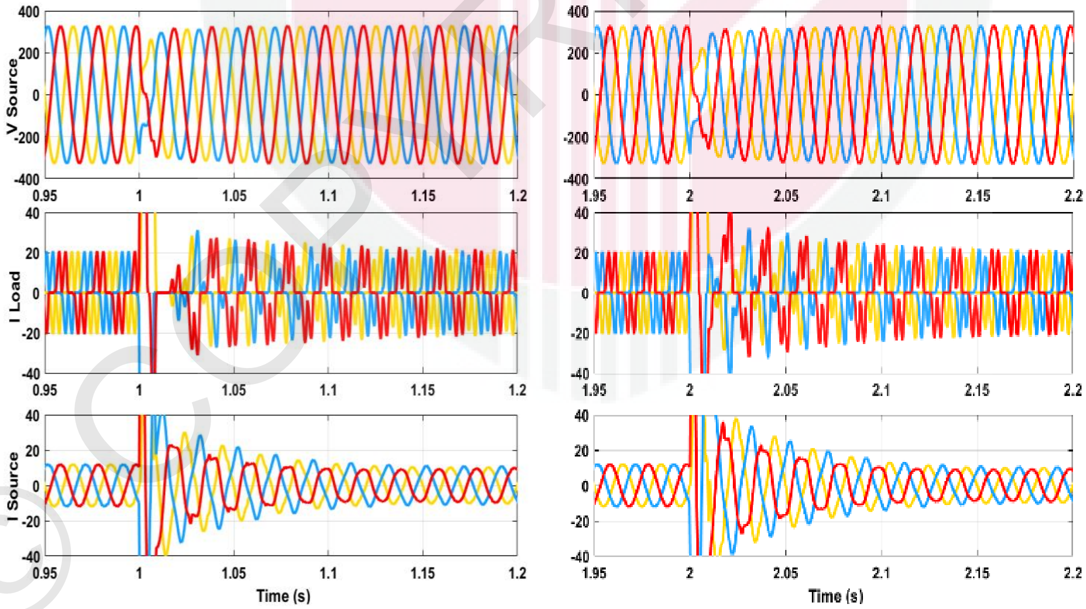

(a) (b)

Figure 4.24: Simulation results of source voltage, load current, and source current under transient-state conditions of (a) R = 50Ω and C= 17 uF to R = 50Ω and C= 19 uF, and (b) R = 50Ω and C= 19 uF to R = 50Ω and C= 36 uF.

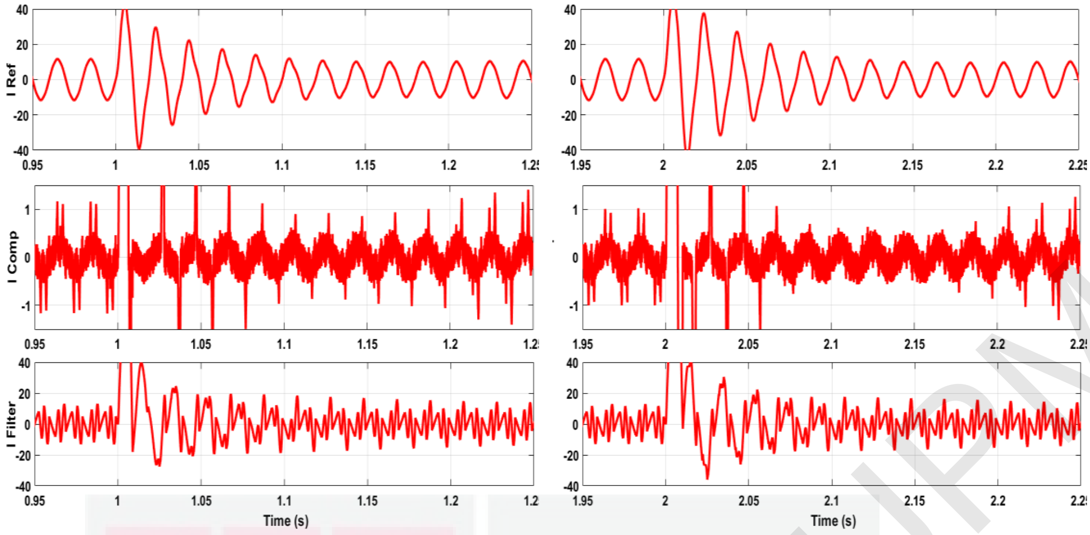

(a) (b)

Figure 4.25: Simulation results of reference current, compensation current, and filter current under transient-state conditions for (a) R = 50Ω and C= 17 uF to R = 50Ω and C= 19 uF, and (b) R = 50Ω and C= 19 uF to R = 50Ω and C= 36 uF

The proposed EFANF is also tested for its robustness and adaptability of changes by introducing it to changes in load types. The changes introduced to the SAPF are pure resistive to inductive load, pure resistive to capacitive load, capacitive to inductive load, and capacitive to inductive load. During the second stage of the dynamic-stage operation, the performance of the waveforms being assessed are source voltage, source current, load current and filter current and compensation signal. During this stage, the waveform is evaluated on the changes of shapes and the sustainability of the APF.

Simulation results of load changes from purely resistive load to inductive and capacitive loads are given in Figure 4.26. Based on the figure shown, the proposed algorithm managed to mitigate the load type changes as the changes are induced in the simulation where the source current maintain within 12 A sinusoidal source waveform within the changes time is around 0.01s. The time of changes of the load is defined at 1.0s.

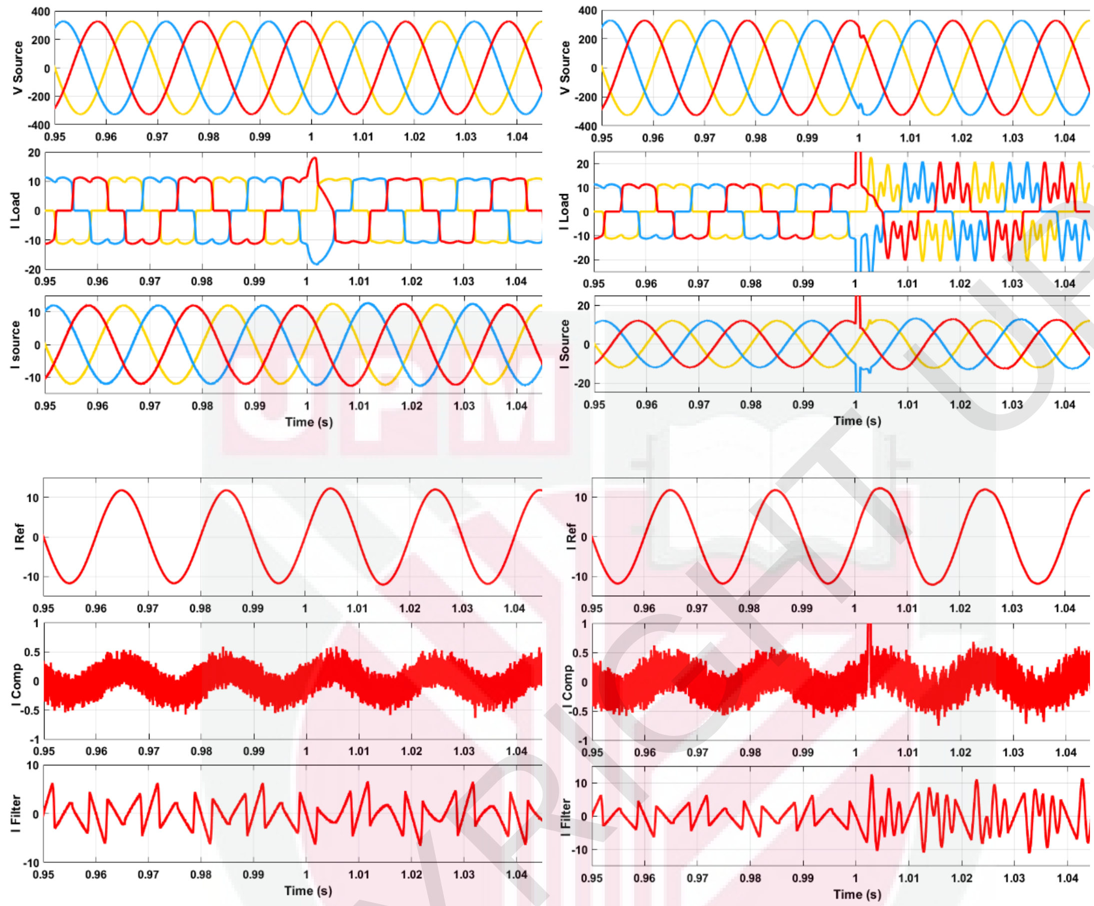

(a) (b)

Figure 4.26: Simulation results of source voltage, load current, source current, reference signal, compensation signal, and filter current for load changes from (a) resistive to inductive load (b) resistive to capacitive load

The simulation in load changes from capacitive load to a resistive load and load is shown in Figure 4.27. The source current waveform is given to be in sinusoidal shape throughout the simulation time and the transition point, indicating the mitigation capabilities for the proposed algorithm where the source current value around 12 A and the response time taken to maintain the shape is around 0.01s. As the figure depicts, the EFANF can also cater to the changes induced within the simulation time of 0.1s. For the low time show that the algorithm is having a high response rate.

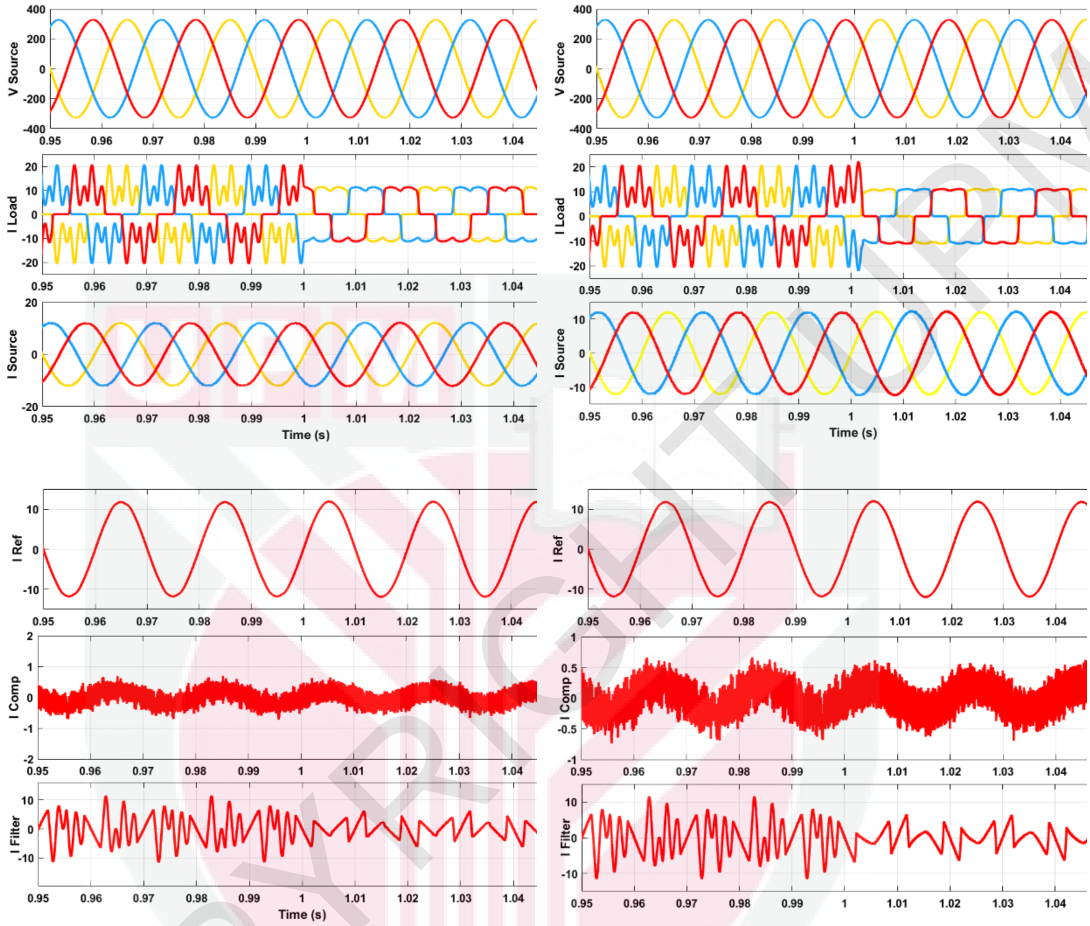

(a) (b)

Figure 4.27: Simulation results of source voltage, load current, source current, reference signal, compensation signal, and filter current for load changes from (a) capacitive to resistive load, (b) capacitive to inductive load

Figure 4.28 represents the simulation results for changes of loads from inductive loads to resistive and capacitive loads. Based on the figure, from the current source waveform, the current source maintains the sinusoidal shape after changes in load at the point of 1.0 s. The current source values around 12 A where the surge due to the changes is 22 A. However, the current source maintains the waveform due to changes within 0.01s. Based on the results, the proposed algorithm has excellent capabilities in mitigating the mentioned types of load change.

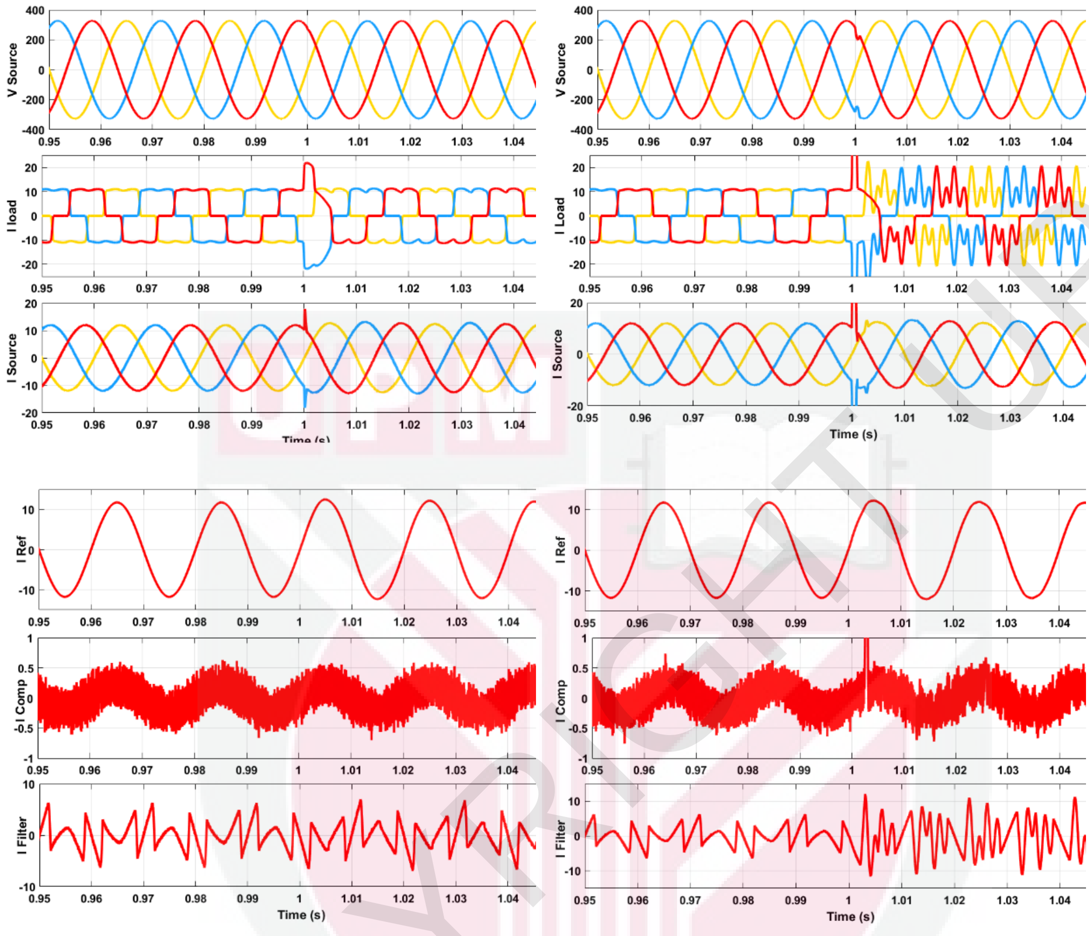

(a) (b)

Figure 4.28: Simulation results of source voltage, load current, source current under, reference signal, compensation signal, and filter current for loas changes from (a) inductive to resistive load, (b) inductive to capacitive load.

The load changes from inductive to resistive load and capacitive load are also shown in Figure 4.28 (a) and (b). The change occurrences are also set at the point of 1s for both types of dynamic load. The figure shows that throughout the simulation, the source current is well mitigated into a sinusoidal waveform compared to the load current waveform, which represents the waveform without mitigation. This condition shows the EFANF can mitigate harmonics through dynamic requirements for all load types.

4.2.4 Transient State Experimental Verification.

The SAPF with the proposed EFANF algorithm is also tested in the experimental setup for transient state conditions for two types of dynamic states. The initial dynamic state tests the response of the involved waveforms based on the changes in values for the same type of load. The second dynamic state test verifies the respective waveforms towards the differences in load types. The values of the load used are mentioned in Table 4.1.

The result of the transient state for the same load types but changes in the value was done in two conditions. First are the upward values, and second is followed by the downward values. Figure 4.29 shows the result for changes purely resistive load. Figure 4.30 shows the change of inductive loads dynamic result and Figure 4.31 shows the result for of the changes in capacitive loads. In each figure, the waveforms are arranged for the increasing values given in figures (a) and (b), while the decreasing values are in figures (c) and (d). The waveforms consist of the source voltage, source current, load current, and filter current.

The waveforms of the purely resistive load for increasing and decreasing values as shown in Figure 4.29 are analyzed. This figure highlights that the source currents are compensated effectively when applying the proposed EFANF to the SAPF. The change of values results in an increase or decrease of the magnitude of the current without changing the shape of load current waveform where the value of the source current changes from 3A to 5A for increasing value and vice versa for decreasing value R_1 to R_2. During change from R_2 to R_3 the current value changes form 5A and 6A for increasing value and vice versa for decreasing value. The system will take around 20ms to reach the next load-designated amplitude. Nonetheless, the waveforms of the source currents are still capable of maintaining the sinusoidal waveshape after the switching point. Therefore, it can be confirmed that the proposed algorithm can perform harmonic current mitigation in these load conditions.

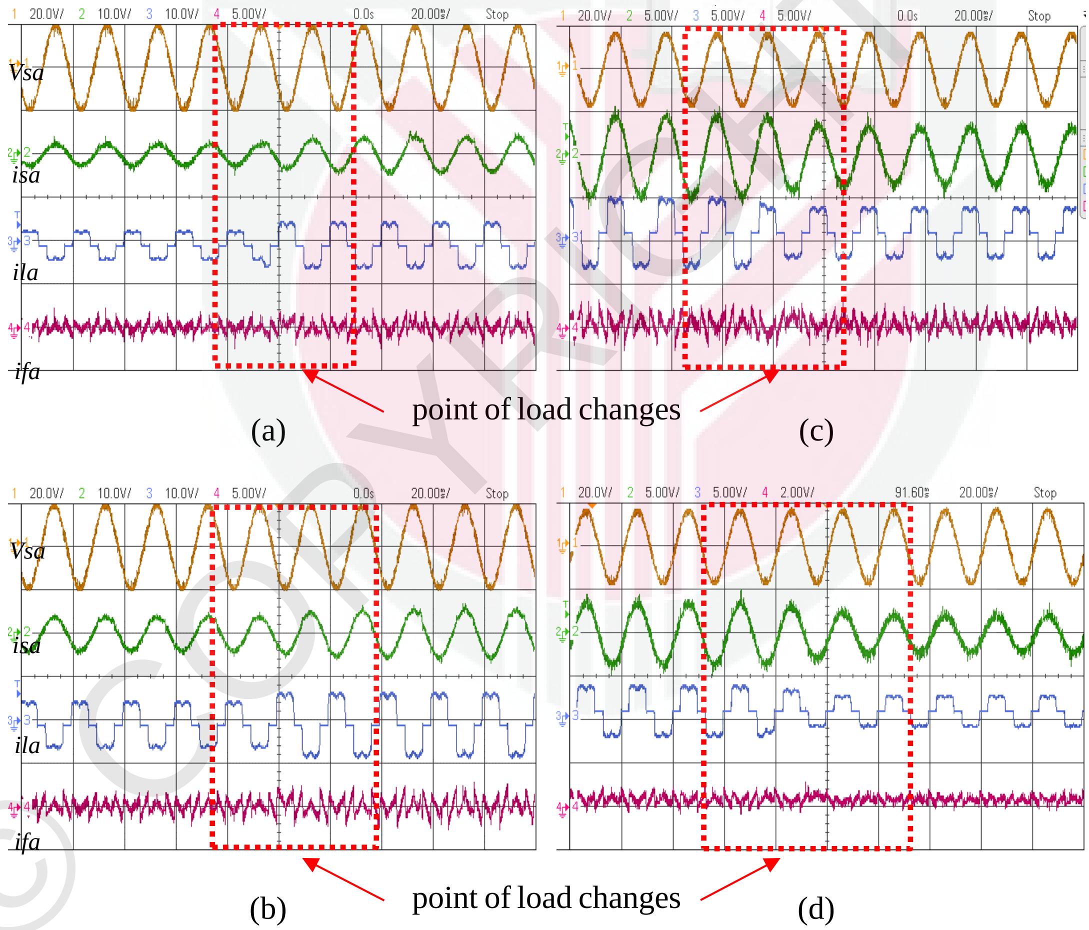

Figure 4.29: Experimental results of transient state for pure resistive loads (a) R_1 to R_2, (b) R_2 to R_3, (c) R_3 to R_2 and (d) R_2 to R_1

Figure 4.30 and Figure 4.31 show the waveforms performed by the SAPF with the proposed algorithm by concentrating more on reactive components of the loads. The changing effects due to change of the load are towards the shape of the load current compared to the amplitude of the load current. The waveform shows that the proposed algorithm works as intended for the inductive load. Figure 4.30 shows the impact on the waveform when the inductive value is changed, where figures (a) and (b) is when the inductor values are increasing, while figures (c) and (d) is when the inductor values are decreasing. During the changes of the reactive load, the source maintains the value within 2. 11A.When the trigger point of changes is activated, the proposed algorithm maintains the shape of source current as a sinusoidal waveform for both dynamic state conditions within 8ms.

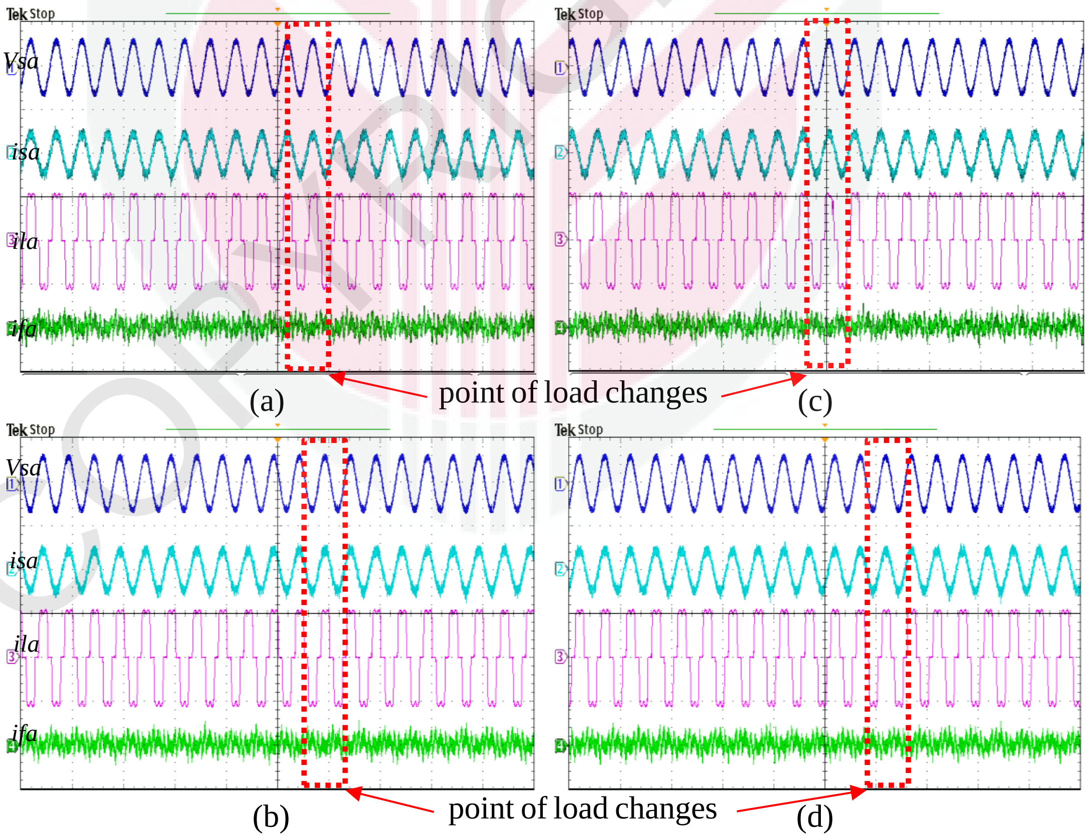

Figure 4.30: Experimental results of transient state of inductive load values. (a) R_1L_1 to R_2L_2, (b) R_2L_2 to R_3L_3, (c) R_3L_3 to R_2L_2 and (d) R_2L_2 to R_1L_1

Analysis from the waveform shows that the proposed algorithm also effectively mitigates capacitive-influenced harmonics. The experimental result shows high variation in the waveform shape for load current within the increasing or decreasing values of the capacitor. During the changes of the capacitor value, the source current stays within the value of 2A. The details of the dynamic state for both increasing and decreasing values of the capacitor are shown in Figure 4.31. The triggering point for the values changes is highlighted in the figure. During the moment of triggering the changes in the capacitive values, the SAPF managed to maintain the waveform of the source current in a sinusoidal shape within 8ms. The maintained waveform supports the capabilities of the proposed algorithm to work efficiently in the dynamic state.

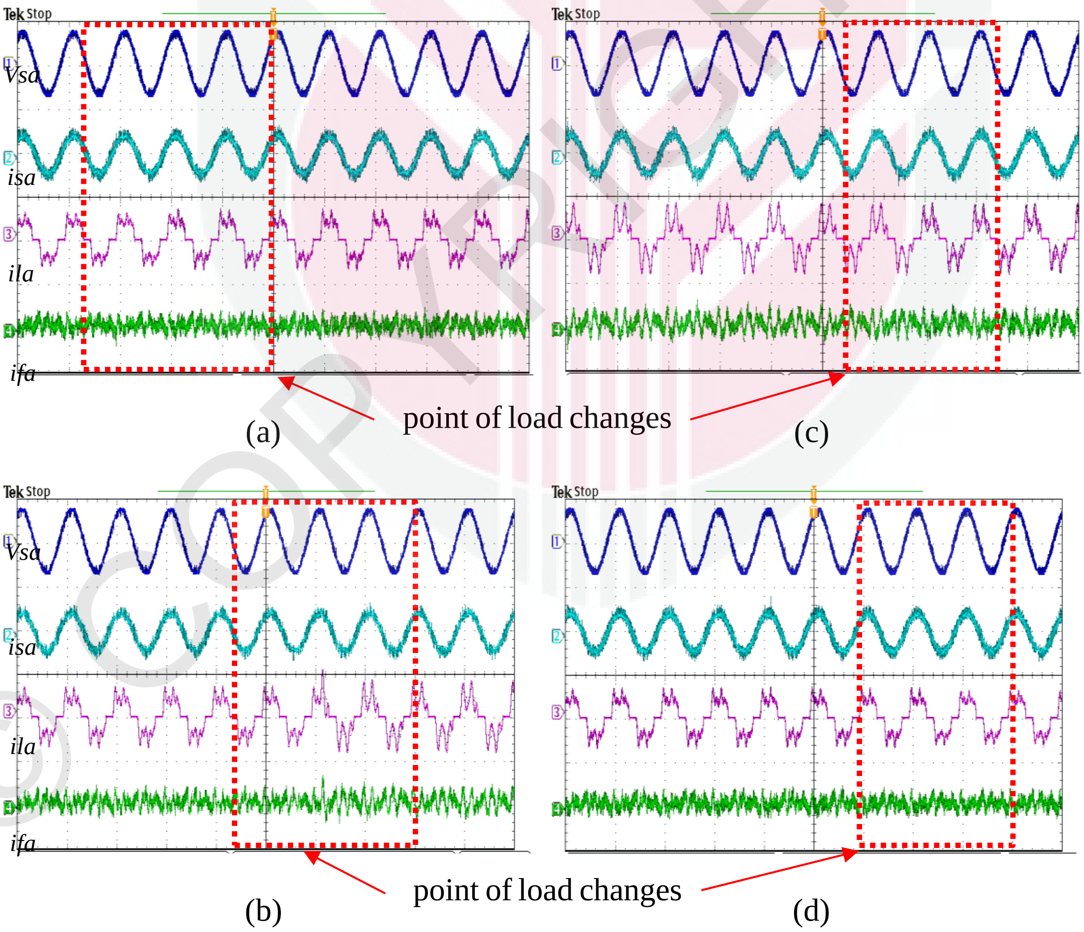

Figure 4.31: Experimental results of transient state for capacitive loads (a) R_1C_1 to R_2C_2, (b) R_2C_2 to R_3C_3, (c) R_3C_3 to R_2C_2 and (d) R_2C_2 to R_1C_1

The algorithm is also tested for changes of load types in dynamic state. The main three load changes that are being tested are pure resistive, inductive, and capacitive.

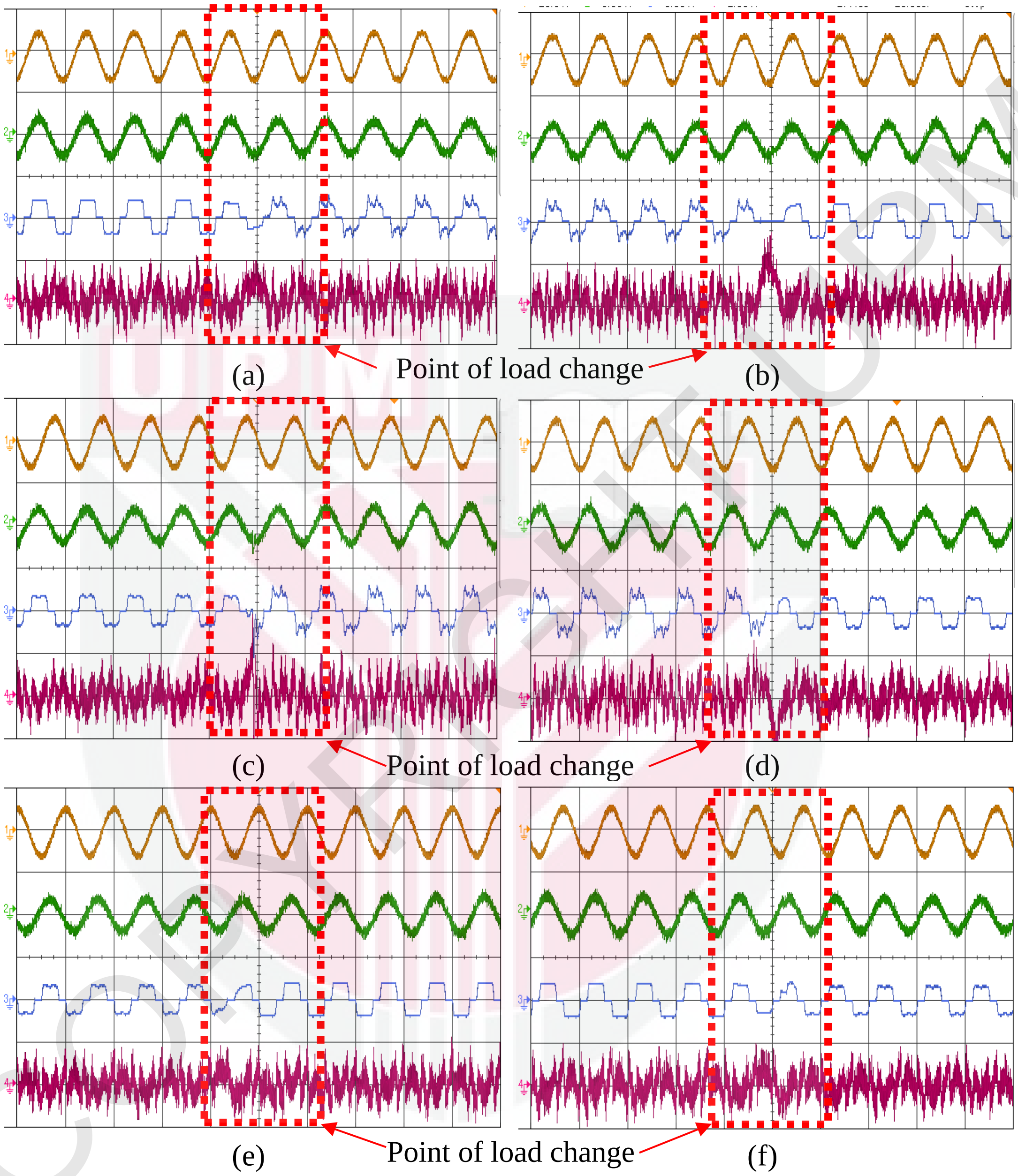

Figure 4.32: Experimental results of transient state for (a) inductive to capacitive load, (b) capacitive to inductive load, (c) resistive to capacitive load, (d) capacitive to resistive load (e) resistive to inductive load (f) inductive to resistive load.

The waveform in Figure 4.32 shows that for all changing load conditions, the proposed algorithm effectively produces the reference current and subsequently mitigates the harmonics induced during the dynamic states. The figure also shows that the mitigation occurs instantaneously with the load changes within 10 ms, where the source current maintained its waveform. It can also be seen that during the changing point of load, the source current can maintain its shape and value where the value of the current source is around 2.11 A. All the changes at the transition point from the experimental works at show that the proposed algorithm is efficient for all the proposed load situations.

4.3 Self-Synchronization for ANF

One of the advantages of the EFANF compared to other harmonics extraction algorithms, as discussed in Chapter 3, is the ANF frequency tracking capability where this eliminates the dependency of the algorithm on PLL for phases synchronization which reduces overall complexity.

4.3.1 Simulation Result of Self-Synchronization

Figure 4.33 shows synchronization between the voltage source for all the phases with reference waveform and filter current. The figure shows that the reference waveform and the filter current have the same zero crossing point for every cycle of the voltage source where in the figures show the crossing point for phase A is at 0.52 and 0.53s, for phase B is at 0.5266s and 0.5367s and for phase C is at 0.5333s and 0.5434s for both source and filter current crossing points.

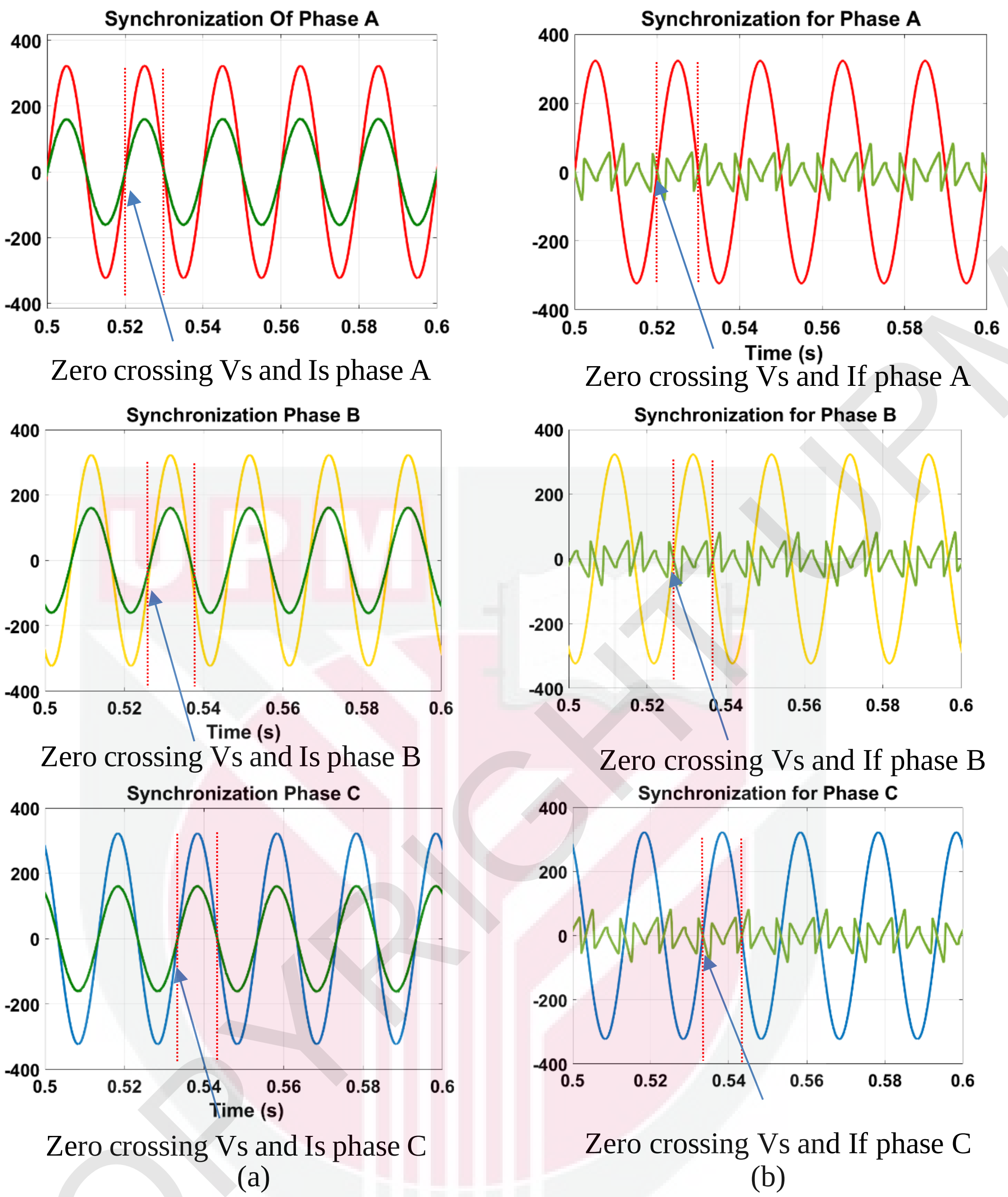

Figure 4.33: Simulation results of self-synchronization by EFANF for (a) reference waveform and (b) filter current.

The consistency of the zero-crossing shows that the frequency tracking capability that the EFANF produces in ensuring the reference signal is fully synchronized with the source signal throughout the simulation time for each individual phase. As the figure highlights, the reference waveform and the filter current waveform start from the same zero crossing point throughout the overall simulation time. Based on this condition, the source voltage, the reference waveform, and the filter current work in phase in the same power system. Hence this validates the synchronization for all the involved waveforms.

4.3.2 Experimental Result of Self-Synchronization

The self-synchronization capability of the proposed algorithm is also tested in the experimental setup to validate its effectiveness practically.

Based on the acquired result, the synchronization process is explored in terms of relationship of the source voltage with the source current and the filter current. The experimental result in Figure 4.34 validates the experimental results for synchronizing the algorithm with the power system. Based on Figure 4.34, the self-synchronization by EFANF can synchronize the source current and filter current with the source voltage for all phases of the system. The waveform in Figure 4.34 (a) shows the synchronization of the source voltage and the source current according to each phase, while Figure 4.34 (b) shows the corresponding source voltage by referring to the filter current according to each phase too.

Both figures show that same zero crossing point for the source and filter current with source voltage indicate EFANF manages to synchronize the reference and filter current for all, proving the self-tracking capability of the proposed algorithm as proposed

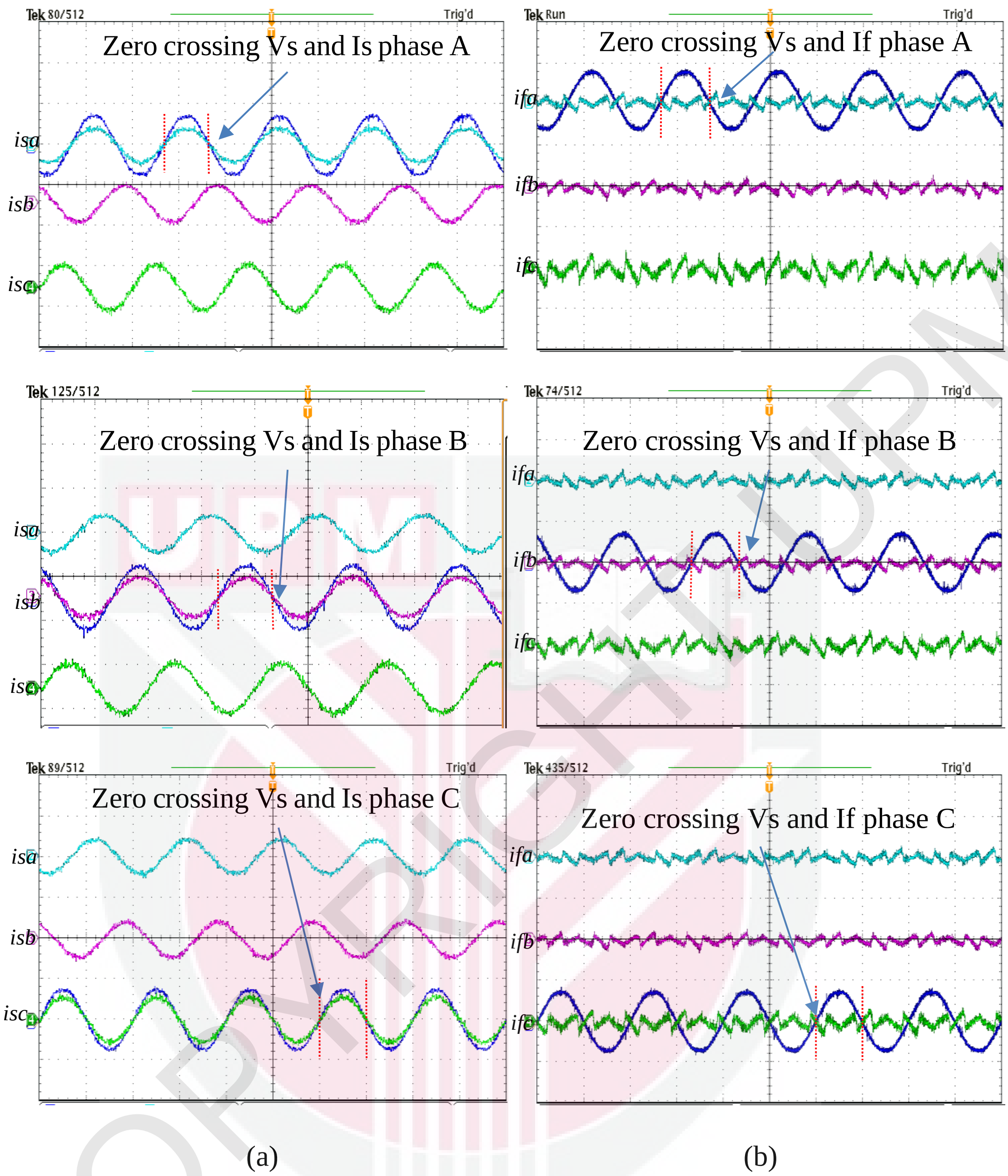

Figure 4.34: Experimental results of self-synchronization by EFANF for (a) reference waveform and (b) filter current.

4.4 DC-Link Voltage Control

One of the major components in the SAPF is the DC-Link. As mentioned in Chapter 3, the DC-Link voltage control for the EFANF is linked with PI PSO-based optimized controller. The PI algorithm is tuned for maximum efficiency by using WBPSO

4.4.1 Simulation Result of WBPSO

The WBPSO-tuned PI is evaluated in two conditions. The first condition is based on the absolute error of DC-Link and the THD, which concludes the outcome based on the final error (FE). Second, the output is concluded by DC-Link and THD based on Sum of Square Error (SSE). The value of the result is reconfirmed for both error considerations.

The suggested PSO criteria are evaluated in the weightage-based error, THD, and DC-Link errors. Figure 4.35 and figure 4.37 display the output of multi-objective PSO for optimizing the fitness output for the PI output based on the Kp and Ki values towards the selected error where each figure presents (a) sum weightage-based error (b) THD and (c) DC-Link error respective for FE error and SSE error during the iteration of the PSO.

Based on the swarm concentration respective to Figure 4.35 (a) and 4.37 (a) sum weightage-based error, the particles are gathered within Kp values around 10 to 20 and Ki values around 70 to 100. During the iteration, the boundary limit for Kp and Ki is set between 0 to 100 for both fitness criteria. Based on the iteration result it is concluded that the best value of PSO for FE are Kp of 23.5759 and Ki of 87.2441. For SSE, the best Kp and Ki gains through the iteration weight based PSO are 96.8723 and 68.7758.

The values of the errors for the respective output based on the iteration point is given in Figure 4.36 and Figure 4.38. Both figures show the iteration points for Weightage-based error, THD error and DC-Link error for FE and SSE, respectively. To compare both, the THD for both FE and SSE are almost in the same trend, where the value for the THD during the iteration is averaging around 0.9 for both FE and SSE. However, for the DC-Link, the SSE is showing a higher trend than FE due to the SSE is catering the error as a whole condition while the FE only considers the final one.

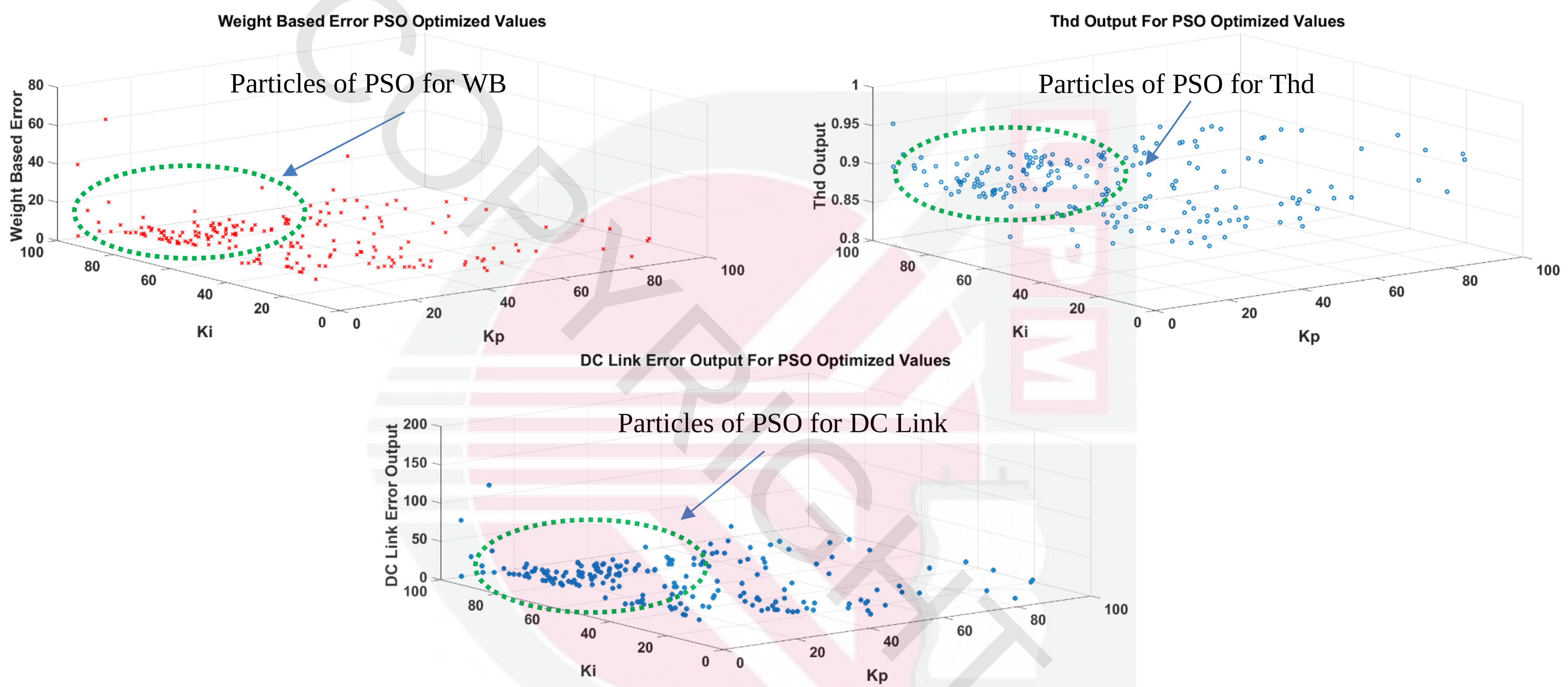

Figure 4.35: (a) Sum weight-based error (b) THD and (c) DC-Link error of PSO for FE corresponding to KP and KI values

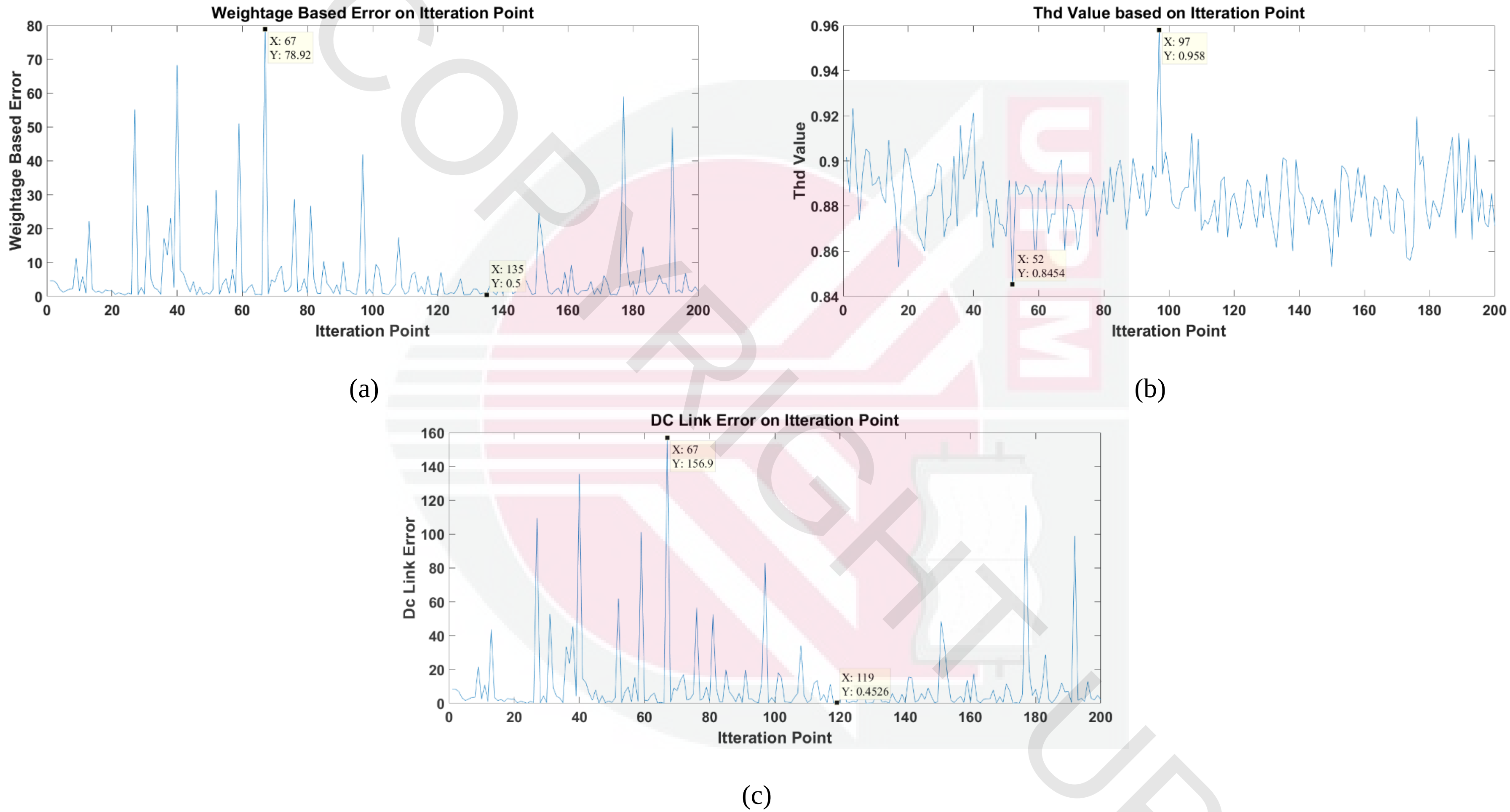

(a)

(b)

(c)

Figure 4.36: (a) Sum weightage-based error (b) THD and (c) DC-Link error of PSO for FE based on iteration point.

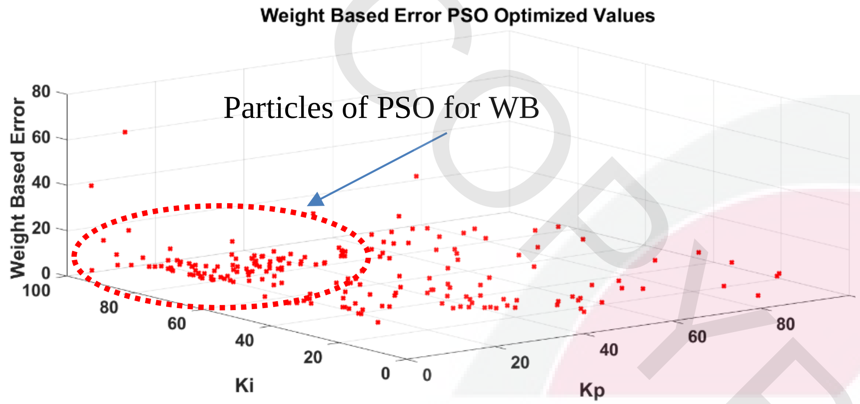

(a)

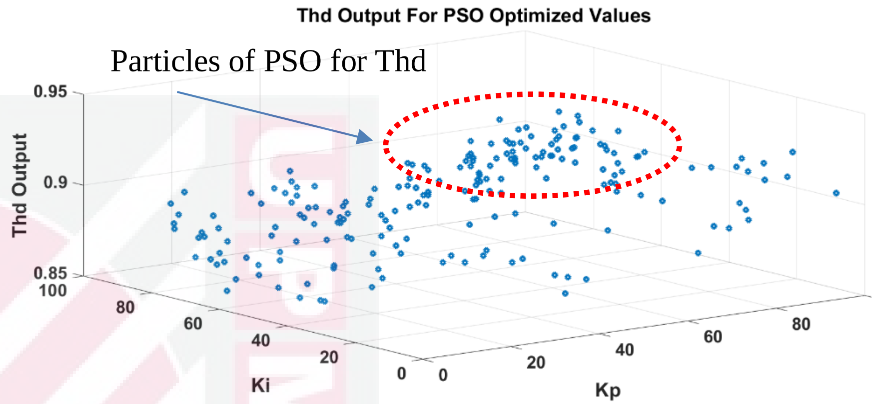

(b)

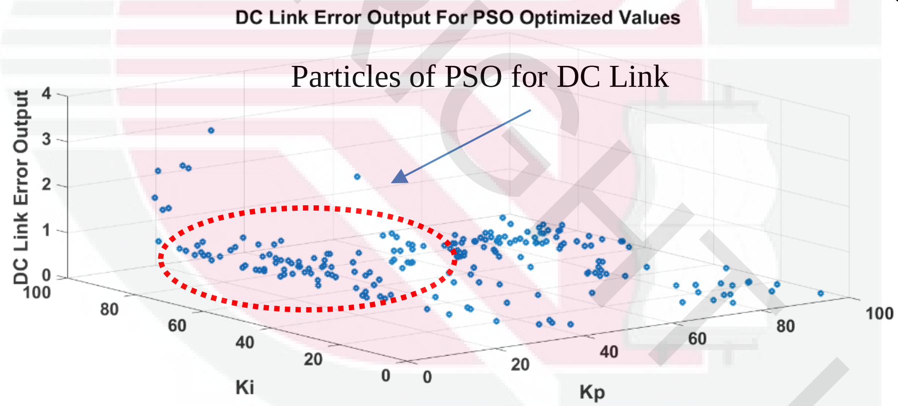

(c)

Figure 4.37: (a) Sum weight-based error (b) THD and (c) DC-Link error of PSO for SSE corresponding to KP and KI values

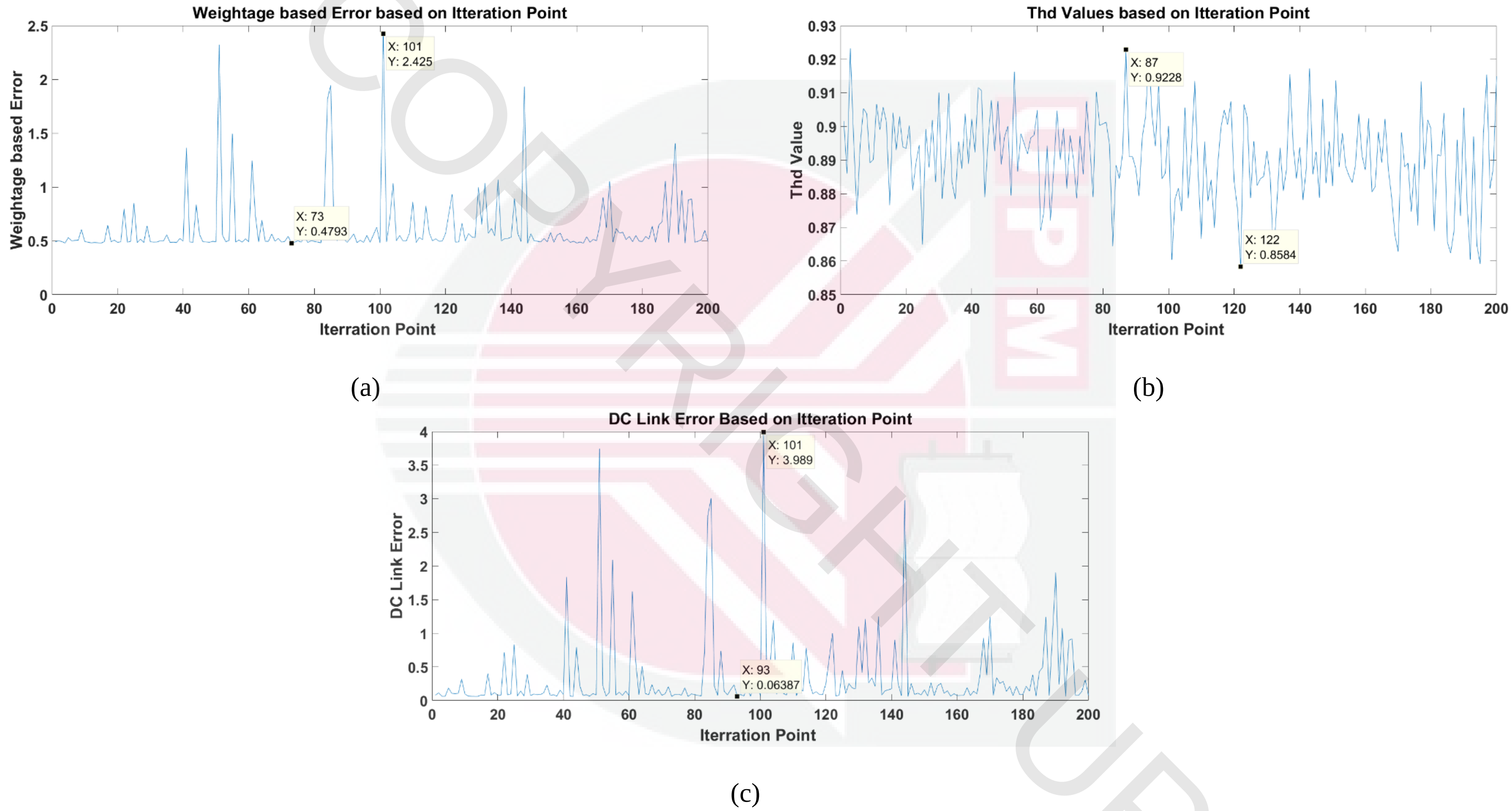

Figure 4.38: (a) Sum weightage-based error (b) THD and (c) DC-Link error of PSO for SSE based on iteration point.

4.4.2 Validation of WBPSO Results

The values obtained through PI weightage based PSO are validated through simulation and experimental works as the PSO iteration generated the best values for Kp and Ki. The outcome is tested for dynamic state based on MATLAB/Simulink and applied within the experimental work. The outputs of the PSO obtained through FE and SSE methods are simulated and compared to each other as shown in Figures 4.39 (a) and 4.40 (a). For transition of the pure resistive load and by using the FE method, it is shown that during the changing point, R_1 to R_2, the overshoot value of the DC-Link voltage is 201.4V, and for R_2 to R_3, the overshoot point is 201.1V. For the SSE method, the overshoots value is 201.3V for R_1 to R_2 and 201.1V for R_2 to R_3, but in terms of settling time, the SSE method produced a better settling time which is 0.368 s and 0.306 s compared to 0.739 s and 0.714 s by FE method.

The Kp and Ki values obtained through PSO for FE and SSE methods were also tested for dynamic state of the inductive and capacitive loads. The results are shown in figures 4.39 (b) and 4.40 (b). It shows that during the transition from R_1L_1 to R_2L_2, the overshoot and settling time values are 201.3V and 0.886 s for FE and 200.7V and 0.595 s for SSE. For transition point of R_2L_2 to R_3L_3, the overshoot and settling time values are 201.1V and 0.836 s for FE, while SSE are 200.4V and 0.218 s.

In terms of capacitive loads, due to change from R_1C_1 to R_2C_2, the overshoot and settling time during this dynamic transition are given as 201.3V and 0.729 s for FE, and meanwhile for SSE, the values acquired are 200.2V and 0.197 s. Another test for dynamic change from R_2C_2 to R_3C_3, the respective voltage overshoot and settling time are given as 201.1V and 0.675 s for FE, and 200.2V and 0.114 s for SSE. Based on the transition results, the value produced through SSE method produced better results than FE method.

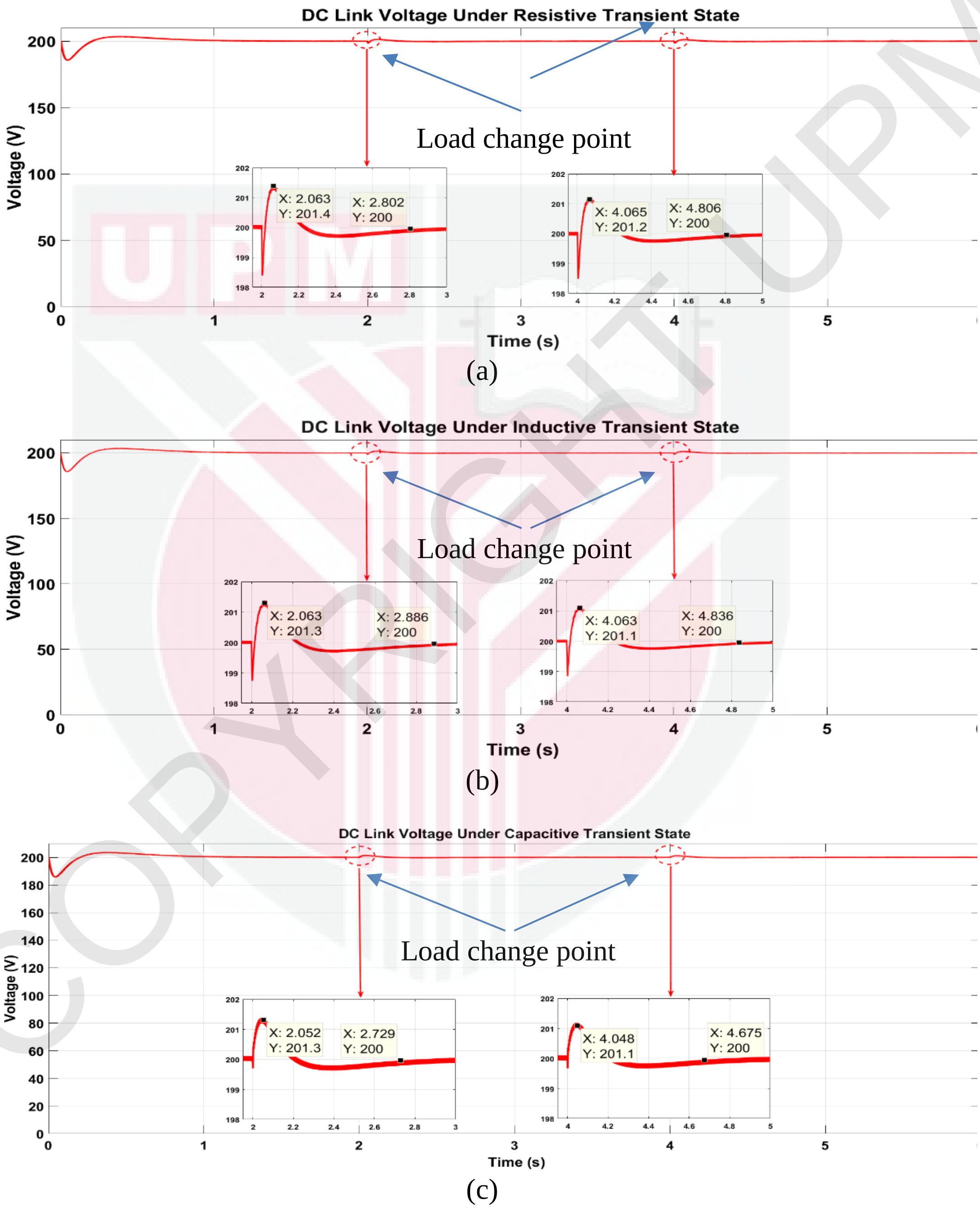

Figure 4.39: Simulation output DC-Link for transient state based on PSO for FE (a) pure resistive loads, (b) inductive loads, and (c) capacitive loads.

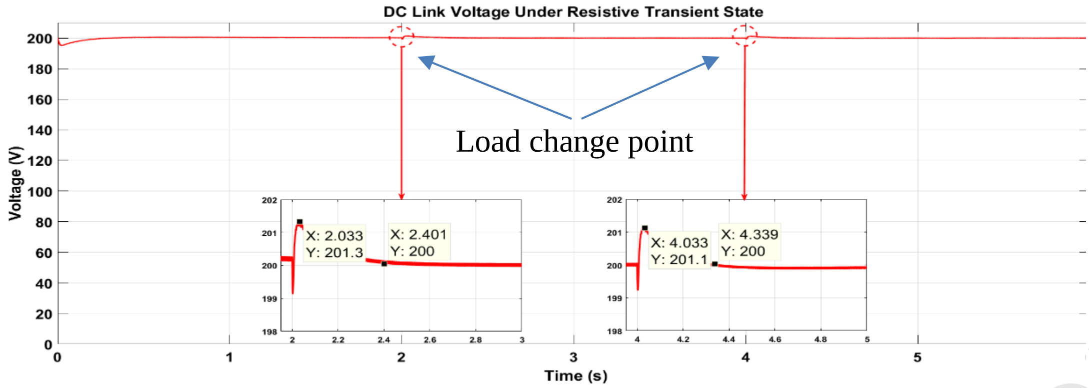

(a)

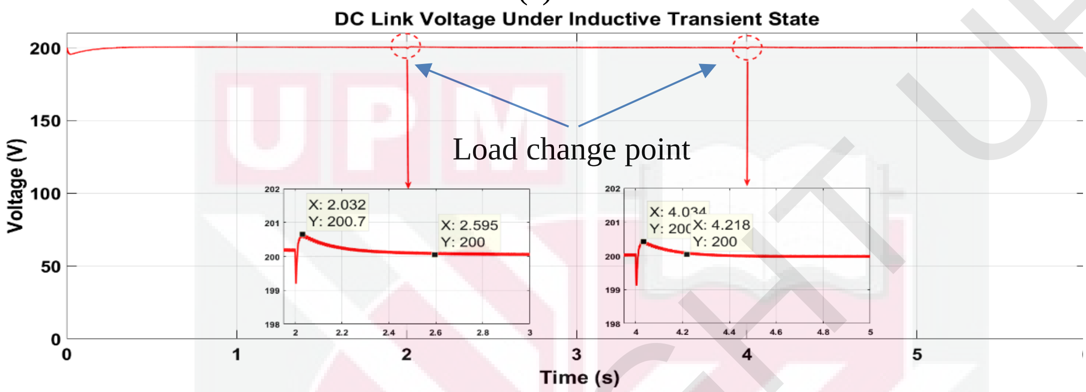

(b)

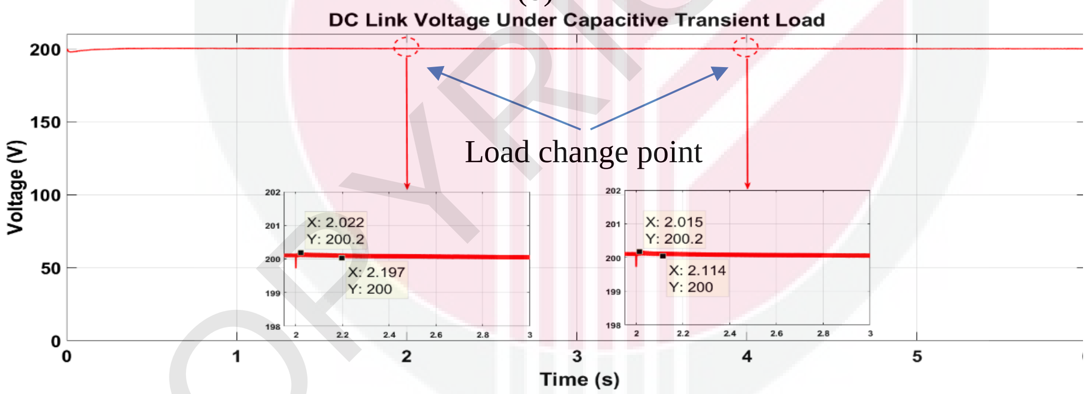

(c)

Figure 4.40: Simulation output of DC-Link for transient state based on PSO for SSE (a) pure resistive, (b) inductive, and (c) capacitive loads.

All the simulation result in related DC-Link capacitor voltage control algorithm for steady state show that the PI with SSE based WBPSO hast the best performance with low undershoot, fast response time to achieve steady state. These performance prove the effectiveness of the proposed controller in DC link capacitor voltage control.

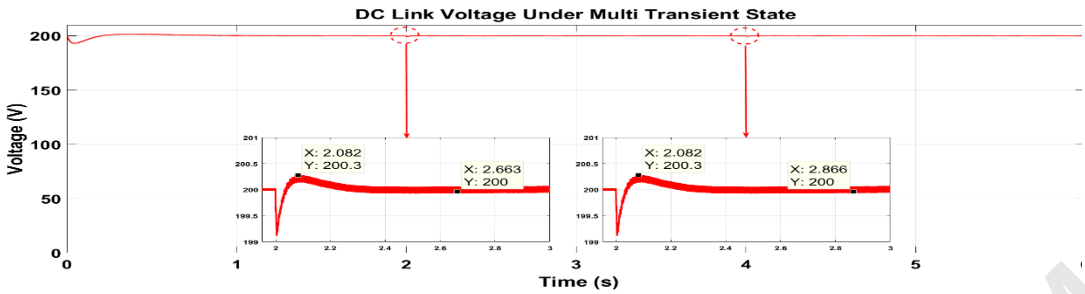

(a)

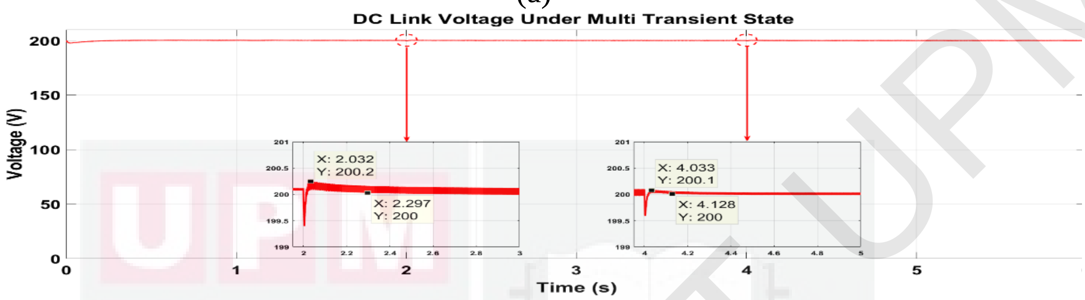

(b)

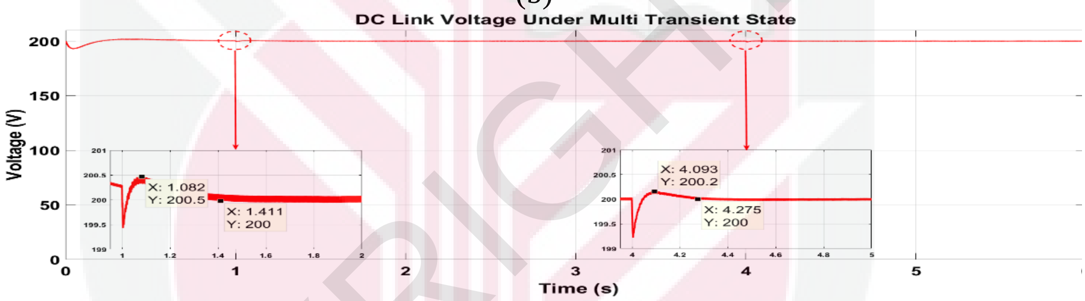

(c)

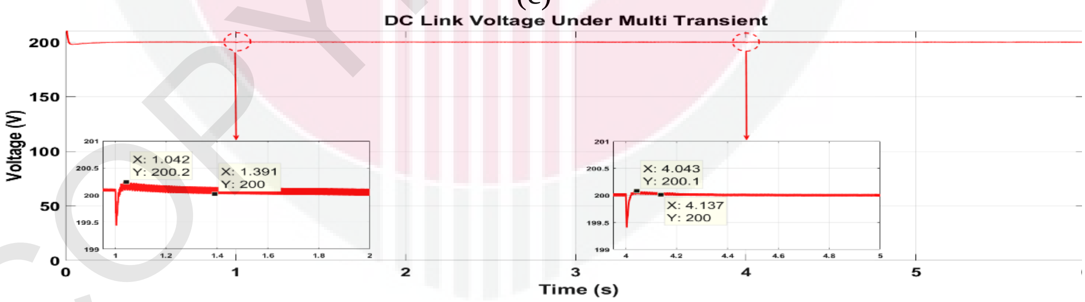

(d)

Figure 4.41: Simulation output of DC-Link for RL to RC and RC to RL under (a) FE and (B) SSE and R to RC and R to RL under (c) FE and (d) SSE

Kp and Ki obtained through WBPSO are further simulated under a multi-load dynamic state to ensure stability of the DC-Link voltage during multi-load changes. The outputs of the DC-Link for RL to RC and RC to RL under FE and SSE-based WBPSO are depicted in Figure 4.41. The figure shows that the SSE yields superior values for overshoot and settling time compared to FE. Specifically, during RL to RC transition, SSE exhibits overshoot and settling time of 200.2V and 0.297 s, while during RC to RL transition, the values are 200.1V and 0.128 s. On the other hand, FE demonstrates the overshoot and settling time of 200.3V and 0.663 s for RL to RC and 200.3V and 0.866 s for RC to RL.

In addition, the figure also illustrates the load transition from R to RC and R to RL. Upon analyzing both load transitions, it is evident that the PI utilizing values from SSE yields superior results in overshoot and settling time when compared to the FE. Specifically, during transition of R to RC, the results indicate overshoot of 200.5V with settling time of 0.411 s for FE, while SSE achieves overshoot of 200.2V with a settling time of 0.391 s. Moreover, for R to RL, FE results in overshoot of 200.2V with settling time of 0.275 s, whereas SSE achieves overshoot of 200.1V with settling time of 0.137 s. Therefore, the simulation results demonstrate that SSE outperforms FE on overshoot and settling times.

The effectiveness of the Kp and Ki values obtained through the SSE is further validated through experimental work to assess the performance of the DC-Link during transient states. Two experimental states were tested. In the first state (Figure 4.42), the resistive, inductive, and capacitive loads underwent changes in terms of values. The figure indicates that the Kp and Ki values obtained through the SSE provide better control over overshoot than those obtained through the FE. Specifically, the SSE achieves an overshoot value of 200.7V, while FE results in an overshoot value of 202.7V for resistive load changes. Regarding the settling time, the SSE shows a better settling time compared to the FE, where the settling time by the SSE is around 0.453s compared to 0.9s taken by the FE.

Similarly, in Figure 4.42 (b) and (c), which represent resistive with inductive and resistive with capacitive loads, respectively, the Kp and Ki values obtained through the SSE demonstrate superior control over the DC-Link voltage throughout all load changes introduced during the experimental work. For example, within the changes of capacitive loads, the DC-Link voltage maintained by the PI optimized by WBPSO based on drop of FE to 199.4V. In contrast, the SSE effectively maintains the DC-Link voltage of 200V. Regarding settling time, the SSE takes around 0.2 s shorter compared to the FE. Same for the inductive load, the overshoot for the SSE is approximately 0.1 V with a settling time of 0.1 s, while the overshoot of the FE is around 0.2 V with settling time of 0.38 s.

Different load types were introduced in the second dynamic state of the experimental work. Figure 4.43 (a) shows the load changes from resistive to resistive with inductive and back to resistive, where for load changes of R_3 to R_3L_3, the DC link voltage for FE method is having an undershoot with the value of 0.8V with settling time of 0.64s while for SSE method the undershoot value is 0.4V with settling time of 0.34 s, which is half of the undershoot value compared to FE method. In terms of load changes from R_3L_3 to R3, both FE and SSE are having overshoots where the overshoot values for FE method is 1.1V with settling time of 0.78s while SSE is having an overshoot of 0.6V with settling time of 0.55s, where the overshoot that produced by the SSE is reduced up to 55% compared to FE.

Figure 4.43 (b) depicts the changes from resistive to resistive with capacitive and back to resistive. For the first change of load between R_3 to R_3C_3, it can seen that for the FE based Kp and Ki value, the FE of experimental result produces an undershoot value of 1.1V with settling time of 0.56s However, for experimental result induced with SSE based Kp and Ki, the undershoot is reduced 54.5% to 0.6V with the settling time of 0.24s. For the next load change from R_3C_3 to R3, the change is causing an overshoot effect for both methods with 3.1V and settling time of 0.815s for the FE, and 1.2V with settling time of 0.3s for the SSE. Both have showing 60% reduction of overshoot values. Lastly, Figure 4.43 (c) illustrates the changes from resistive with inductive to resistive with capacitive and back to resistive with inductive. For R_3L_3 to R_3C_3, the overshoot value is 0.8V for FE and 0.3V for SSE and the settling times for both are 0.68s and 0.37s where in terms of percentage reduction of the value is around 62.5% reduction when compared SSE to FE. For second load changes R_3C_3 to R_3L_3, the DC link is having an undershoot where the value of SSE is 67% of the FE, which is 0.6V compared to 0.9V. In terms of settling time, the settling time of SSE is 0.2645s faster, which is 0.515s compared to FE, which is 0.7795s.

Across all transient conditions, it is evident from the figures that the Kp and Ki values obtained through the SSE provide better control over the DC-Link voltage. Based on these results, it is evident that for transient states, the Kp and Ki values obtained through the SSE offer superior control when compared to the FE in maintaining the DC-Link voltage level and controlling overshoot during load changes. The SSE managed to maintain control in terms of undershoot and overshoot condition during all type of load changes which show the overall capabilities of SSE algorithm.

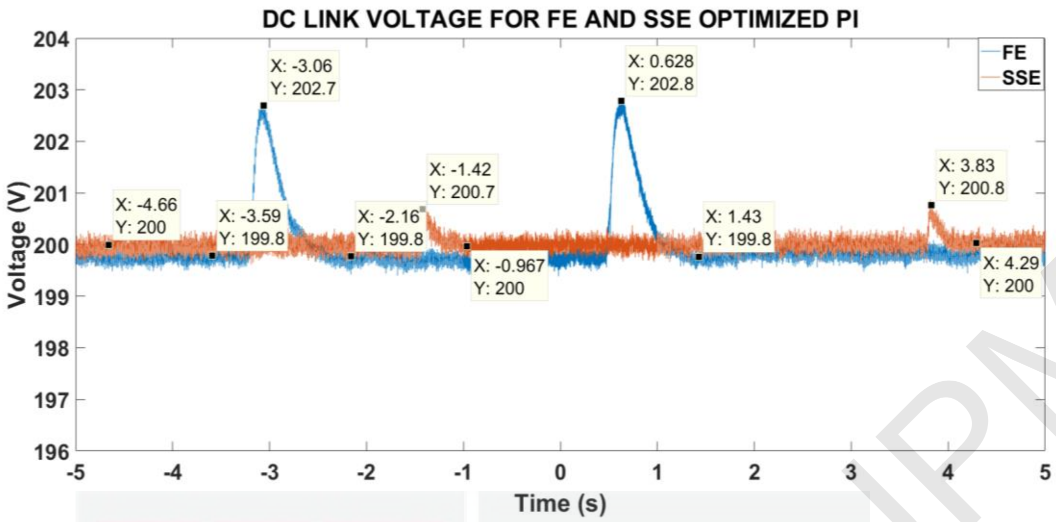

(a)

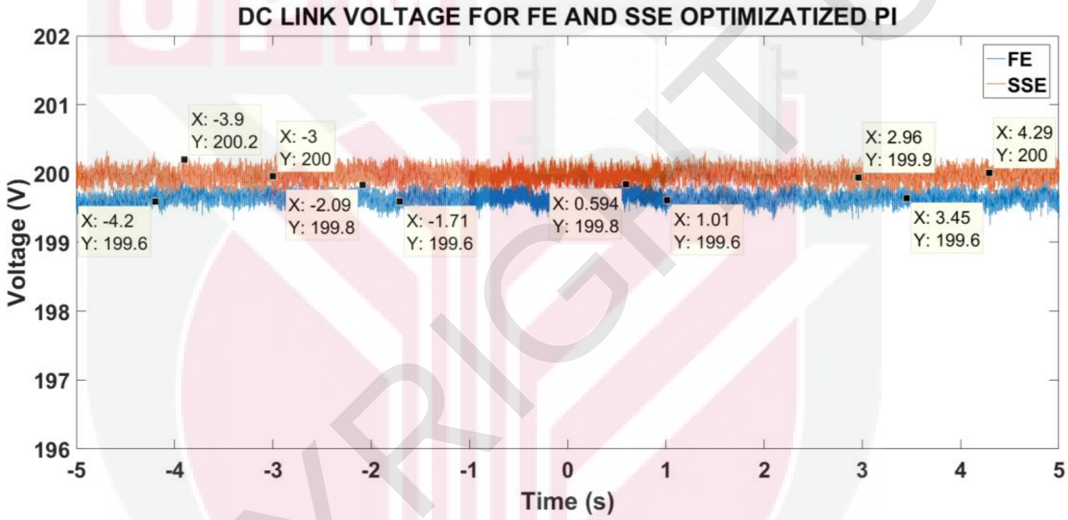

(b)

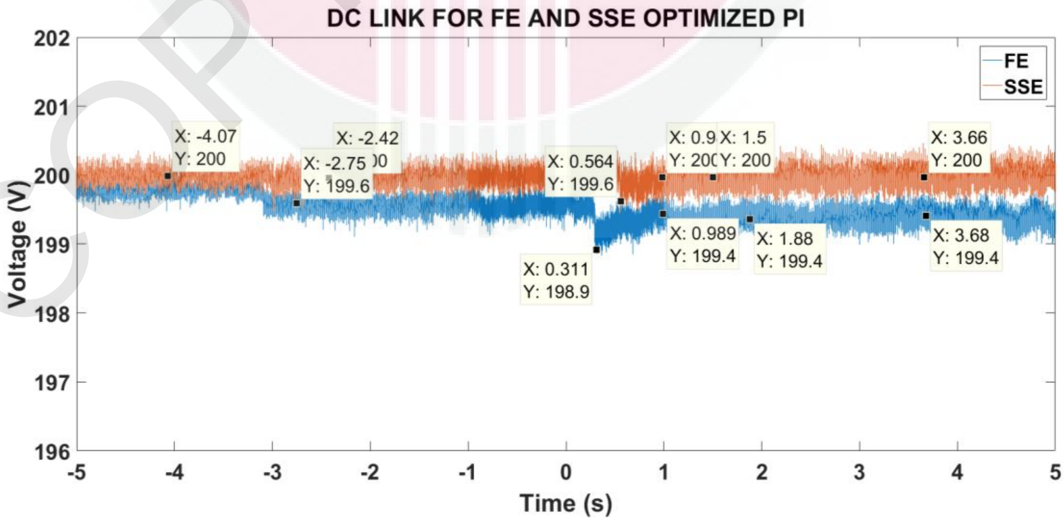

(c)

Figure 4.42: Experimental output of DC-Link for multi transient state (a) R_1 to R_2 and R_3 (b)R_1L_1 to R_2L_2 and R_3L_3 (c) R_1C_1 to R_2C_2 and R_3C_3

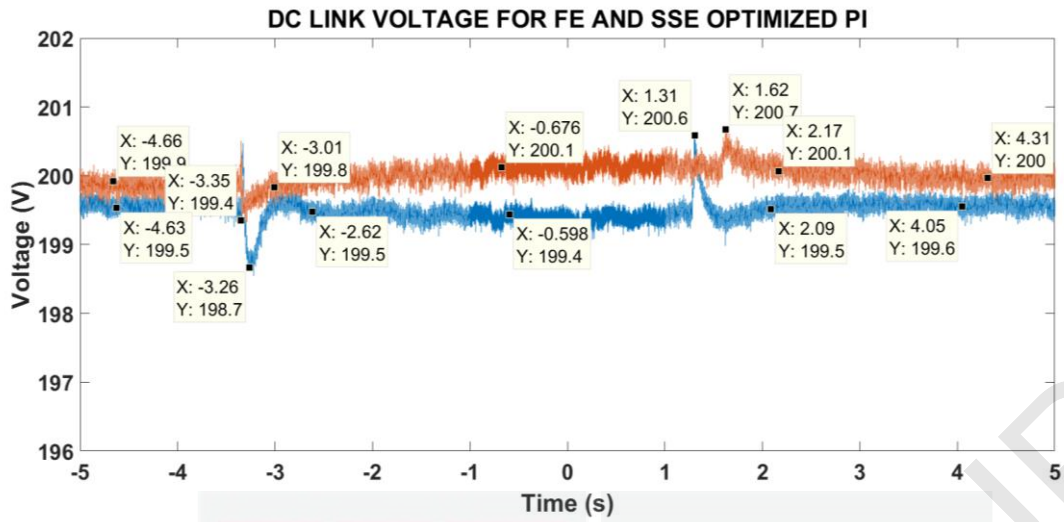

(a)

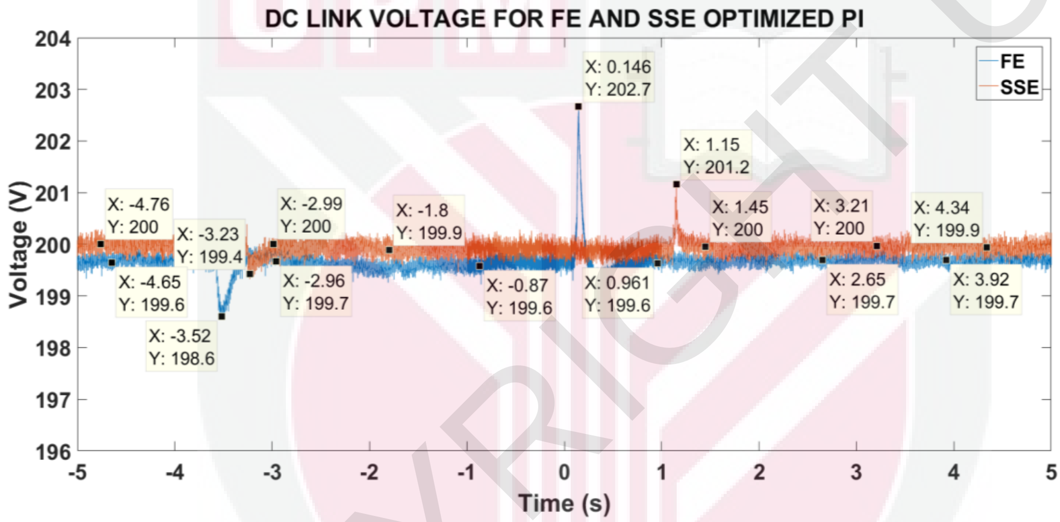

(b)

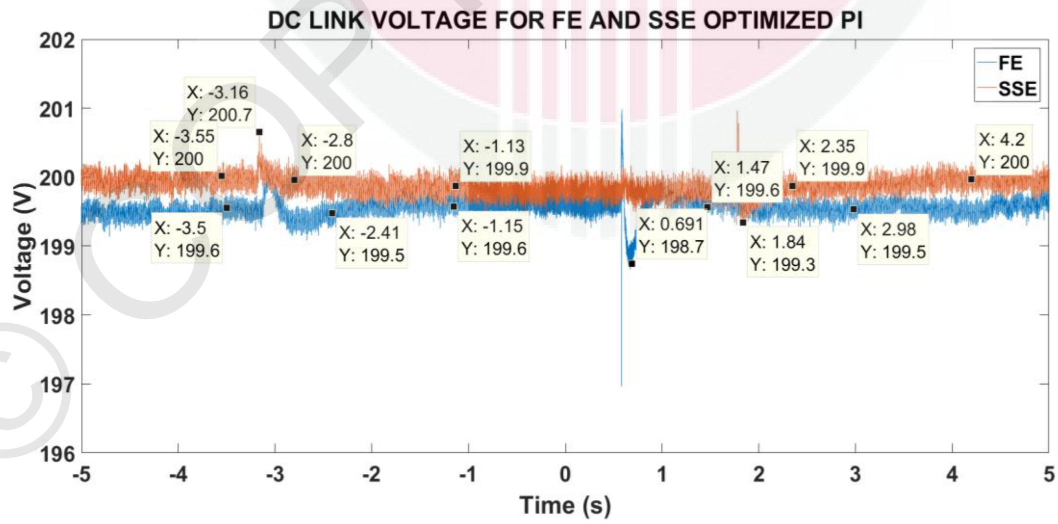

(c)

Figure 4.43: Experimental output of DC-Link for the multi-transient state (a)R_3 to R_3L_3 to R_3 (b) R_3 to R_3C_3 to R_3 (c) R_3L_3 to R_3C_3 to R_3L_3

For overall comparison in terms of overshoot and settling time for load changes based on load type changes is given in Table 4-1 for Kp and Ki based FE WPSO, while table 4-2 show the result of overshoot and settling time for Kp and Ki for SSE based WBPSO. Based on the table, for both result according to the of the load type, Kp and Ki obtained through the SSE based WBPSO produced better overshoot and settling time value for both simulation and experimental result. However, during the changes of load during R1 to R2 and R2 to R3, the overshoot values for the experimental value is higher than simulation value. This is mainly due to the Kp and Ki value FE based WPSO has lower tendencies of reducing overshoot and settling compared to Kp and Ki produced by the SSE based WBPSO.

Table 4.2: Simulation and experimental results for FE

Load Type Change	% Overshoot		Settling Time	
	Simulation	Experimental	Simulation	Experimental
R_1 to R_2	0.7	1.45	0.739	0.900
R_2 to R_3	0.55	1.50	0.714	0.802
R_1L_1 to R_2L_2	0.65	0.10	0.886	0.380
R_2L_2 to R_3L_3	0.55	0.10	0.836	0.416
R_1C_1 TO R_2C_2	0.65	0.10	0.729	0.550
R_2C_2 TO R_3C_3	0.55	0.25	0.675	0.678

Table 4.3: Simulation and experimental result for SSE

Load Type Change	% Overshoot		Settling Time	
	Simulation	Experimental	Simulation	Experimental
R_1 to R_2	0.65	0.35	0.368	0.453
R_2 to R_3	0.55	0.4	0.306	0.460
R_1L_1 to R_2L_2	0.35	0.1	0.595	0.102
R_2L_2 to R_3L_3	0.2	0.05	0.218	0.112
R_1C_1 TO R_2C_2	0.1	0.05	0.197	0.280
R_2C_2 TO R_3C_3	0.1	0.2	0.114	0.205

4.5 Summary

The effectiveness of the proposed algorithms has been verified according to the respective objectives through simulation and experimental works. Throughout both simulation and experimental results, it can be established that both proposed algorithms are capable of operating with the SAPF. The EFANF can produce the required reference current for the SAPF to mitigate the harmonics and perform under low THD values from 2.52% up to 2.99% under various loads. The EFANF also shows self-synchronous capability, as proposed in Chapter 3. In terms of DC-Link control, based on Kp and Ki values obtained through the WBPSO, the DC-Link is confirmed to be able to maintain the reference current through the transient load changes and having low overshoot and settling time, where the overshoot is around 0.345% and settling time around 0.24 s.

CHAPTER 5

CONCLUSION AND FUTURE WORKS

5.1 Conclusion

The design, development, and implementation of advanced algorithms for a three-phase three-wire Shunt Active Power Filter (SAPF) have successfully been achieved. The proposed EFANF algorithm effectively manages harmonics extraction and balanced power control by determining reference currents based on the average value of three-phase instantaneous power and incorporating DC-Link voltage loss into its calculations. This approach eliminates the need for additional synchronization algorithms such as PLL and ZCD, simplifying the overall SAPF system.

Through comprehensive simulation and experimental validation, the EFANF algorithm consistently achieved low Total Harmonic Distortion (THD) values. In steady-state conditions, the algorithm managed to mitigate harmonics with THD values ranging from 1.25% to 2.46% for resistive loads, 1.25% to 1.91% for inductive loads, and 1.91% to 2.54% for capacitive loads. Comparatively, the proposed algorithm outperformed other extraction algorithms like PQLP, PQANF, and Fryze in harmonic mitigation. In dynamic states, the algorithm successfully maintained the sinusoidal shape of the source current below 0.01s for all load types, demonstrating its effectiveness in dynamic conditions.

The PI controller, optimized using Weighted Binary Particle Swarm Optimization (WBPSO), demonstrated superior performance in controlling the DC-Link voltage.

Two optimization conditions were considered which are Final Error (FE) and Sum of Squared Errors (SSE). The SSE-based WBPSO outperformed the FE-based WBPSO, particularly in terms of overshoot and settling time where the overshoot value for SSE based WBPSO is between 0.1% to 0.65% compared to FE based WBPSO which lies between 0.55 to 0.7%. The optimized Kp and Ki values were validated during dynamic operations, showing effective control of DC-Link voltage stability and improved performance during load changes.

Experimental validation further confirmed the robustness of the proposed algorithms. In steady-state tests, the EFANF algorithm achieved THD values of 3.46% for resistive loads, 2.63% for inductive loads, and 2.52% for capacitive loads. In dynamic states, the algorithm maintained the sinusoidal shape of the source current within 0.01s of operation, illustrating its quick response capability. The optimized PI controller using SSE-based WBPSO showed superior performance in terms of overshoot and settling time compared to the FE-based approach during load changes where for overshoot SSE the 0.2% to 0.35% better compared to FE which ranging 0.25% to 1.50%. While in terms of settling time for SSE ranging from 0. 205s to 0.460s exceeds the FE which ranging from 0.678s to 0.900s.

These findings establish the EFANF and WBPSO-optimized PI controller as robust and efficient solutions for SAPF operations, capable of delivering low harmonics and stable voltage control under diverse operating conditions. Consequently, the developed methodologies present significant advancements in power quality improvement and pave the way for future research and practical implementations in the field of active power filters.

5.2 Contribution of Works

The development of three-phase SAPF with EFANF for extraction algorithm and optimized PI controller based on WBPSO for DC-Link voltage control, has been presented for both simulation and experimental works. The significant contributions of this work are as follows.

1) EFANF Algorithm Development: The successful development and implementation of the EFANF algorithm for harmonics extraction and balanced power control in a three-phase three-wire SAPF. The algorithm effectively extracts harmonics and contributes to power balance within the capacitor, leading to improved power quality.

2) Complexity Reduction: The simplification of the control system complexity within the SAPF by eliminating the need for conventional synchronization algorithms with EFANF. This streamlines the operation of the system and improves overall efficiency.

3) WBPSO Optimization: The utilization of Weightage-Based Particle Swarm Optimization (WBPSO) for optimizing Proportional-Integral (PI) controllers in conjunction with EFANF. This optimization technique enhances DC-Link voltage control and harmonics mitigation, demonstrating improved performance compared to traditional tuning methods.

4) SAPF Performance Evaluation: The assessment of EFANF and optimized PI controllers through simulations and experimental works to evaluate their performance in reducing Total Harmonic Distortion (THD) caused by non-linear

loads and ensuring DC-Link voltage stability. The results indicate the effectiveness of the algorithms in enhancing power quality and system stability.

5.3 Future Works

Based on the findings of this research, the following future works are proposed:

1) The proposed algorithms can be considered for other topologies of SAPF, such as a three-phase three-wire SAPF using a two-leg (modified) VSI topology and a three-phase four-wire SAPF using either three-leg or four-leg VSI topology.

2) Auto-tuning method for the ANF coefficients can be established, as those coefficients significantly affect accuracy and convergence speed of the algorithm.

3) The proposed algorithm can be integrated with other control techniques, such as SPWM or SVPWM, to assess its effectiveness in mitigation of harmonics.

In conclusion, this research has successfully presented a well-designed algorithm for three-phase SAPF, by demonstrating its effectiveness through comprehensive simulation and experimental tests. The proposed extraction algorithm and the optimized PI controller based on WBPSO offer promising solutions for SAPF, providing low harmonics and stable DC-Link voltage control.

REFERENCES

[1] J. S. Subjak and J. S. Mcquilkin, "Harmonies—Causes, Effects, Measurements, and Analysis: An Update," *IEEE Trans. Ind. Appl.*, vol. 26, no. 6, pp. 1034–1042, 1990.

[2] T. M. T. Thentral, R. Palanisamy, S. Usha, M. Bajaj, H. M. Zawbaa, and S. Kamel, "Analysis of Power Quality issues of different types of household applications," *Energy Reports*, vol. 8, pp. 5370–5386, 2022.

[3] R. Kaushik, O. P. Mahela, P. K. Bhatt, B. Khan, S. Padmanabhan, and F. Blaabjerg, "A Hybrid Algorithm for Recognition of Power Quality Disturbances," *IEEE Access*, vol. 8, 2020.

[4] A. Kouchaki and M. Nymand, "Analytical Design of Passive LCL Filter for Three-Phase Two-Level Power Factor Correction Rectifiers," *IEEE Trans. Power Electron.*, vol. 33, no. 4, pp. 3012–3022, 2018.

[5] R. N. Beres, X. Wang, M. Liserre, F. Blaabjerg, and C. L. Bak, "A Review of Passive Power Filters for Three-Phase Grid-Connected Voltage-Source Converters," *IEEE J. Emerg. Sel. Top. Power Electron.*, vol. 4, no. 1, pp. 54–69, 2016.

[6] S. R. Das *et al.*, "A comprehensive survey on different control strategies and applications of active power filters for power quality improvement," *Energies*, vol. 14, no. 15, 2021.

[7] J. Gong, D. Li, T. Wang, W. Pan, and X. Ding, "A comprehensive review of improving power quality using active power filters," *Electr. Power Syst. Res.*, vol. 199, no. October 2020, p. 107389, 2021.

[8] Y. Pal, A. Swarup, and B. Singh, "Flexible control of UPQC for selective compensation of power quality problems," *India Int. Conf. Power Electron. IICPE 2010*, pp. 1–8, 2011.

[9] G. B. Ezhiljenekkha and M. Marsalinebeno, "Review of Power Quality Issues in Solar and Wind Energy," *Mater. Today Proc.*, vol. 24, no. July 2009, pp. 2137–2143, 2019.

[10] P. A. Regalia, "An improved lattice-based adaptive IIR notch filter," *IEEE Trans. Signal Process.*, vol. 39, no. 9, pp. 2124–2128, 1991.

[11] M. Mojiri and A. R. Bakhshai, "Stability analysis of periodic orbit of an adaptive notch filter for frequency estimation of a periodic signal," *Automatica*, vol. 43, no. 3, pp. 450–455, 2007.

[12] D. Yazdani, A. Bakhshai, and P. K. Jain, "A Three-Phase Adaptive Notch Filter-Based Approach to Harmonic/Reactive Current Extraction and Harmonic

Decomposition," *IEEE Trans. Power Electron.*, vol. 25, no. 4, pp. 914–923, Apr. 2010.

[13] M. Mojiri, M. Karimi-Ghartemani, and A. Bakhshai, "Processing of harmonics and interharmonics using an adaptive notch filter," *IEEE Trans. Power Deliv.*, vol. 25, no. 2, pp. 534–542, 2010.

[14] M. H. Same, G. Gleeton, G. Gandubert, P. Ivanov, and R. J. Landry, "Multiple narrowband interferences characterization, detection and mitigation using simplified welch algorithm and notch filtering," *Appl. Sci.*, vol. 11, no. 3, pp. 1–26, 2021.

[15] Liu Hsu, R. Ortega, and G. Damm, "A globally convergent frequency estimator," *IEEE Trans. Automat. Contr.*, vol. 44, no. 4, pp. 698–713, Apr. 1999.

[16] M. Mojiri and A. R. Bakhshai, "An Adaptive Notch Filter for Frequency Estimation of a Periodic Signal," *IEEE Trans. Automat. Contr.*, vol. 49, no. 2, pp. 314–318, Feb. 2004.

[17] M. Farhadi-Kangarlu, E. Babaei, and F. Blaabjerg, "A comprehensive review of dynamic voltage restorers," *Int. J. Electr. Power Energy Syst.*, vol. 92, pp. 136–155, 2017.

[18] U. Kumar and S. Kumar, "DC-Link Voltage Balancing with Fuzzy Logic Controller for Shunt Active Power Filter of More Electrical Aircraft," *Proc. 2020 IEEE 1st Int. Conf. Smart Technol. Power, Energy Control. STPEC 2020*, 2020.

[19] J. Zhou, Y. Yuan, and H. Dong, "Adaptive DC-Link Voltage Control for Shunt Active Power Filters Based on Model Predictive Control," *IEEE Access*, vol. 8, pp. 208348–208357, 2020.

[20] H. A. Ismail, A. Alenany, and B. Abozalam, "Improved dc-link voltage controller for photo voltaic on-grid systems," *Indones. J. Electr. Eng. Informatics*, vol. 9, no. 2, pp. 442–452, 2021.

[21] A. K. Mishra, S. R. Das, P. K. Ray, R. K. Mallick, A. Mohanty, and D. K. Mishra, "PSO-GWO Optimized Fractional Order PID Based Hybrid Shunt Active Power Filter for Power Quality Improvements," *IEEE Access*, vol. 8, pp. 74497–74512, 2020.

[22] C. Lascu, L. Asiminoaei, I. Boldea, and F. Blaabjerg, "High performance current controller for selective harmonic compensation in active power filters," *IEEE Trans. Power Electron.*, vol. 22, no. 5, pp. 1826–1835, 2007.

[23] M. Haddad, S. Ktata, S. Rahmani, and K. Al-Haddad, "Real time simulation and experimental validation of active power filter operation and control," *Math. Comput. Simul.*, vol. 130, pp. 212–222, 2016.

[24] Y. Wang, J. Yong, Y. Sun, W. Xu, and D. Wong, "Characteristics of Harmonic Distortions in Residential Distribution Systems," *IEEE Trans. Power Deliv.*, vol. 32, no. 3, pp. 1495–1504, 2017.

[25] K. M. Nor, "Power Quality Awareness Program," *st.gov.my https://www.st.gov.my/en/contents/presentations/PQ_2015/01PQ%20Baseline%20Study_Prof%20Khalid.pdf*, 2012. .

[26] J. Barros and R. I. Diego, "A review of measurement and analysis of electric power quality on shipboard power system networks," *Renew. Sustain. Energy Rev.*, vol. 62, pp. 665–672, 2016.

[27] A. Nassif, "Assessing the Impact of Harmonics and Interharmonics of Top and Mudpump Variable Frequency Drives in Drilling Rigs," *IEEE Trans. Ind. Appl.*, vol. 55, no. 1, pp. 1–1, 2019.

[28] C. Tu *et al.*, "Dynamic Voltage Restorer With an Improved Strategy to Voltage Sag Compensation and Energy Self-Recovery," *CPSS Trans. Power Electron. Appl.*, vol. 4, no. 3, pp. 219–229, Sep. 2019.

[29] R. N. Liao and N. C. Yang, "Evaluation of voltage imbalance on lowvoltage distribution networks considering delta-connected distribution transformers with a symmetrical NGS," *IET Gener. Transm. Distrib.*, vol. 12, no. 7, pp. 1644–1654, 2018.

[30] T. Routtenberg, R. Concepcion, and L. Tong, "PMU-Based Detection of Voltage Imbalances with Tolerance Constraints," *IEEE Trans. Power Deliv.*, vol. 32, no. 1, pp. 484–494, 2017.

[31] M. R. Alam, K. M. Muttaqi, and A. Bouzerdoum, "Characterizing Voltage Sags and Swells Using Three-Phase Voltage Ellipse Parameters," *IEEE Trans. Ind. Appl.*, vol. 51, no. 4, pp. 2780–2790, 2015.

[32] A. A. Alkahtani *et al.*, "Power Quality in Microgrids including Supraharmonics: Issues, Standards, and Mitigations," *IEEE Access*, vol. 8, pp. 127104–127122, 2020.

[33] P. Thakur, "Load Distribution and VFD Topology Selection for Harmonic Mitigation in an Optimal Way," *IEEE Trans. Ind. Appl.*, vol. 56, no. 1, pp. 48–56, 2020.

[34] W. Song, J. Fang, Z. Jiang, M. Staines, and R. Badcock, "AC Loss Effect of High-Order Harmonic Currents in a Single-Phase 6.5 MVA HTS Traction Transformer," *IEEE Trans. Appl. Supercond.*, vol. 29, no. 5, pp. 1–5, 2019.

[35] R. V. Sabariego and J. Gyselinck, "Eddy-Current-Effect Homogenization of Windings in Harmonic-Balance Finite-Element Models," *IEEE Trans. Magn.*, vol. 53, no. 6, pp. 1–4, 2017.

[36] K. Wang, "Effects of harmonics into magnet shape and current of dual three-phase permanent magnet machine on output torque capability," *IEEE Trans. Ind. Electron.*, vol. 65, no. 11, pp. 8758–8767, 2018.

[37] L. Moran, C. A. Albistur, and R. Burgos, "Multimega VAR Passive Filters for Mining Applications: Practical Limitations and Technical Considerations," *IEEE Trans. Ind. Appl.*, vol. 52, no. 6, pp. 5310–5317, 2016.

[38] Y. W. Liu, S. H. Rau, C. J. Wu, and W. J. Lee, "Improvement of Power Quality by Using Advanced Reactive Power Compensation," *IEEE Trans. Ind. Appl.*, vol. 54, no. 1, pp. 18–24, 2018.

[39] M. A. Fard, A. J. Reid, and D. M. Hepburn, "Analysis of HVDC superimposed harmonic voltage effects on partial discharge behavior in solid dielectric media," *IEEE Trans. Dielectr. Electr. Insul.*, vol. 24, no. 1, pp. 7–16, 2017.

[40] L. Merabet, S. Saad, D. O. Abdeslam, and J. Merckle, "Direct neural method for harmonic currents estimation using adaptive linear element," *Electr. Power Syst. Res.*, vol. 152, pp. 61–70, 2017.

[41] X. Wei, C. Li, M. Qi, B. Luo, X. Deng, and G. Zhu, "Research on harmonic current amplification effect of parallel APF compensating voltage source nonlinear load," *Energies*, vol. 12, no. 16, 2019.

[42] W. Liang, W. Fei, and P. C. K. Luk, "An Improved Sideband Current Harmonic Model of Interior PMSM Drive by Considering Magnetic Saturation and Cross-Coupling Effects," *IEEE Trans. Ind. Electron.*, vol. 63, no. 7, pp. 4097–4104, 2016.

[43] J. Li, Q. Yang, Y. Li, C. Zhang, and B. Qu, "Measurement and Modeling of 3-D Rotating Anomalous Loss Considering Harmonics and Skin Effect of Soft Magnetic Materials," *IEEE Trans. Magn.*, vol. 53, no. 6, pp. 1–4, 2017.

[44] D. Committee, I. Power, and E. Society, *IEEE 519 Recommended Practice and Requirements for Harmonic Control in Electric Power Systems IEEE Power and Energy Society*, vol. 2014. 2014.

[45] B. A. Angélico, L. B. G. Campanhol, and S. A. Oliveira da Silva, "Proportional–integral/proportional–integral-derivative tuning procedure of a single-phase shunt active power filter using Bode diagram," *IET Power Electron.*, vol. 7, no. 10, pp. 2647–2659, Oct. 2014.

[46] IEC 61000-4-30, *INTERNATIONAL STANDARD Electromagnetic compatibility (EMC)-Part 4-30: Testing and measurement techniques-Power quality measurement methods INTERNATIONAL ELECTROTECHNICAL COMMISSION*. 2015.

[47] IEC 61000-4-7, *Electromagnetic compatibility (EMC) – Part 4-7: testing and measurement techniques – general guide on harmonics and interharmonics*

measurements and instrumentation, for power supply systems and equipment connected thereto, vol. 2005. 2005.

[48] EN 50160, "Voltage characteristics of electricity supplied by public distribution systems.," *Cenelec*, vol. 3, 2011.

[49] T. D. C. Busarello, J. A. Pomilio, and M. G. Simões, "Passive Filter Aided by Shunt Compensators Based on the Conservative Power Theory," *IEEE Trans. Ind. Appl.*, vol. 52, no. 4, pp. 3340–3347, 2016.

[50] P. C. Sanjeet Kumar Dwivedi, Shailendra Jain, Krishna Kumar Gupta, "Biography," in *Modeling and Control of Power Electronics Converter System for Power Quality Improvements*, vol. 87, no. 1,2, Elsevier, 2018, p. ix.

[51] D. Li, K. Yang, Z. Q. Zhu, and Y. Qin, "A novel series power quality controller with reduced passive power filter," *IEEE Trans. Ind. Electron.*, vol. 64, no. 1, pp. 773–784, 2017.

[52] R. N. Beres, X. Wang, F. Blaabjerg, M. Liserre, and C. L. Bak, "Optimal design of high-order passive-damped filters for grid-connected applications," *IEEE Trans. Power Electron.*, vol. 31, no. 3, pp. 2083–2098, 2016.

[53] T. Toumi, A. Allali, A. Meftouhi, O. Abdelkhalek, A. Benabdelkader, and M. Denai, "Robust control of series active power filters for power quality enhancement in distribution grids: Simulation and experimental validation," *ISA Trans.*, vol. 107, pp. 350–359, 2020.

[54] L. F. J. Meloni, F. L. Tofoli, A. J. J. Rezek, and E. R. Ribeiro, "Modeling and Experimental Validation of a Single-Phase Series Active Power Filter for Harmonic Voltage Reduction," *IEEE Access*, vol. 7, pp. 151971–151984, 2019.

[55] O. S. Senturk and A. M. Hava, "Performance enhancement of the single-phase series active filter by employing the load voltage waveform reconstruction and line current sampling delay reduction methods," *IEEE Trans. Power Electron.*, vol. 26, no. 8, pp. 2210–2220, 2011.

[56] C. Pazhanimuthu, I. Baranilingesan, and A. Karthick, "An improved control algorithm for Series Hybrid Active Power Filter based on SOGI-PLL under dynamic load conditions," *Solid State Commun.*, vol. 333, no. April, p. 114357, 2021.

[57] M. Song, W. Fei, C. Wang, and X. Liu, "Design and Study of a Series Active Filter for the 10MW-Level High Power and High Stability DC Power Supply," *IEEE Trans. Appl. Supercond.*, vol. 32, no. 6, pp. 1–5, 2022.

[58] G. D. S. Fischer, A. Mengatto, L. G. Kremer, and M. Mezaroba, "A Control Strategy for a Series APF with Critical-Load-Bus Voltage Feedback That Avoids Injection Transformer Saturation," *IEEE Trans. Ind. Appl.*, vol. 55, no. 3, pp. 2290–2299, 2019.

[59] S. Hou, J. Fei, C. Chen, and Y. Chu, "Finite-Time Adaptive Fuzzy-Neural-Network Control of Active Power Filter," *IEEE Trans. Power Electron.*, vol. 34, no. 10, pp. 10298–10313, 2019.

[60] Y. P. Obulesu, "Control Strategy for Three Phase Shunt Active Power Filter with Minimum Current Measurements," *Int. J. Electr. Comput. Eng.*, vol. 1, no. 1, pp. 31–42, 2011.

[61] H. L. Jou, K. Der Wu, J. C. Wu, and W. J. Chiang, "A three-phase four-wire power filter comprising a three-phase three-wire active power filter and a zig-zag transformer," *IEEE Trans. Power Electron.*, vol. 23, no. 1, pp. 252–259, 2008.

[62] F. Harirchi and M. G. Simoes, "Enhanced Instantaneous Power Theory Decomposition for Power Quality Smart Converter Applications," *IEEE Trans. Power Electron.*, vol. 33, no. 11, pp. 9344–9359, 2018.

[63] G. S. Chawda *et al.*, "Comprehensive Review on Detection and Classification of Power Quality Disturbances in Utility Grid with Renewable Energy Penetration," *IEEE Access*, vol. 8, pp. 146807–146830, 2020.

[64] R. Puche-Panadero *et al.*, "New Method for Spectral Leakage Reduction in the FFT of Stator Currents: Application to the Diagnosis of Bar Breakages in Cage Motors Working at Very Low Slip," *IEEE Trans. Instrum. Meas.*, vol. 70, 2021.

[65] H. Liu, H. Hu, H. Chen, L. Zhang, and Y. Xing, "Fast and Flexible Selective Harmonic Extraction Methods Based on the Generalized Discrete Fourier Transform," *IEEE Trans. Power Electron.*, vol. 33, no. 4, pp. 3484–3496, 2018.

[66] H. Wen, J. Zhang, W. Yao, and L. Tang, "FFT-Based Amplitude Estimation of Power Distribution Systems Signal Distorted by Harmonics and Noise," *IEEE Trans. Ind. Informatics*, vol. 14, no. 4, pp. 1447–1455, 2018.

[67] T. De Almeida Prado, A. M. A. Barros, and G. A. Guarneri, "An Algorithm Based on Sparse Decomposition for Estimating Harmonic and Interharmonic Components of Stationary Signals in Power Systems," *IEEE Access*, vol. 7, pp. 163958–163968, 2019.

[68] C. Li, J. Zhang, and H. Wen, "Accurate and Fast Amplitude Estimation of Signal Distorted by Noise and Harmonics for Control of VSI," *IEEE Trans. Ind. Electron.*, vol. 68, no. 12, pp. 12584–12594, 2021.

[69] B. Jafarpisheh, S. M. Madani, and S. Jafarpisheh, "Improved DFT-Based phasor estimation algorithm using down-sampling," *IEEE Trans. Power Deliv.*, vol. 33, no. 6, pp. 3242–3245, 2018.

[70] A. Pigazo, M. Liserre, R. A. Mastromauro, V. M. Moreno, and A. Dell'Aquila, "Wavelet-based Islanding detection in grid-connected PV systems," *IEEE Trans. Ind. Electron.*, vol. 56, no. 11, pp. 4445–4455, 2009.

[71] A. Gholami, A. Vosughi, and A. K. Srivastava, “Denoising and Detection of Bad Data in Distribution Phasor Measurements Using Filtering, Clustering, and Koopman Mode Analysis,” *IEEE Trans. Ind. Appl.*, vol. 58, no. 2, pp. 1602–1610, 2022.

[72] X. Pan, L. Zhang, and H. Huang, “Harmonic Cancellation by Adaptive Notch Filter Based on Discrete Wavelet Packet Transform for an MMCC-STATCOM,” *IEEE Trans. Power Deliv.*, vol. 37, no. 3, pp. 1834–1844, 2022.

[73] A. Ferrero, H. V. Jetti, and S. Salicone, “The Possibilistic Kalman Filter: Definition and Comparison with the Available Methods,” *IEEE Trans. Instrum. Meas.*, vol. 70, 2021.

[74] S. Sharifinia *et al.*, “Extended Kalman Filter-Based Approach for Nodal Pricing in Active Distribution Networks,” *IEEE Syst. J.*, vol. 15, no. 1, pp. 487–496, 2021.

[75] Z. Yang, Z. Yan, Y. Lu, W. Wang, L. Yu, and Y. Geng, “Double DOF Strategy for Continuous-Wave Pulse Generator Based on Extended Kalman Filter and Adaptive Linear Active Disturbance Rejection Control,” *IEEE Trans. Power Electron.*, vol. 37, no. 2, pp. 1382–1393, 2022.

[76] V. Moreno, A. Pigazo, and R. I. Diego, “Reference estimation technique for active power filters using a digital Kalman algorithm,” in *10th International Conference on Harmonics and Quality of Power. Proceedings (Cat. No.02EX630)*, 2002, vol. 2, pp. 490–494.

[77] A. Pigazo and R. I. Diego, “Corrections to ‘Reference Current Estimation Under Distorted Line Voltage for Control of Shunt Active Power Filters,’” *IEEE Trans. Power Electron.*, vol. 19, no. 6, pp. 1688–1688, Nov. 2004.

[78] H. Wang and S. Liu, “Adaptive kalman filter for harmonic detection in active power filter application,” *2015 IEEE Electr. Power Energy Conf. Smarter Resilient Power Syst. EPEC 2015*, pp. 227–232, 2016.

[79] S. Golestan, J. M. Guerrero, J. C. Vasquez, A. M. Abusorrah, and Y. Al-Turki, “Single-Phase FLLs Based on Linear Kalman Filter, Limit-Cycle Oscillator, and Complex Bandpass Filter: Analysis and Comparison with a Standard FLL in Grid Applications,” *IEEE Trans. Power Electron.*, vol. 34, no. 12, pp. 11774–11790, 2019.

[80] A. Bagheri, M. Mardaneh, A. Rajaei, and A. Rahideh, “Detection of Grid Voltage Fundamental and Harmonic Components Using Kalman Filter and Generalized Averaging Method,” *IEEE Trans. Power Electron.*, vol. 31, no. 2, pp. 1064–1073, 2016.

[81] S. J. Alam and S. R. Arya, “Control of UPQC based on steady state linear Kalman filter for compensation of power quality problems,” *Chinese J. Electr. Eng.*, vol. 6, no. 2, pp. 52–65, 2020.

[82] R. Cardoso, R. F. De Camargo, H. Pinheiro, and H. A. Gründling, "Kalman filter based synchronisation methods," *IET Gener. Transm. Distrib.*, vol. 2, no. 4, pp. 542–555, 2008.

[83] T. D. Raheni and P. Thirumoorthi, "Intelligent control of shunt active power filter for minimization of current harmonics," in *TENCON 2017 - 2017 IEEE Region 10 Conference*, 2017, no. 1, pp. 2846–2851.

[84] A. A. A. Elgammal and M. F. El-naggar, "MOPSO-based optimal control of shunt active power filter using a variable structure fuzzy logic sliding mode controller for hybrid (FC-PV-Wind-Battery) energy utilisation scheme," *IET Renew. Power Gener.*, vol. 11, no. 8, pp. 1148–1156, Jun. 2017.

[85] Y. Hoon, M. A. M. Radzi, M. K. Hassan, and N. F. Mailah, "Operation of Three-Level Inverter-Based Shunt Active Power Filter under Nonideal Grid Voltage Conditions with Dual Fundamental Component Extraction," *IEEE Trans. Power Electron.*, vol. 33, no. 9, pp. 7558–7570, 2018.

[86] Y. Hoon, M. A. Mohd Radzi, M. K. Hassan, and N. F. Mailah, "Enhanced Instantaneous Power Theory with Average Algorithm for Indirect Current Controlled Three-Level Inverter-Based Shunt Active Power Filter under Dynamic State Conditions," *Math. Probl. Eng.*, vol. 2016, 2016.

[87] L. B. Garcia Campanhol, S. A. Oliveira da Silva, and A. Goedtel, "Application of shunt active power filter for harmonic reduction and reactive power compensation in threephase four-wire systems," *IET Power Electron.*, vol. 7, no. 11, pp. 2825–2836, 2014.

[88] K. Djazia, F. Krim, A. Chaoui, and M. Sarra, "Active power filtering using the ZDPC method under unbalanced and distorted grid voltage conditions," *Energies*, vol. 8, no. 3, pp. 1584–1605, 2015.

[89] S. F. Al-Gahtani, E. Z. M. Salem, S. M. Irshad, and H. Z. Azazi, "Improved Instantaneous Reactive Power (PQ) Theory Based Control of DVR for Compensating Extreme Sag and Swell," *IEEE Access*, vol. 10, no. May, pp. 75186–75204, 2022.

[90] Y. Hoon, M. A. Mohd Radzi, M. K. Hassan, and N. F. Mailah, "A Dual-Function Instantaneous Power Theory for Operation of Three-Level Neutral-Point-Clamped Inverter-Based Shunt Active Power Filter," *Energies*, vol. 11, no. 6, 2018.

[91] S. S. Patnaik and A. K. Panda, "Three-level H-bridge and three H-bridges-based three-phase four-wire shunt active power filter topologies for high voltage applications," *Int. J. Electr. Power Energy Syst.*, vol. 51, pp. 298–306, 2013.

[92] R. Patel and A. K. Panda, "Real time implementation of PI and fuzzy logic controller based 3-phase 4-wire interleaved buck active power filter for mitigation of harmonics with id-iq control strategy," *Int. J. Electr. Power*

Energy Syst., vol. 59, pp. 66–78, 2014.

[93] R. Patel, A. K. Panda, and S. Mikkili, "PI and fuzzy logic controller based 3-phase 4-wire interleaved buck active power filter for mitigation of harmonics with the Id-Iq control strategy," *IECON Proc. (Industrial Electron. Conf.*, vol. 11, no. 6, pp. 2145–2150, 2013.

[94] R. S. Herrera and P. Salmerón, "Instantaneous reactive power theory: A reference in the nonlinear loads compensation," *IEEE Trans. Ind. Electron.*, vol. 56, no. 6, pp. 2015–2022, 2009.

[95] H. Liu, H. Hu, H. Chen, L. Zhang, and Y. Xing, "Fast and Flexible Selective Harmonic Extraction Methods Based on the Generalized Discrete Fourier Transform," *IEEE Trans. Power Electron.*, vol. 33, no. 4, pp. 3484–3496, 2018.

[96] J. F. Petit, G. Robles, and H. Amaris, "Current reference control for shunt active power filters under non-sinusoidal voltage conditions," *IEEE Trans. Power Deliv.*, vol. 22, no. 4, pp. 2254–2261, 2007.

[97] D. TESHOME, T. D. Huang, and K.-L. Lian, "A Distinctive Load Feature Extraction Based on Fryze's Time-domain Power Theory," *IEEE Power Energy Technol. Syst. J.*, vol. 3, no. 2, pp. 1–1, 2016.

[98] V. M. Moreno and A. Pigazo, "Modified FBD method in active power filters to minimize the line current harmonics," *IEEE Trans. Power Deliv.*, vol. 22, no. 1, pp. 735–736, 2007.

[99] X. Nie and J. Liu, "Current Reference Control for Shunt Active Power Filters under Unbalanced and Distorted Supply Voltage Conditions," *IEEE Access*, vol. 7, pp. 177048–177055, 2019.

[100] R. L. De Araujo Ribeiro, C. C. De Azevedo, and R. M. I. De Sousa, "A robust adaptive control strategy of active power filters for power-factor correction, harmonic compensation, and balancing of nonlinear loads," *IEEE Trans. Power Electron.*, vol. 27, no. 2, pp. 718–730, 2012.

[101] R. L. de A. Ribeiro, T. de O. A. Rocha, R. M. de Sousa, E. C. dos Santos, and A. M. N. Lima, "A Robust DC-Link Voltage Control Strategy to Enhance the Performance of Shunt Active Power Filters Without Harmonic Detection Schemes," *IEEE Trans. Ind. Electron.*, vol. 62, no. 2, pp. 803–813, Feb. 2015.

[102] H. Komurcugil, S. Bayhan, N. Guler, and F. Blaabjerg, "An Effective Model Predictive Control Method with Self-Balanced Capacitor Voltages for Single-Phase Three-Level Shunt Active Filters," *IEEE Access*, vol. 9, pp. 103811–103821, 2021.

[103] T. Gao, Y. Lin, D. Chen, and Z. Xu, "A DC-link Balancing Control Strategy for NPC Three-level Shunt Active Power Filter," *2020 4th Int. Conf. Power Energy Eng. ICPEE 2020*, pp. 163–167, 2020.

[104] H. H. Huang, E. Li, and H. Wang, “Three-level equilibrium strategy of DC voltage balance control for H-bridge cascaded active power filter,” *IEEE Access*, vol. 7, pp. 28847–28854, 2019.

[105] S. Hou, Y. Chu, and J. Fei, “Intelligent Global Sliding Mode Control Using Recurrent Feature Selection Neural Network for Active Power Filter,” *IEEE Trans. Ind. Electron.*, vol. 68, no. 8, pp. 7320–7329, Aug. 2021.

[106] M. Iqbal *et al.*, “Neural Networks Based Shunt Hybrid Active Power Filter for Harmonic Elimination,” *IEEE Access*, vol. 9, pp. 69913–69925, 2021.

[107] S. Agrawal, P. Kumar, and D. K. Palwalia, “Artificial neural network based three phase shunt active power filter,” in *2016 IEEE 7th Power India International Conference (PIICON)*, 2016, pp. 1–6.

[108] J. Jayachandran and R. Murali Sachithanandam, “ANN based controller for three phase four leg shunt active filter for power quality improvement,” *Ain Shams Eng. J.*, vol. 7, no. 1, pp. 275–292, 2016.

[109] D. T. Vu, N. K. Nguyen, E. Semail, and H. Wu, “Adaline-Based Control Schemes for Non-Sinusoidal Multiphase Drives—Part II: Torque Optimization for Faulty Mode,” *Energies*, vol. 15, no. 1, 2022.

[110] A. Bhattacharya and C. Chakraborty, “A shunt active power filter with enhanced performance using ANN-based predictive and adaptive controllers,” *IEEE Trans. Ind. Electron.*, vol. 58, no. 2, pp. 421–428, 2011.

[111] P. Garanayak, R. T. Naayagi, and G. Panda, “A High-Speed Master-Slave ADALINE for Accurate Power System Harmonic and Inter-Harmonic Estimation,” *IEEE Access*, vol. 8, pp. 51918–51932, 2020.

[112] Y. Hoon, M. Amran, M. Radzi, M. K. Hassan, and N. F. Mailah, “A Self-Tuning Filter-Based Adaptive Linear Neuron Approach for Operation of Three-Level Inverter-Based Shunt Active Power Filters under Non-Ideal Source Voltage Conditions,” *Energies*, vol. 10, no. 5, p. 667, 2017.

[113] M. Ammirrul *et al.*, “Fundamental Active Current Adaptive Linear Neural Networks for Photovoltaic Shunt Active Power Filters,” *Energies*, vol. 9, pp. 1–21, 2016.

[114] M. A. A. M. Zainuri, M. A. M. Radzi, A. C. Soh, N. Mariun, N. A. Rahim, and S. Hajighorbani, “Fundamental active current adaptive linear neural networks for photovoltaic shunt active power filters,” *Energies*, vol. 9, no. 6, pp. 1–20, 2016.

[115] Y. Hoon, M. A. M. Radzi, M. K. Hassan, and N. F. Mailah, “A refined self-tuning filter-based instantaneous power theory algorithm for indirect current controlled three-level inverter-based shunt active power filters under non-sinusoidal source voltage conditions,” *Energies*, vol. 10, no. 3, pp. 1–20, 2017.

[116] R. El Shatshat, M. Kazerani, and M. M. A. Salama, "On-line tracking and mitigation of power system harmonics using ADALINE-based active power filter system," *Can. Conf. Electr. Comput. Eng.*, vol. 4, pp. 2119–2124, 2004.

[117] F. L. Yousfi, D. Ould Abdeslam, T. Bouthiba, N. K. Nguyen, and J. Mercklé, "Adaline for online symmetrical components and phase-angles identification in transmission lines," *IEEE Trans. Power Deliv.*, vol. 27, no. 3, pp. 1134–1143, 2012.

[118] V. Mane and A. Agashe, "An Adaptive Notch Filter For Noise Reduction and Signal Decomposition," in *International Journal of Computer Science Issues*, 2011, vol. 8, no. 5, pp. 360–365.

[119] M. Mojiri, M. Karimi-ghartemani, and A. Bakhshai, "Time-Domain Signal Analysis Using Adaptive Notch Filter," *IEEE Trans. SIGNAL Process.*, vol. 55, no. 1, pp. 85–93, 2007.

[120] D. Yazdani, A. Bakhshai, G. Joos, and M. Mojiri, "An adaptive notch filtering approach for harmonic and reactive current extraction in active power filters," *IECON Proc. (Industrial Electron. Conf.*, pp. 535–538, 2008.

[121] R. S. R. Chilipi, N. Al Sayari, K. H. Al Hosani, and A. R. Beig, "Adaptive Notch Filter-Based Multipurpose Control Scheme for Grid-Interfaced Three-Phase Four-Wire DG Inverter," *IEEE Trans. Ind. Appl.*, vol. 53, no. 4, pp. 4015–4027, Jul. 2017.

[122] K. H. Tan, F. J. Lin, and J. H. Chen, "DC-Link voltage regulation using RPFNN-AMF for Three-Phase active power filter," *IEEE Access*, vol. 6, pp. 37454–37463, 2018.

[123] N. F. ABDUL RAHMAN, M. A. MOHD RADZI, A. CHE SOH, N. MARIUN, and N. ABD RAHIM, "Significant insights into the operation of DC-link voltage control of a shunt active power filter using different control algorithms: a comparative study," *Turkish J. Electr. Eng. Comput. Sci.*, vol. 25, pp. 2033–2043, 2017.

[124] Y. Huang, Z. Zhang, W. Huang, and S. Chen, "DC-Link Voltage Regulation for Wind Power System by Complementary Sliding Mode Control," *IEEE Access*, vol. 7, pp. 22773–22780, 2019.

[125] T. Demirdelen *et al.*, "A sliding mode control method of dc-link capacitor voltage used in active power filter," *7th Power Electron. Drive Syst. Technol. Conf. PEDSTC 2016*, vol. 1, no. 2, pp. 23–25, 2016.

[126] M. S. Mousavi, A. Jalilian, and M. Asadi, "A sliding mode control method of dc-link capacitor voltage used in active power filter," *30th Power Syst. Conf. PSC 2015*, no. November 2015, pp. 123–128, 2017.

[127] J. Fei, N. Liu, S. Hou, and Y. Fang, "Neural network complementary sliding

mode current control of active power filter,” *IEEE Access*, vol. 9, pp. 25681–25690, 2021.

[128] Y. Chen, R. Tan, Y. Zheng, and Z. Zhou, “Sliding-mode control with multipower approaching law for dc-link voltage of z-source photovoltaic inverters,” *IEEE Access*, vol. 7, pp. 133812–133821, 2019.

[129] J. Fei and Y. Chen, “Dynamic Terminal Sliding-Mode Control for Single-Phase Active Power Filter Using New Feedback Recurrent Neural Network,” *IEEE Trans. Power Electron.*, vol. 35, no. 9, pp. 9906–9924, 2020.

[130] V. Rajakumar, K. Anbukumar, and A. Immanuel Selwynraj, “Sliding mode controller-based voltage source inverter for power quality improvement in microgrid,” *IET Renew. Power Gener.*, vol. 14, no. 11, pp. 1860–1872, 2020.

[131] Y. Chen and J. Fei, “Dynamic Sliding Mode Control of Active Power Filter with Integral Switching Gain,” *IEEE Access*, vol. 7, pp. 21635–21644, 2019.

[132] N. F. Mailah, Y. Hoon, and M. A. M. Radzi, “DC-link capacitor voltage regulation with effort-reduction fuzzy logic control for three-level inverter-based shunt active power filter,” *Pertanika J. Sci. Technol.*, vol. 25, no. S, pp. 11–20, 2017.

[133] M. A. A. M. Zainuri, M. A. M. Radzi, A. C. Soh, N. Mariun, and N. A. Rahim, “DC-link capacitor voltage control for single-phase shunt active power filter with step size error cancellation in self-charging algorithm,” *IET Power Electron.*, vol. 9, no. 2, pp. 323–335, 2016.

[134] J. Choudhary, D. K. Singh, S. N. Verma, and K. Ahmad, “Artificial Intelligence Based Control of a Shunt Active Power Filter,” *Procedia Comput. Sci.*, vol. 92, pp. 273–281, 2016.

[135] P. U. Panati, S. Ramasamy, M. Ahsan, J. Haider, and E. M. G. Rodrigues, “Indirect effective controlled split source inverter-based parallel active power filter for enhancing power quality,” *Electron.*, vol. 10, no. 8, 2021.

[136] P. K. Barik, G. Shankar, and P. K. Sahoo, “Power quality assessment of microgrid using fuzzy controller aided modified SRF based designed SAPF,” *Int. Trans. Electr. Energy Syst.*, vol. 30, no. 4, pp. 1–24, 2020.

[137] P. Mishra, A. K. Pradhan, and P. Bajpai, “Voltage control of PV inverter connected to unbalanced distribution system,” *IET Renew. Power Gener.*, vol. 13, no. 9, pp. 1587–1594, 2019.

[138] Y. Hoon, M. A. M. Radzi, M. K. Hassan, and N. F. Mailah, “DC-link capacitor voltage regulation for three-phase three-level inverter-based shunt active power filter with inverted error deviation control,” *Energies*, vol. 9, no. 7, 2016.

[139] H. Lin *et al.*, “Integral sliding-mode control-based direct power control for

three-level NPC converters," *Energies*, vol. 13, no. 1, pp. 1–20, 2020.

[140] B. Rahima, G. Amar, B. Mohamed Toufik, and C. Mohamed, "High-performance active power filter implementation based on predictive current control," *Int. J. Power Electron. Drive Syst.*, vol. 10, no. 1, p. 277, 2019.

[141] N. Abdul Rahman, M. Mohd Radzi, A. Che Soh, N. Mariun, and N. Abd Rahim, "Adaptive Hybrid Fuzzy-Proportional Plus Crisp-Integral Current Control Algorithm for Shunt Active Power Filter Operation," *Energies*, vol. 9, no. 9, p. 737, 2016.

[142] M. Parvez, M. F. M. Elias, N. A. Rahim, F. Blaabjerg, D. Abbott, and S. F. Al-Sarawi, "Comparative study of discrete PI and PR controls for single-phase UPS inverter," *IEEE Access*, vol. 8, pp. 45584–45595, 2020.

[143] W. Qiao and R. G. Harley, "Power quality and dynamic performance improvement of wind farms using a STATCOM," *PESC Rec. - IEEE Annu. Power Electron. Spec. Conf.*, pp. 1832–1838, 2007.

[144] H. Shutari, N. Saad, N. B. M. Nor, M. F. N. Tajuddin, A. Alqushaibi, and M. A. Magzoub, "Towards Enhancing the Performance of Grid-Tied VSWT via Adopting Sine Cosine Algorithm-Based Optimal Control Scheme," *IEEE Access*, vol. 9, pp. 139074–139088, 2021.

[145] B. Liu, W. Song, J. Chen, and X. Feng, "Model predictive power control for grid-connected ac–dc converters with trajectory optimisation of the modulated voltage vector," *IET Power Electron.*, vol. 13, no. 10, pp. 2060–2068, 2020.

[146] S. Choudhury, P. Bhowmik, and P. K. Rout, "Economic load sharing in a D-STATCOM Integrated Islanded Microgrid based on Fuzzy Logic and Seeker Optimization Approach," *Sustain. Cities Soc.*, vol. 37, no. September 2017, pp. 57–69, 2018.

[147] W. Dai, C. Li, Z. Cui, Y. Wu, L. Zhang, and J. Huang, "An Improved Dragonfly Algorithm with Higher Exploitation Capability to Optimize the Design of Hybrid Power Active Filter," *IEEE Access*, vol. 8, pp. 155020–155038, 2020.

[148] S. H. E. A. Aleem, A. F. Zobaa, M. E. Balci, and S. M. Ismael, "Harmonic overloading minimization of frequency-dependent components in harmonics polluted distribution systems using harris hawks optimization algorithm," *IEEE Access*, vol. 9, pp. 100824–100837, 2019.

[149] F. G. Montoya, A. Alcayde, F. M. Arrabal-Campos, and R. Baños, "Quadrature current compensation in non-sinusoidal circuits using geometric algebra and evolutionary algorithms," *Energies*, vol. 12, no. 4, pp. 14–16, 2019.

[150] V. Verma and B. Singh, "Genetic-algorithm-based design of passive filters for offshore applications," *IEEE Trans. Ind. Appl.*, vol. 46, no. 4, pp. 1295–1303, 2010.

[151] W. Lenwari, M. Sumner, and P. Zanchetta, “The use of genetic algorithms for the design of resonant compensators for active filters,” *IEEE Trans. Ind. Electron.*, vol. 56, no. 8, pp. 2852–2861, 2009.

[152] S. Zhang, X. Zhu, J. Geng, and R. Zhang, “Evaluation of enterprise performance based on FLI-GA model,” *J. Ind. Eng. Manag.*, vol. 7, no. 2 SPEC. ISSUE, pp. 373–389, 2014.

[153] H. Y. Fan, J. W. Z. Lu, and Z. Ben Xu, “An empirical comparison of three novel genetic algorithms,” *Eng. Comput. (Swansea, Wales)*, vol. 17, no. 8, pp. 981–1001, 2000.

[154] D. B. Fogel, “Asymptotic convergence properties of genetic algorithms and evolutionary programming: analysis and experiments,” *Cybern. Syst.*, vol. 25, no. 3, pp. 389–407, 1994.

[155] N. He, D. Xu, and L. Huang, “The application of particle swarm optimization to passive and hybrid active power filter design,” *IEEE Trans. Ind. Electron.*, vol. 56, no. 8, pp. 2841–2851, 2009.

[156] W. Cao, K. Liu, M. Wu, S. Xu, and J. Zhao, “An Improved Current Control Strategy Based on Particle Swarm Optimization and Steady-State Error Correction for SAPF,” *IEEE Trans. Ind. Appl.*, vol. 55, no. 4, pp. 4268–4274, 2019.

[157] R. S. R. Chilipi, N. Al Sayari, K. H. Al Hosani, and A. R. Beig, “Adaptive Notch Filter-Based Multipurpose Control Scheme for Grid-Interfaced Three-Phase Four-Wire DG Inverter,” *IEEE Trans. Ind. Appl.*, vol. 53, no. 4, pp. 4015–4027, 2017.

[158] W. U. K. Tareen *et al.*, “Mitigation of power quality issues due to high penetration of renewable energy sources in electric grid systems using three-phase APF/STATCOM technologies: A review,” *Energies*, vol. 11, no. 6, 2018.

[159] A. El-Nady and A. Noureldin, “Mitigation of Arc furnace voltage flicker using an innovative scheme of adaptive notch filters,” *IEEE Trans. Power Deliv.*, vol. 26, no. 3, pp. 1326–1336, 2011.

[160] B. Mariappan, B. G. Fernandes, and M. Ramamoorty, “A novel single-stage solar inverter using hybrid active filter with power quality improvement,” *Proceedings, IECON 2014 - 40th Annu. Conf. IEEE Ind. Electron. Soc.*, pp. 5443–5449, 2014.

[161] V. N. Jayasankar and U. Vinatha, “Backstepping Controller with Dual Self-Tuning Filter for Single-Phase Shunt Active Power Filters under Distorted Grid Voltage Condition,” *IEEE Trans. Ind. Appl.*, vol. 56, no. 6, pp. 7176–7184, 2020.

[162] R. Kumar, H. O. Bansal, A. R. Gautam, O. P. Mahela, and B. Khan,

"Experimental Investigations on Particle Swarm Optimization Based Control Algorithm for Shunt Active Power Filter to Enhance Electric Power Quality," *IEEE Access*, vol. 10, pp. 54878–54890, 2022.

[163] Y. F. Wang and Y. W. Li, "A grid fundamental and harmonic component detection method for single-phase systems," *IEEE Trans. Power Electron.*, vol. 28, no. 5, pp. 2204–2213, 2013.

[164] H. W. Salih, S. Wang, and J. A. Dora, "Adaptive Notch Filter based Fuzzy controller for synchronization of grid with renewable energy sources," *2015 Conf. Power, Control. Commun. Comput. Technol. Sustain. Growth, PCCCTSG 2015*, pp. 122–127, 2016.

[165] H. Khas and H. Khas, "Discrete Adaptive Notch Filter based Single Phase Solar PV Integrated UPQC," in *International Conference on Power Electronics, Intelligent Control and Energy Systems*, 2016, pp. 1–5.

[166] A. R. B. Raja Sekhara Reddy Chilipi, Naji Al Sayari, Khalifa Al Hosani, A. Notch, F. Based, and M. Control, "Adaptive Notch Filter Based Multipurpose Control Scheme for Grid-Interfaced Three-Phase Four-Wire DG Inverter," *IEEE Ind. Appl. Soc. Annu. Meet.*, pp. 1–8, 2016.

[167] S. H. Tabatabaei, M. Moslehi Bajestan, and A. Jalilian, "Shunt active power filter control for compensating current power quality problems in three-phase three-wire systems based on an adaptive notch filter," *Turkish J. Electr. Eng. Comput. Sci.*, vol. 24, no. 4, pp. 2539–2555, 2016.

[168] H. W. Salih, Shaorong Wang, and J. A. Dora, "Adaptive Notch Filter based Fuzzy controller for synchronization of grid with renewable energy sources," in *2015 Conference on Power, Control, Communication and Computational Technologies for Sustainable Growth (PCCCTSG)*, 2015, pp. 122–127.

[169] G. Fujita, N. D. Dinh, T. Funabashi, and N. D. Tuyen, "Adaptive notch filter solution under unbalanced and/or distorted point of common coupling voltage for three-phase four-wire shunt active power filter with sinusoidal utility current strategy," *IET Gener. Transm. Distrib.*, vol. 9, no. 13, pp. 1580–1596, 2015.

[170] N. D. Tuyen, G. Fujita, T. Funabashi, and M. Nomura, "Adaptive notch filter for synchronization and islanding detection using negative-sequence impedance measurement," *IEEJ Trans. Electr. Electron. Eng.*, vol. 7, no. 3, pp. 240–250, May 2012.

[171] A. Ketabi, M. Farshadnia, M. Malekpour, and R. Feuillet, "A new control strategy for active power line conditioner (APLC) using adaptive notch filter," *Int. J. Electr. Power Energy Syst.*, vol. 47, no. 1, pp. 31–40, 2013.

[172] S. Rafiei, A. Moallem, A. Bakhshai, and D. Yazdani, "Application of a digital ANF-based power processor for micro-grids power quality enhancement," in *Conference Proceedings - IEEE Applied Power Electronics Conference and*

Exposition - APEC, 2014, pp. 3055–3059.

[173] J. C. Alfonso-Gil, E. Pérez, C. Ariño, and H. Beltran, “Optimization algorithm for selective compensation in a shunt active power filter,” *IEEE Trans. Ind. Electron.*, vol. 62, no. 6, pp. 3351–3361, 2015.

[174] B. Singh, S. R. Arya, and K. Kant, “Notch filter-based fundamental frequency component extraction to control distribution static compensator for mitigating current-related power quality problems,” *IET Power Electron.*, vol. 8, no. 9, pp. 1758–1766, Sep. 2015.

[175] S. K. Kesharvani, A. Singh, and M. Badoni, “Conductance based fryze algorithm for improving power quality for non-linear loads,” *2014 Int. Conf. Signal Propag. Comput. Technol. ICSPCT 2014*, pp. 703–708, 2014.

[176] Z. Zeng, R. Zhao, and H. Yang, “Coordinated control of multi-functional grid-tied inverters using conductance and susceptance limitation,” *IET Power Electron.*, vol. 7, no. 7, pp. 1821–1831, 2014.

[177] A. Sunbul, A. Alduraibi, and F. Zare, “Harmonics Mitigation Filter for High-Power Applications,” *IEEE Access*, vol. 10, no. September, pp. 111406–111418, 2022.

[178] G. S. Kumar, B. K. Kumar, and M. K. Mishra, “Mitigation of voltage sags with phase jumps by UPQC with PSO-Based ANFIS,” *IEEE Trans. Power Deliv.*, vol. 26, no. 4, pp. 2761–2773, 2011.

[179] S. S. Patnaik and A. K. Panda, “Real-time performance analysis and comparison of various control schemes for particle swarm optimization-based shunt active power filters,” *Int. J. Electr. Power Energy Syst.*, vol. 52, no. 1, pp. 185–197, 2013.

APPENDICES

Appendix A

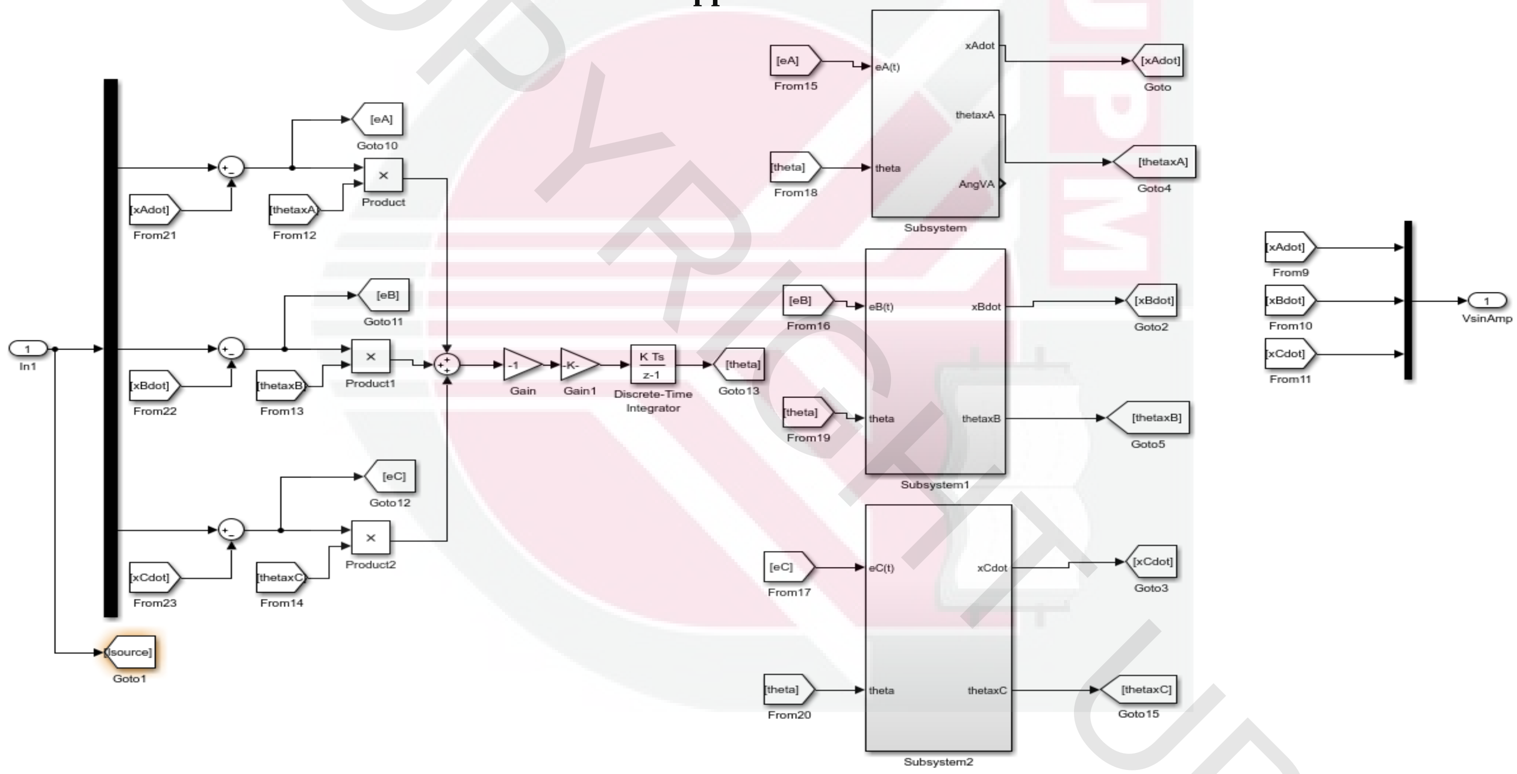

Figure A.1 : Simulation model for three phase ANF

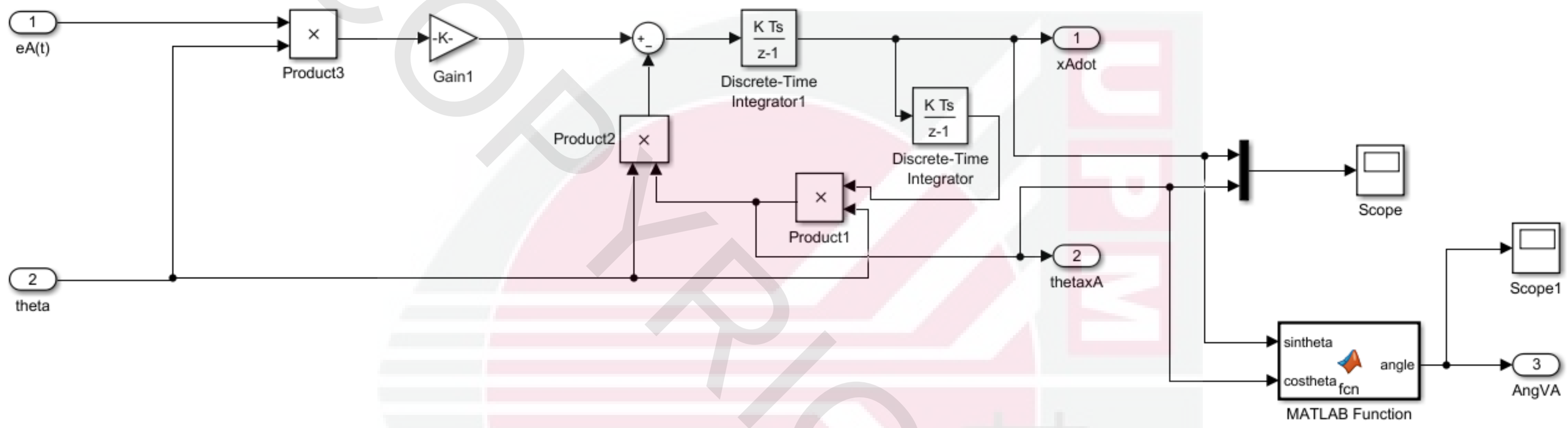

Figure A.2: Simulation block of ANF tracking

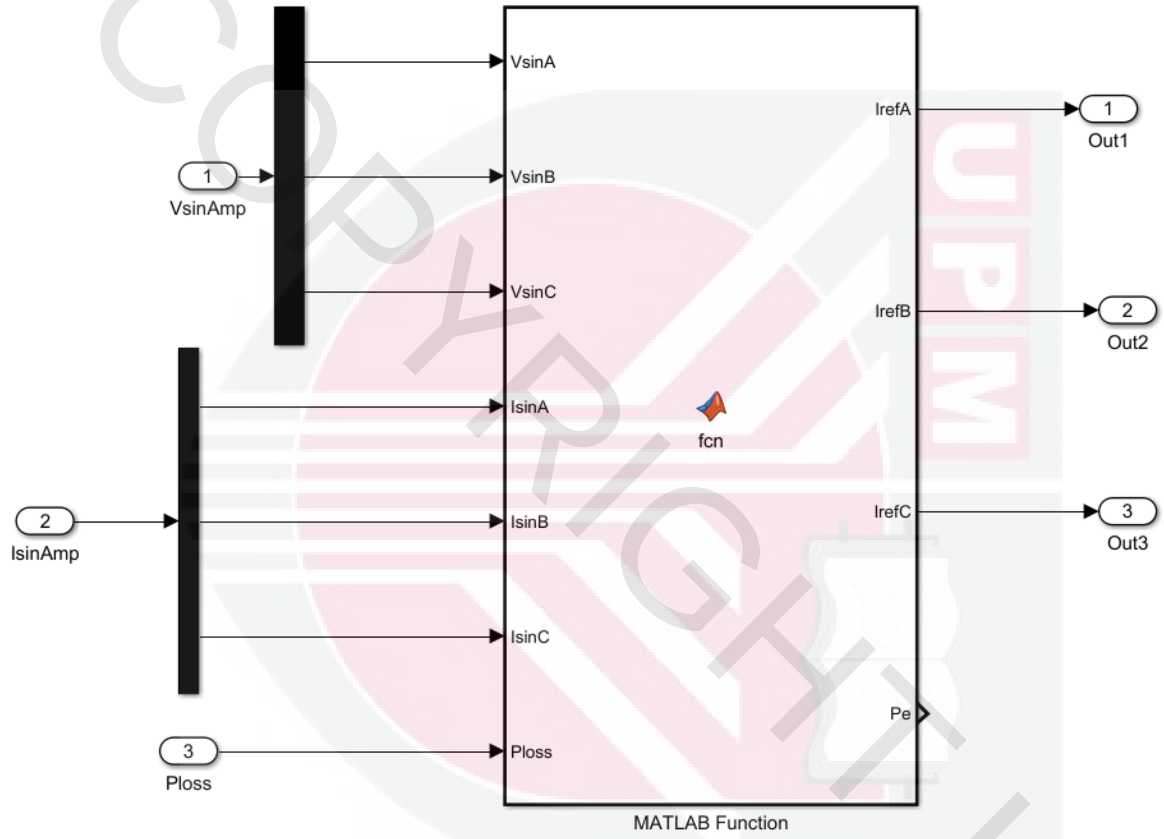

Figure A.3: Simulation block of reference generation algorithm

Appendix B

WBSO ALGORITHM

Table 5-1: PSO Algorithm

Algorithm 1: PSO Algorithm

```
Initialize all particles with a random position and velocity in the search space
while stopping condition not met
  for each particle do
    Calculate the fitness of the particles
    if particle fitness is better than the previous pbest then
      Set particle fitness value as new pbest
    end if
    if the particle fitness value is better than the current gbest then
      Set fitness value as the new gbest
    end if
  end for
  for each particle do
    Update particle velocity according to (2)
    Update the particle position according to (1)
  end for
end while
Present gbest solution
```

```
% Symbols directory
% A/G/Pe - Agent (or Particle in PSO)/Global Best/Personal Best
% F/P/V  - Fitness/Position/Velocity
% s/c    - Social Coefficient/Congnitive Coefficient
% iw     - Inertia Weight
% i      - Iteration
% p      - Particle @ agent
% d      - Dimension
% N      - Number of
%SAE - Sum Absolute Error
%SSE - Sum Square Error

% Clear previous data
clc;
clear;
count=;
hari=datetime('now','Format','yyyy_MM_dd');
tStart=tic;

% Particle Swarm Optimization (PSO) Parameters
Ts = 0.000005; %sampling time
TS = 2; %end time

%a=2;
%A=20;
%b=5;
```

```
s = 2; %social coof
c = 2; %personal / cognitive coof
iw = 0.9; %inertia weight
Np = 6;
Nd = 2;
Ni = 18;
NF = 5; %berapa byk fitness function nak guna.. kalau byk kena ada
prority

AP = zeros(Np,Nd); %agent position
AV = zeros(Np,Nd); %agent velocity
GP = zeros(Ni,Nd); %global best position
PeP = zeros(Np,Nd);%personal best position



% Initialize PSO Algorithm
GF(1,1:5) = inf;

lb=[0.000001, 0.000001];
ub=[1000, 1000];

for p = 1:Np
    for d = 1:Nd
        AP(p,d) = lb(d) + (ub(d)-lb(d))*rand();
        % AP(p,d) = 200 * rand(); %200 sb boundry smpi 200
        AV(p,d) = rand(); %atau 0 pun ok starting velocity
    end

    PeF(p,1:5) = inf;
end

% Start Iteartion of PSO Algorithm
for i=1:Ni

    iw = 0.4 + 0.5 * (Ni - i)/Ni; % linear decreasing inertia weight
from 0.9 to 0.4

    for p = 1:Np

        Kp = AP(p,1)
        Ki = AP(p,2)

        sim('ANFFryzePIDPSO');

        % Priority-based Fitness
        % AF(p,2) = e0;
        % AF(p,1) = THD

        % Weightage-based Fitness
        w1 = 0.5;
        w2 = 1 - w1;

        disp('| w | THD | e0 | Kp | Ki |');
        AF(p,1) =  w1 * e0 + w2 * THD
        AF(p,2)   = THD
        AF(p,3)   = e0
```

```
     AF(p,4)   = Kp
     AF(p,5)   = Ki

    data(count,1)=THD(size(THD,1));
    data(count,2)=Kp(size(Kp,1));
    data(count,3)=Ki(size(Ki,1));
    data(count,4)=VS(size(VS,1));
    data(count,5)=IS(size(IS,1));
    data(count,6)=IL(size(IL,1));
    data(count,7)=e0(size(e0,1));
    data(count,:)
    count=count+1;
    save('databaru2.mat');

     % Update Personal Best Record
     if (AF(p,1) <= PeF(p,1))
         if (AF(p,1) == PeF(p,1))
             if (AF(p,2) <=  PeF(p,2))
                 if (AF(p,2) == PeF(p,2))
                     if (AF(p,3) <  PeF(p,3))
                         PeF(p,:) = AF(p,:);
                         PeP(p,:) = AP(p,:);
                     end
                 else
                     PeF(p,:) = AF(p,:);
                     PeP(p,:) = AP(p,:);
                 end
             end
         else
             PeF(p,:) = AF(p,:);
             PeP(p,:) = AP(p,:);
         end
     end
end

for p = 1:Np
    % Update Global Best Record
    if (AF(p,1) <= GF(i,1))
        if (AF(p,1) == GF(i,1))
            if (AF(p,2) <= GF(i,2))
                if (AF(p,2) == GF(i,2))
                    if (AF(p,3) < GF(i,3))
                        GF(i,:) = AF(p,:);
                        GP(i,:) = AP(p,:);
                    end
                else
                    GF(i,:) = AF(p,:);
                    GP(i,:) = AP(p,:);
                end
            end
        else
            GF(i,:) = AF(p,:);
            GP(i,:) = AP(p,:);
        end
    end
end

for p = 1:Np
    for d = 1:Nd
```

```
            % Update Particle Velocity
            AV(p,d) = iw * AV(p,d) + c * rand() * (PeP(p,d) -
AP(p,d)) + s * rand() * (GP(i,d) - AP(p,d));

            % Update Particle Position
            AP(p,d) = AP(p,d) + AV(p,d);

            %check for upper boundry limit
            if AP(p,d) > ub(d)
                AP(p,d)= abs(ub(d) - AP(p,d));
            end

            %check for lower boundry limit
            if AP(p,d) < lb(d)
                AP(p,d)= abs(lb(d) + AP(p,d));
            end

        end
    end


    % Display Global Best Fitness For Iteration i
    i
    disp('| w | THD | e0 | Kp | Ki |');
    GF(i,:)

    % Update Information Of Global Best
    GF(i+1,:) = GF(i,:);
    GP(i+1,:) = GP(i,:);

end
% Display Best Found Result
e = GP(i,1);
delta = GP(i,2);

disp('| w | THD | e0 | Kp | Ki |');
GF(i,:)

sim('ANFFryzePID');

plot(1:Ni,GF(1:Ni,1));
title('SSE');

tEnd=toc(tStart);
fprintf('%d hours %d minutes and %f
seconds\n',floor(floor(tEnd/60)/60), rem(floor(tEnd/60),60),
rem(tEnd,60));

file_att_alt=sprintf('data_%s_%d.mat',hari,count);
save(file_att_alt, '-v7.3');

load handel.mat;
sound(y, 2*Fs);
```

LIST OF PUBLICATIONS

S. H. Mohamad, M. A. M. Radzi, N. F. Mailah, N. I. A. Wahab, A. Jidin, and M. Y. Lada, “Adaptive notch filter under indirect and direct current controls for active power filter,” Bull. Electr. Eng. Informatics, vol. 9, no. 5, pp. 1794–1802, 2020.

S. H. Mohamad, M. A. M. Radzi, N. F. Mailah, N. I. A. Wahab, and A. Jidin, “Mitigation of Harmonic Current for Balanced Three-Phase Power System Based on Extended Fryze Adaptive Notch Filter,” J. Eng. Sci. Technol., vol. 18, no. 2, pp. 1339–1362, 2023.